A SOFTWARE FOR ANALYSIS AND DESIGN OPTIMIZATION OF SWITCHED RELUCTANCE MOTOR

A THESIS SUBMITTED TO
THE GRADUATE SCHOOL OF NATURAL AND APPLIED SCIENCES
OF
MIDDLE EAST TECHNICAL UNIVERSITY

BY

LEVENT BURAK YALÇINER

IN PARTIAL FULFILLMENT OF THE REQUIREMENTS FOR THE DEGREE
OF
MASTER OF SCIENCE

IN

ELECTRICAL AND ELECTRONICS ENGINEERING

APRIL 2004

Approval of the Graduate School of Natural and Applied Sciences

Prof. Dr. Canan ÖZGEN
Director

I certify that this thesis satisfies all the requirements as a thesis for the degree of Master of Science.

Prof. Dr. Mübeccel DEMİREKLER
Head of the Department

This is to certify that we have read this thesis and that in our opinion it is fully adequate, in scope and quality, as a thesis for the degree of Master of Science.

Prof. Dr. H. Bülent ERTAN
Supervisor

Examining Committee Members

Prof.Dr.Muammer ERMİŞ (M.E.T.U. EE)

Prof. Dr. H. Bülent ERTAN (M.E.T.U. EE)

Prof. Dr. Kemal LEBLEBİCİOĞLU (M.E.T.U. EE)

Prof.Dr. Yildirim ÜÇTUĞ (M.E.T.U. EE)

Erdal BİZKEVELCİ(M.Sc.) (TÜBİTAK – BİLTEN)

I hereby declare that all information in this document has been obtained and presented in accordance with academic rules and ethical conduct. I also declare that, as required by these rules and conduct, I have fully cited and referenced all material and results that are not original to this work.

Levent Burak YALÇINER

ABSTRACT

A SOFTWARE FOR ANALYSIS AND DESIGN OPTIMIZATION OF SWITCHED RELUCTANCE MOTOR

YALÇINER, Levent Burak
M.Sc., Department of Electrical and Electronics Engineering
Supervisor: Prof. Dr. H. Bülent ERTAN

April 2004, 130 pages

In this study, development of software, which can analyze and optimize an SRM by accurately calculating its performance, is aimed. Existing methods in the literature are investigated. Some studies for the calculation of performance use 2D field solutions and are known to be accurate; however, using field solutions is not feasible for the optimization purpose. So, a method based on a set of normalized permeance and force data are chosen for prediction of magnetizing characteristics. Selected methods are programmed into the software with a user friendly interface.

The results from the software are compared with test results from an existing motor. It is found that the accuracy of the predictions is not acceptable if the effect of end winding leakage flux is not accounted for. An approach is proposed for accounting the end winding leakage. The software is modified accordingly. In this case, the results obtained are found to have good accuracy, compared with measurements.

The SR motor design optimization problem is treated as a constrained wieght optimization problem. This problem is converted to an unconstrained optimization problem, by using the Augmented Lagrangian method. To decrease the computation time of some of the performance calculation algorithms, some modifications are made. These are described in the related sections. The derivatives for the optimization process are numerically calculated. The accuracy of the performance calculation is once again verified against test results at this stage. The optimization software is then used to optimize the design of an SR motor for a washing machine application. The results obtained are discussed.

Keywords: switched reluctance motor, analysis, design optimization.

ÖZ

ANAHTARLAMALI RELÜKTANS MOTORUN ANALİZİ VE DİZAYN OPTİMİZASYONU İÇİN BİR BİLGİSAYAR PROGRAMI

YALÇINER, Levent Burak
Yüksek Lisans, Elektrik Elektronik Mühendisliği Bölümü
Tez Danışmanı: Prof. Dr. H. Bülent ERTAN

Nisan 2004, 130 sayfa

Bu çalışmada, anahtarlamalı relüktans motorunun(ARM) analizini ve optimizasyonunu hassas olarak gerçekleştiren bir yazılımın geliştirilmesi amaçlanmıştır. Literatürde geçen metodlar araştırılmıştır. Bazı çalışmalar, performans hesaplamaları için, hassas sonuçlar verdikleri bilinen 2 boyutlu alan çözümlerini kullanmışlardır. Ancak, bir optimizasyon süreci için, alan çözümleri yeterince hızlı değildir. Bu yüzden, mıknatıslanma karakteristiklerinin hesaplanmasında, normalize edilmiş permeans ve kuvvet verilerine dayalı bir metod seçilmiştir. Seçilen metodlar, kullanıcı dostu bir arabirimle yazılım haline getirilmiştir.

Yazılımdan alınan sonuçlar, varolan bir motorun test sonuçlarıyla karşılaştırılmıştır. Sonuçlardan, sarım sonu kaçak akı etkisi hesaba katılmazsa, hesaplamaların hassasiyetinin kabul edilemez seviyede olduğu tespit edilmiştir. Bu etkiyi hesaba katan bir yaklaşım öne sürülmüştür. Yazılım bu doğrultuda değiştirilmiştir. Bu durumda, elde edilen sonuçların, ölçümlerle karşılaştırıldığında, çok daha hassas değerlere sahip olduğu görülmüştür.

ARM tasarım optimizasyonu problemi, kısıtlara sahip bir ağırlık optimizasyon problemi olarak değerlendirilmiştir. Problem, Augmented Lagrangian metodu kullanılarak kısıtsız optimizasyon formuna çevrilmiştir. Performans hesaplamalarının aldığı zamanı azaltmak için bazı değişiklikler yapılmıştır. Bunlar ilgili bölümlerde anlatılmıştır. Optimizasyon sürecinde, türevler nümerik olarak hesaplanmıştır. Performans hesaplamalarının hassasiyeti, bu aşamada test sonuçları kullanılarak bir daha doğrulanmıştır. Bundan sonra, bir çamaşır makinası uygulaması için optimizasyon yazılımı çalıştırılmıştır. Elde edilen sonuçlar ilgili bölümlerde tartışılmıştır.

Anahtar Kelimeler: anahtarlamalı relüktans motoru, analiz, tasarım optimizasyonu.

ACKNOWLEDGEMENTS

I express sincere appreciation to my thesis supervisor Prof. Dr. H. Bülent Ertan for his valuable advice and guidance throughout all stages of this study.

I offer sincere thanks to Erdal BİZKEVELCİ, who encouraged me during M.Sc. study.

I wish to thank Cüneyt KARACAN for his patience to my questions.

Special thanks to my dear friends Tolga ÇAMLIKAYA, Gökçen BAŞ, Akın ACAR, Çağlar ÖZYURT and Serkan ŞEDELE for their great motivation and unforgettable friendship.

Finally I would like to thank my family for their precious support during all stages of my life.

TABLE OF CONTENTS

CHAPTER

LIST OF TABLES

TABLE

LIST OF FIGURES

CHAPTER 1

INTRODUCTION

1.1 Introduction

The theory of variable reluctance motors was established by 1838. but, these motors awake new interest since 1960's with the developments in electronics, especially due to inexpensive, high power switching devices. The term "Swiched Reluctance" defines not only the "Doubly Salient Motor" but also its drive.

First application areas investigated for these devices were positioning applications. In the early 1970's, it was noticed that doubly salient motors can be used for continuous variable speed applications.

Doubly salient motors, or "Switched Reluctance Motors" (SRM), have many advantages and some disadvantages against other types of motors. These advantages and disadvantages can be summarized as follows:

- Contrary to the case of AC machines, only one power switch is required to control phase current as the motor is insensitive to the direction of current.
- The inductance characteristic of the stator winding is dependent both on the rotor position and current. For this reason, a linear model with constant circuit parameters is not possible.
- SRM has a good starting torque,
- By changing the sequence of excitation, the direction of rotation can be reversed.
- It requires a controllable converter which is expensive for constant speed applications.
- The rotor structure is simple and easy to manufacture.
- Cooling is easy because, most of the heat is generated in stator.

- Because of the ripple on torque, SRM requires careful magnetic and controller design to minimize the ripple and acoustic noise.
- The cabling is more complex than induction motor drives.

Generally, SRMs are chosen for the applications where a brushless drive is required with a wide speed range, and also if the cost saving is important.

1.2 Basic Structure and Operating Principles of SRM

The most common stator-rotor pole numbers of SRMs are 8-6 and 6-4. Also, 4-2, 6-2, 10-4 and 12-8 are possible. Stator poles are wound oppositely to form a phase. Like step motors, SRMs have a step angle:

$$\alpha_S = \frac{2 \cdot \pi}{q \cdot N_r} \text{ rad} \tag{1.1}$$

where, q is the number of phases and N_r is the number of rotor teeth.

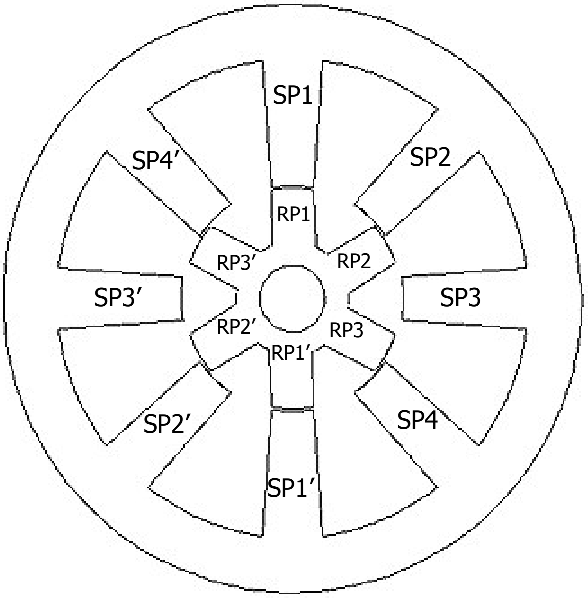

Figure 1–1: An 8-6 (4 Phase) SRM structure

Referring to Figure 1–1, the flux linkage and hence the permeance of pole pair SP1-SP1′ is maximum, while for the pole pair SP3-SP3′, it is minimum. The maximum permeance position is called as IN position, and the minimum permeance position is called as the OUT position.

The operation of the rotor movement is achieved by firing the successive phases sequentially. The rotor tends to align the excited stator pole pair to achieve maximum permeance. SRM drives determine the instant for the phase to be energized from the rotor position information taken from the position transducer. The instant at which the phase is excited is called as "Switch On" position. Likewise, the position at which the excitation is turned off is called as "Switch Off" position. The time passing between Switch On and Switch Off instants is called "Excitation Period". Due to the highly inductive equivalent circuit of SRM phase, the current can not fall to zero at Switch Off instant, and continues to flow over the freewheeling diode as the time constant of the phase winding permits, and drops to zero. The time at which the phase carries current is called the "Conduction period". The control of the SRM[5] is achieved by controlling the:

- Supply voltage,
- Switch On instant,
- Switch Off instant.

1.3 Application Considerations

Some of the advantages and disadvantages of SR motor are given in section 1.1. In the application point of view, advantages and disadvantages of converter and control of SRM should also be taken into account [5].

- It only requires unidirectional current to achieve four quadrant operation, resulting less than two switching devices per phase,
- No shoot through problem, assuring high reliability,
- Can continue operation even when a failure of one phase occurs,
- Reduced number of switches requirement reduces cost.
- Requires at least one current sensor sensing the DC link current, and one position transducer.

1.4 Existing Research in the Literature

In 1972, Byrne [30] investigated the tangential forces in overlapped geometries,
In 1974, Unnewehr and Koch [31], presented a disc type SRM,
In 1974, Chai [28] developed a method for calculating permeances of doubly salient structures by assuming some flux tubes between rotor and stator teeth,
In 1976, Blenkinsop [32] analyzed a 2 phase single stack SRM, without considering the magnetic saturation, but showed the basic design principles,
In 1977, Koch [33] developed linear methods in predicting the performance of SRMs,
In 1979, Corda and Stephenson [19], adopted the approach of Chai to predict minimum and maximum inductances of SRMs,
In 1979, Corda and Stephenson [1] proposed a method for the computation of torque and current in SRMs from non-linear magnetization data,
In 1980, Lawrenson, Stephenson, Blenkinsop, Corda and Fulton [12] published the basic structural and design principles,
In 1986, Ertan [2],[3], developed an accurate and fast method for permeance – tooth flux density, and torque – tooth flux density predictions of doubly salient structures, especially at intermediate rotor positions.
In 1985, Tohumcu [21], investigated the optimum design considering minimum weight of SRM in his Ph.D thesis, while considering the non-linear nature of the SRM in performance calculations.
Some of the recent studies are;
In 1993, Walivadekar, Athani and Acharya [34] published an equivalent circuit for SRM which is capable of explaining SRM operation in all four quadrants,
In 1995, Xu and Ruckstadter [35], coupled finite element analysis with power electronic circuit, and achieved transient analysis of SRM,
In 1996, Tang and Kline [36] published the studies on modeling and design optimization of SRM by boundary element analysis,
In 1996, Şahin [20], optimized the pole structure of SRM to reach minimum torque ripple, using neural networks,
In 1997, Ohdachi [37], realized an optimum design considering the pole shape of the motor for the minimum torque ripple, using dynamic finite element analysis,

In 2002, Miller [38], published basic rules for optimal design of SR motors, which reduces acoustic noise while achieving satisfactory performance,

There are many more papers on the issue but only some are investigated and reported here.

1.5 Objectives of the Study

The objective of this study is to develop a software which makes the steady – state analysis of a given SRM geometry under a given set of operating conditions like input voltage, chopper settings, rotor speed, etc. A further objective is to incorporate weight or cost optimization for a given set of constraints like efficiency, output power, etc. based on the analysis methods developed. While performing this job, an accurate and fast prediction of performance characteristics is required. These subjects will be discussed in detail in related chapters.

1.6 Contents of the Thesis

This study has two parts. In Chapter 2, the first part, the analysis method of SRM is explained including the mathematical model and solution algorithm. The analysis of SRM includes, "Average Torque", "Efficiency", "Total Losses", "Torque Ripple", and "Output Power" at given speed. To perform the analysis, a fast and accurate method to predict flux linkage characteristics of an SRM is given. In Chapter 3, modified analysis methods for optimization process, and the mathematical background of optimization algorithm are explained. In Chapter 4, the verification results of the methods proposed in Chapter 2 are given for a test motor. Once the accuracy of the analysis methods employed are established, the optimization results for two different SRMs are given in Chapter 4. Finally, in Chapter 5, conclusion of the study is covered.

CHAPTER 2

NON – LINEAR STEADY STATE MODELING AND ANALYSIS METHOD OF SWITCHED RELUCTANCE MOTORS

2.1 Introduction

Accurate prediction of the performance of a doubly – salient switched reluctance motor has been of interest in the past 20-25 years. Methods are developed based on the electromechanical nature of the motors. The simulation of SRM is more complex than AC or DC motors because of the nonlinear behaviour of the operating region of the motor. Mainly, three factors cause this nonlinearity:

- Magnetic materials used in the construction of SRM have nonlinear B-H characteristics,
- The flux linking the phases is dependent on both excitation level (current magnitude), and rotor position,
- Unlike separately excited DC or synchronous machines having two sources of excitation, SRMs have single source of excitation.

As stated in [1], pole flux linkage characteristics as a function of rotor position and excitation level should be known to calculate torque for a given speed. Typical flux linkage curves of an 8-6 SRM are shown in Figure 2–1. These characteristic curves can be obtained by:

- Using numerical field solution methods,
- Measurements,or
- Using analytical techniques.

For an optimization software, calculation of these characteristics should be as fast as possible. Field solution methods are known to be accurate but too slow to be used in an optimization process. Measurements give accurate results, but doing measurements on a motor which is at the design stage is out of question. Analytical methods are available, but these are not accurate. However, analytical approach based on numerically obtained normalized permeance versus position and tooth flux density has been developed [2] [3]. This method is shown to be quite accurate. In the optimization stage of this study, this approach shall be used.

This chapter is devoted to describing the methods used for the prediction of SR motors' performance assuming that "Flux linkage – Position – Current" data are available.

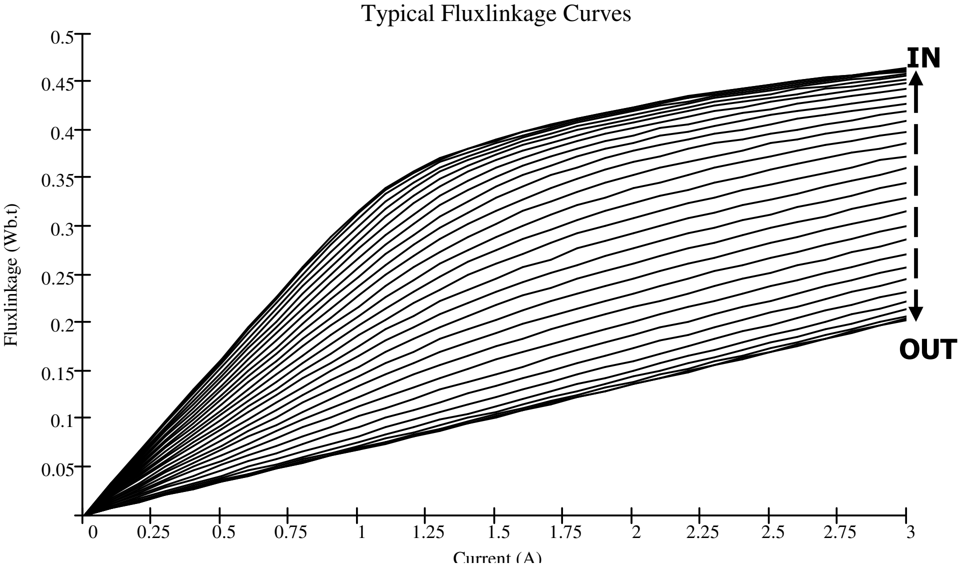

Figure 2–1: Typical flux linkage curves of an SRM, obtained by field solution using RM23 lamination characteristics.

Analysis of an SRM means obtaining steady – state or dynamic performance of the SRM. Some outputs of SRM analysis are:

- Average torque,
- Phase currents and current density,
- Output power, input power, and efficiency,
- Torque ripple,
- Total losses,

For

- given speed or speed range,
- Switch On and Switch Off positions, or Advance Angle and Excitation Period,
- DC supply voltage magnitude,

Current limit (Chopper drive is assumed in this study, see section 2.2.5).

In this study, the analysis part of the software performs steady – state performance calculations of the SRM. The functions and calculation methods of analysis part are also used for optimization part of the software. This study does not introduce a new performance calculation method of SRM, but presents a fast and accurate implementation of chosen methods from the literature. The verification of the chosen method will be given in Chapter4. As stated before, any analysis method for an SRM requires flux linkage data as a function of rotor position and excitation level to be given, as well as the chosen method. The analysis part of the software developed in this study either uses pre-measured data, or may predict the flux linkage data from user entered "Physical Data" and "BH characteristic" of any SRM. This prediction method will also be given in this chapter.

The topics of this chapter form the background of the overall study of performance analysis and design optimization of an SRM. Briefly, in this chapter:

- The performance calculation method chosen for the software will be explained,
- A method for analytical prediction of flux linkage data will be given.

The methods described here have been employed in a user friendly software developed in Microsoft Windows medium. The software is capable of analyzing the performance of an SR motor driven by a current – controlled voltage source converter. The software is also capable of designing an optimum SR motor using the optimization techniques described in Chapter 3.

2.2 Calculation of Steady – State Performance of an SRM

2.2.1 Introduction

As stated before, the electromechanical nature of SRM is both dependent on rotor position and excitation level. SRMs are often designed to operate into the saturation region of the magnetic material, so that the output torque is enhanced. In the literature, analysis methods are based on solving differential circuit equations of the motor. The voltage equation describing the electrical circuit of an SRM phase is:

$$\begin{matrix}+V\\0\\-V\end{matrix} = R\cdot i+\frac{d\lambda(\theta,i)}{dt} \tag{2.1}$$

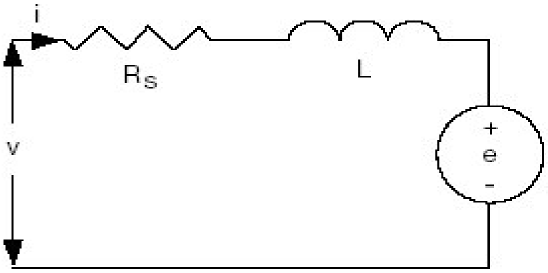

Figure 2–2: Equivalent circuit of single phase of an SRM

where, V is the input voltage, R is phase resistance, and λ is the flux linkage of the phase windings. *R.i* is the resistive voltage drop across the phase winding, and $d\lambda/dt$ is the rate of change of phase flux linkage, which is the sum of inductive voltage drop and back emf, *e*. The mechanical equations are as follows:

$$\frac{d\theta}{dt}=\omega \tag{2.2}$$

$$\frac{d\omega}{dt}=\frac{1}{J}\cdot\{T(\theta,i)-T_{mech}\} \tag{2.3}$$

where ω is the shaft speed, and *J* is the load and rotor inertia. T_{mech} in equation 2.3 represents the friction and load torques on the motor.

As stated in [1], the performance calculation requires to solve these first order differential equations. Stephenson and Corda, in [1], gave a brief literature search on the usage of equation 2.1. The possible forms of equation 2.1 are:

$$\frac{di}{dt} = \frac{1}{\frac{\partial \lambda}{\partial i}(\theta,i)} \cdot \left\{ \pm V - R \cdot i - \omega \cdot \frac{\partial \lambda}{\partial \theta}(\theta,i) \right\} \qquad \textbf{(2.4)}$$

$$\frac{di}{dt} = \frac{1}{l(\theta,i)} \cdot \left\{ \pm V - \left[R + \omega \cdot \frac{\partial L}{\partial \theta}(\theta,i) \right] \cdot i \right\} \qquad \textbf{(2.5)}$$

$$\frac{di}{dt} = \frac{1}{L(\theta,i)} \cdot \left\{ \pm V - \left[R + \omega \cdot \frac{\partial L}{\partial \theta}(\theta,i) \right] \cdot i \right\} \qquad \textbf{(2.6)}$$

where, $l(\theta,i)$ is named as the incremental inductance, because it is the ratio of incremental flux linkages to incremental excitation current [5].

From [1]:

- Singh [6], used the form 2.5, the fuctions $l(\theta,i)$, $L(\theta,i)$ and $T(\theta,i)$ were approximated by fundamental cosinusoidal components of θ and by linear functions of *i*, the derivatives $\frac{\partial L}{d\theta}(\theta,i)$ obtained analytically.

  $L(\theta,i) = \left\{ \int_0^i l(\theta,i) \cdot di \right\} / i$ and $T(\theta,i) = \partial \left\{ \int_0^i L(\theta,i) \cdot i \cdot di \right\} / \partial\theta$,

- Pickup and Tipping [7],[8], used the form 2.4. Flux linkage was measured at equally spaced angles and currents. They first approximates the $\lambda(\theta,i)$ function by polynomials in both θ and *i*, and later, by Fourier cosine series in θ and by polynomials in *i*. The derivatives $\frac{\partial \lambda}{d\theta}(\theta,i)$ and $\frac{\partial \lambda}{di}(\theta,i)$, and torque $T(\theta,i) = \partial \left\{ \int_0^i \lambda(\theta,i) \cdot i \cdot di \right\} / \partial\theta$ were found analytically.

- Byrne and Dwyer [9], used the form 2.4. Flux linkage was measured at equally spaced angles and currents. $\lambda(\theta,i)$ functions are fitted by a sum of three exponentials. $\frac{\partial\lambda}{di}(\theta,i)$ and $\int_0^i \lambda(\theta,i)\cdot di\big|_{\theta=cons\tan t}$ were obtained analytically and, $\frac{\partial\lambda}{d\theta}(\theta,i)$ and $T(\theta,i)=\partial\left\{\int_0^i \lambda(\theta,i)\cdot i\cdot di\right\}/\partial\theta$ were obtained numerically.
- Blenkinshop [10], used the form 2.6. Inductance was measured at equally spaced angles and unequally spaced currents. $L(\theta,i)$ functions are fitted polynomially, and values of co-energy $W^{'}(\theta,i)$ were found analytically and values of $\frac{\partial L}{d\theta}(\theta,i)\Big|_{i=cons\tan t}$ and $T(\theta,i)=\frac{\partial W^{'}(\theta,i)}{\partial\theta}\Big|_{i=cons\tan t}$ were obtained numerically.

In [1], it is clearly stated that the approaches listed below are not preferred because to fit magnetizing characteristics into polynomials, Fourier series or exponential functions introduce significant errors in analytical differentiation. Stephenson and Corda, propose a new method which is based on using non-linear differential functions. These equations do not require analytical differentiation and give more accurate results.

2.2.2 Formulation of Stephenson and Corda, and Implementation of the Algorithm

From [1], the excitation current is formulated as a function of rotor position and flux linkage, i(θ,λ), instead of λ(θ,i). With constant speed assumption, equation 2.1 takes the form:

$$V = R\cdot i(\lambda,\theta)+\omega\cdot\frac{d\lambda}{d\theta} \tag{2.7}$$

Taking the $\frac{d\lambda}{d\theta}$ term in the left hand side:

$$\frac{d\lambda(\theta,i)}{d\theta}=\frac{1}{\omega}\cdot\left[V-R\cdot i(\lambda,\theta)\right] \tag{2.8}$$

In this study, the numerical differential solution method Runge Kutta 4^{th} order is chosen to solve equation 2.8. The aim is to obtain the Flux linkage – Current locus of the active phase, as shown in Figure 2.3.

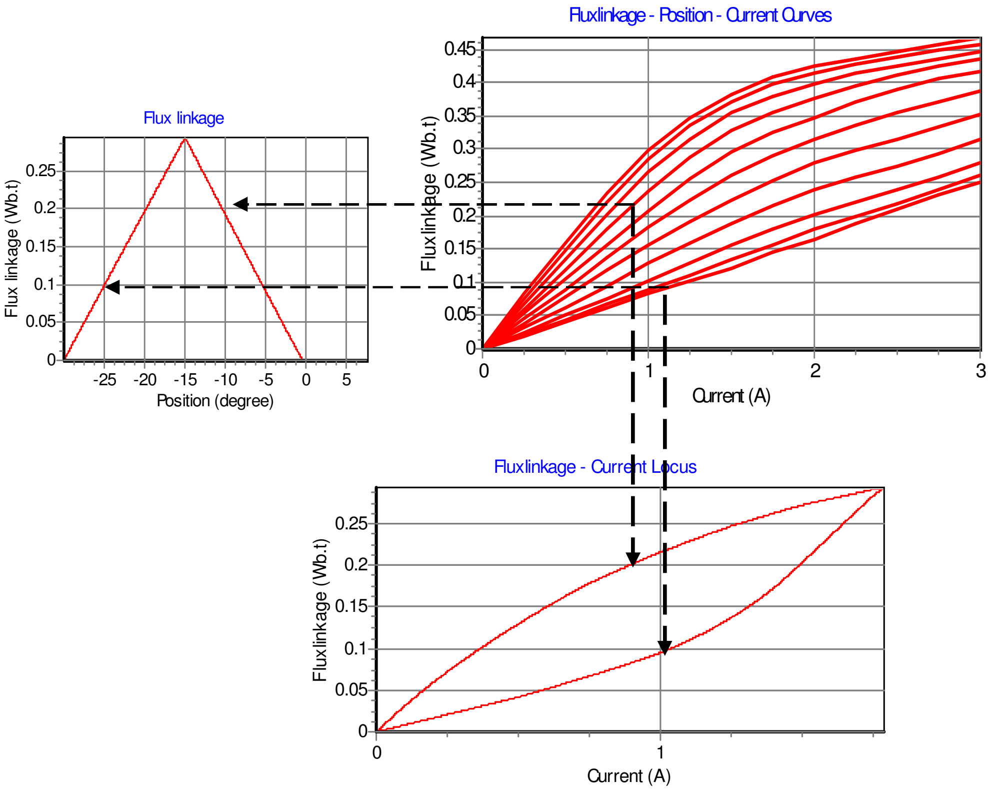

Figure 2–3: Graphical representation of the solution method

The flowchart of the Runge – Kutta 4th order algorithm is given in Figure 2.4, and the flowchart of the steady – state solution algorithm is given in Figure 2.6. The initial conditions are needed to solve the differential equation 2.8 by Runge – Kutta, these are:

- Input voltage, input to software by the user,
- Initial rotor position, which is also Switch on position, determined by the Advance Angle input to software by the user, as shown in Figure 2.5.

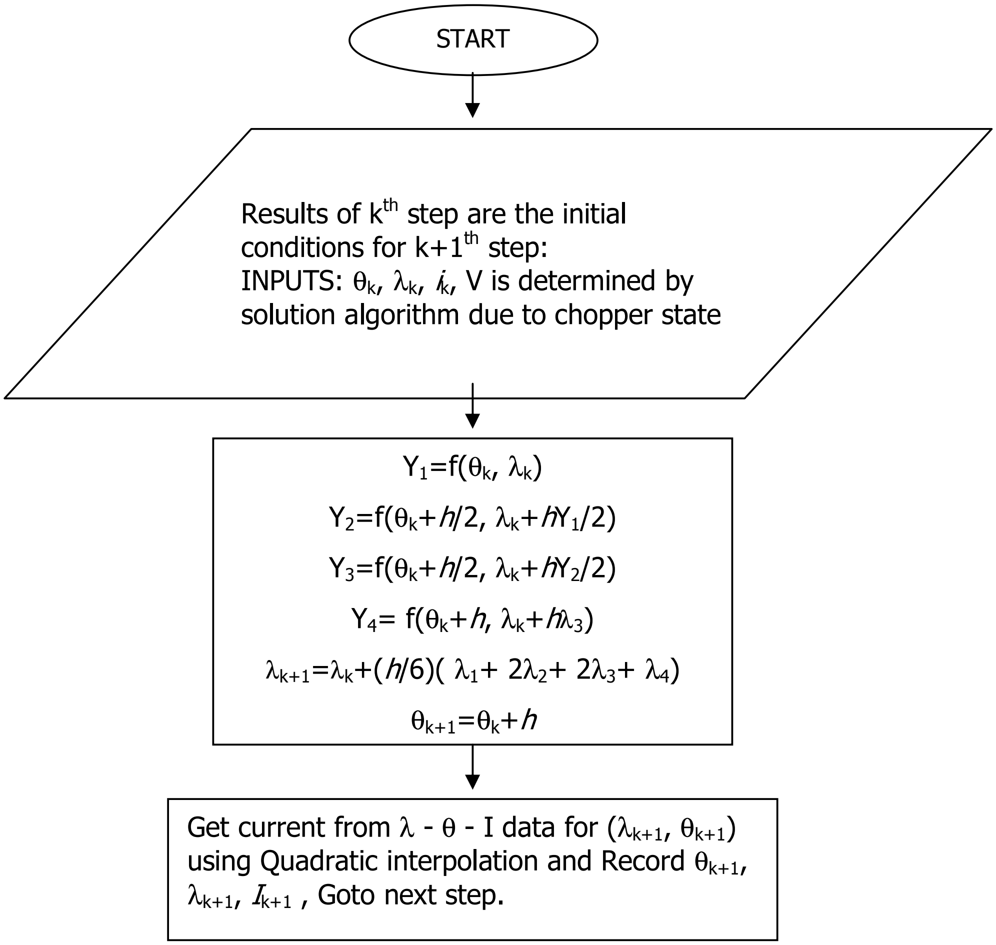

Figure 2–4: Flowchart of the RK 4th order algorithm and its implementation in the software

- Rotor speed, ω, input to software by the user,
- Phase resistance, input to software by the user,
- Initial current, taken as zero since at steady –state, the current of one phase decreases to zero until the next excitation of the phase comes again, as shown in Figure 2.12.
- Initial value of flux inkage is taken as zero for the same reason.
- Numerical differentiation step size, *h*, either may be input to software by user, or determined by the software taking rotor speed and excitation period into consideration. This step size should be as small as possible to reach

accurate results, but not to limit calculation speed. In the analysis part of the software the integration step size is:

$$h = \left| \frac{\theta_{ON} - \theta_{OFF}}{4000} \right| \tag{2.9}$$

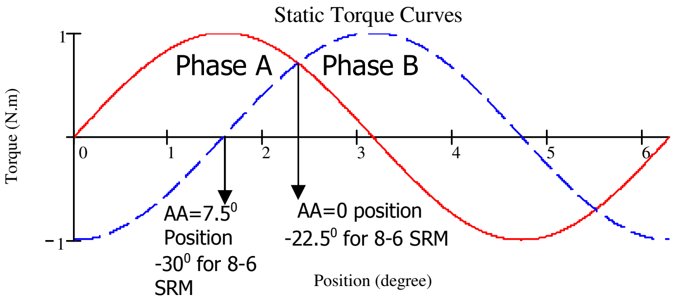

Figure 2–5: Static Torque Curves of two successive phases

At the end of the process we obtain:

- Current – Position (I - θ) waveform,
- Flux linkage – Position (λ - θ) waveform,
- Instantaneous Torque – Position (T - θ) waveform (See section 2.2.3),
- and, Flux linkage – Current (λ - I) locus.

In the following sections, obtaining the average torque produced by an SRM and its torque ripple will be described.

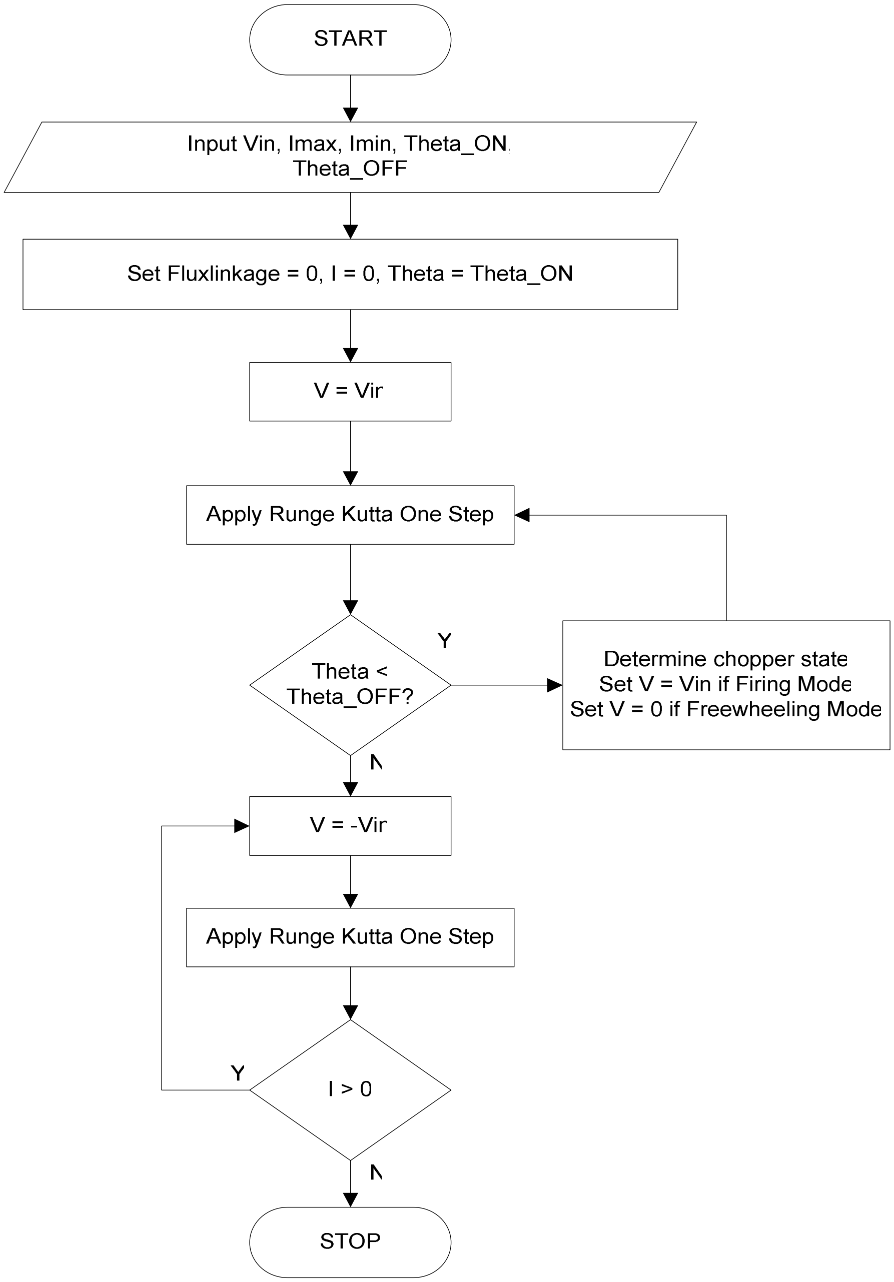

Figure 2–6: Flowchart of the solution algorithm

2.2.3 Obtaining the Instantaneous Torque Waveform

During the solution process, Instantaneous Torque – Position waveform is needed to be predicted, in order to calculate steady – state average torque and its torque ripple. This waveform is obtained using the equation, for one phase:

$$T(\theta) = \frac{\Delta W_C}{\Delta \theta} \tag{2.10}$$

where,

$$\Delta \theta = \theta_{k+1} - \theta_k \tag{2.11}$$

and,

$$\Delta W_C = (\lambda_{k+1} - \lambda_k) \cdot (i_{k+1} - i_k) \tag{2.12}$$

ΔW_C is the change in co-energy while rotor moves from θ_k to θ_{k+1}. This process is given in Figure 2.7.

Another method in obtaining the instantaneous torque is to use Static Torque curves of SRM if already available. This is possible since the author has access to a set of normalized Torque – Current – Position data [13], [42]. This approach however, is not preferred here, because this method requires the instantaneous torque value to be interpolated from the data for each current and rotor position values during the process, requiring extra computation time. Typical static torque curves are shown in Figure 2.8.

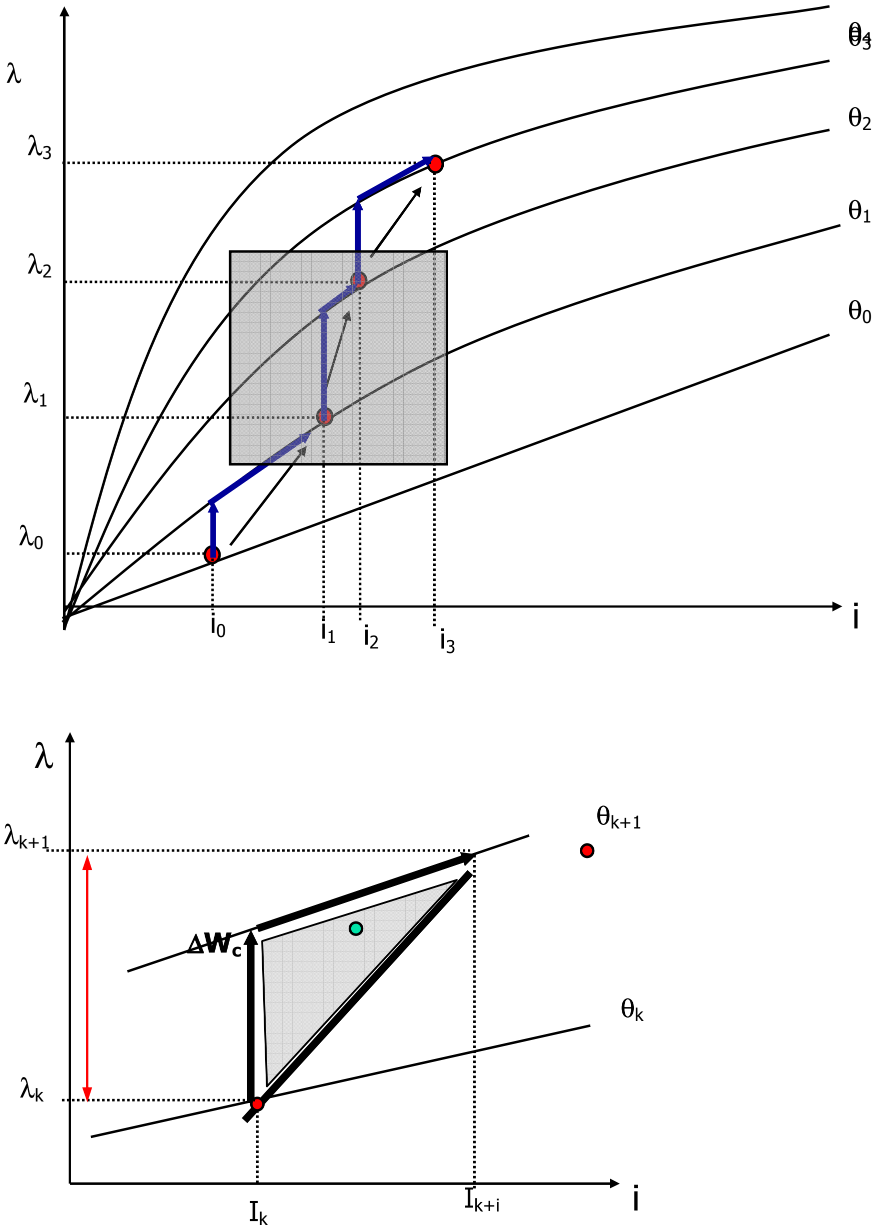

b)

Figure 2–7: Determination of instantaneous co-energy, and hence the torque.

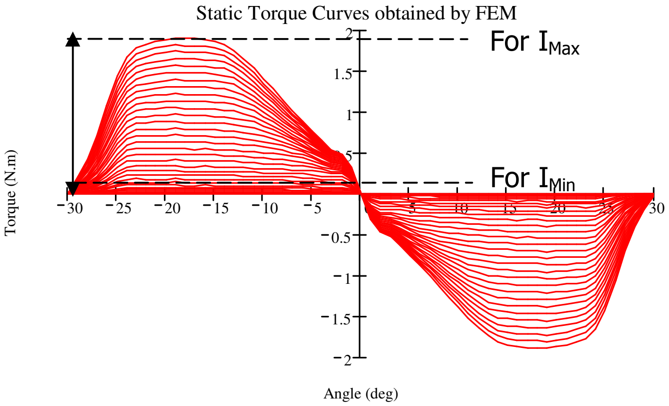

Figure 2–8: Typical static torque curves of an SRM, obtained by field solution using RM23 lamination characteristics.

Obtained waveforms are periodic for successive phases and resultant waveform is the sum of waveforms of all phases.

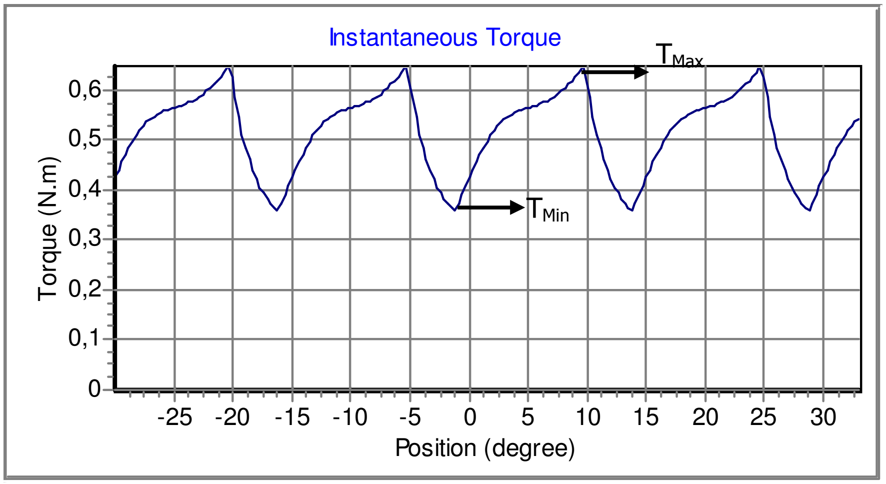

Figure 2–9: Resultant "Instantaneous Torque – Position waveform of an 8-6 SRM obtained at 2500 rpm with 7.5^0 Advance Angle

2.2.4 Calculation of Steady – State Average Torque and Torque – Ripple

In section 2.2.3, the method for obtaining instantaneous torque – position waveform is described. For a given geometry, the $T-\theta$ (or time) waveform is calculated and is stored as a data array in the software. Calculation of the "Average Torque" is done by taking the average of this data array over rotor tooth pitch (2 p.u. in normalized form).

To calculate the minimum and maximum torque points on this data array is an easy task. The minimum point is set as T_{Min}, and the maximum point is set as T_{Max}.(Figure 2.9) Then, the torque ripple is, by definition:

$$T_{ripple} = \frac{T_{\max} - T_{\min}}{T_{\max}} \% \tag{2.13}$$

2.2.5 Accounting for the Chopping Action

As seen from the flowchart of the method, the SRM is assumed to be driven by a chopper driver. A typical SRM converter with freewheeling and regeneration capability is shown in Figure 2.10 and Figure 2.11. There are four states of the chopper driver:

1. Conduction period, during this period T1 is ON, T2 is ON, $V = V_{in}$,
2. Free – wheeling period, during this period T1 is ON, T2 is OFF, V = 0
3. Fast – decay period, during this period T1 is OFF, T2 is OFF, $V = -V_{in}$.
4. Off state,

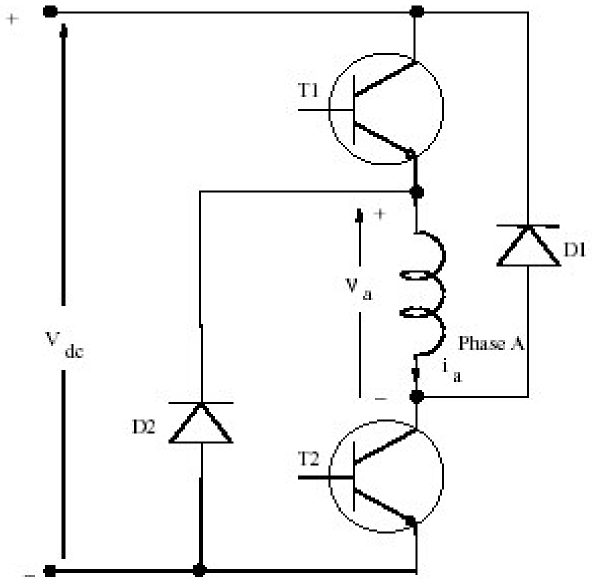

Figure 2–10: Asymmetric converter for one phase of SRM

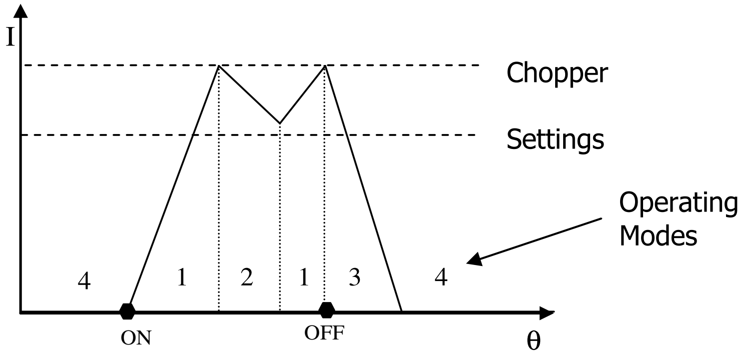

Figure 2–11: Operation of converter on phase current waveform

2.3 Calculation of Losses

In the design procedure of a motor, the thermal capability, hence the losses and cooling of the motor play an important role. In this study, an approximate calculation of SRM losses is investigated. SRM losses are mainly separated as Copper and Core losses.

2.3.1 Copper Losses

Copper losses are calculated using the formula:

$$P_{cu} = qI^2R_s \qquad \textbf{(2.14)}$$

where q is the number of stator phases, R_s is the per-phase resistance of stator winding, and I is the RMS value of the phase current. Calculation of I_{RMS} is an easy task since after the solution process given in Section 2.2, we have obtained a detailed Current – Position (I - θ)waveform as shown in Figure 2.12. Software calculates I_{RMS} using the definiton of RMS current:

$$I_{RMS} = \sqrt{\frac{\int_{X_{ON}}^{X_{ON}+T} I(\theta)^2 \, d\theta}{T}} \text{ A} \qquad \textbf{(2.15)}$$

on Current – Position waveform. The integration operation is given in Appendix B.1.

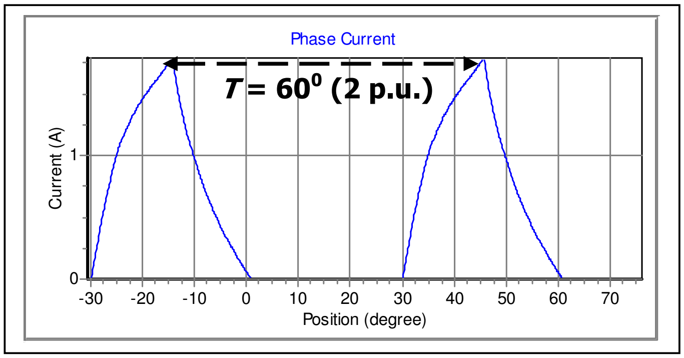

Figure 2–12: Current – position waveform of a 8-6 SRM, obtained at 2500 rpm with Advance Angle = 7.5^0.

2.3.2 Core Losses

In the study here, stator pole flux – position waveform for a given operating condition is obtained following the approach presented in section 2.2.2. Following this, the flux waveforms, and hence the flux density waveforms in various parts of the core can be found as described in the succeeding sections.

2.3.2.1 The Flux Waveforms

The issue of determining the flux waveforms in various parts of SRM has been of interest since the 80's [5], [11], [21]. In [21], Materu and Krishnan also deal with this problem for a 6-4 SRM. The flux waveforms of two succeeding phases are shown in Figure 2.13, in which, for the sake of simplicity, waveforms are assumed to be in triangular shape, and represented as the sum of Fourier series up to 20th harmonic. For an 8-6 SRM considering the periodicity of the waveforms, the following equations can be written for the pole flux waveforms of successive phases.

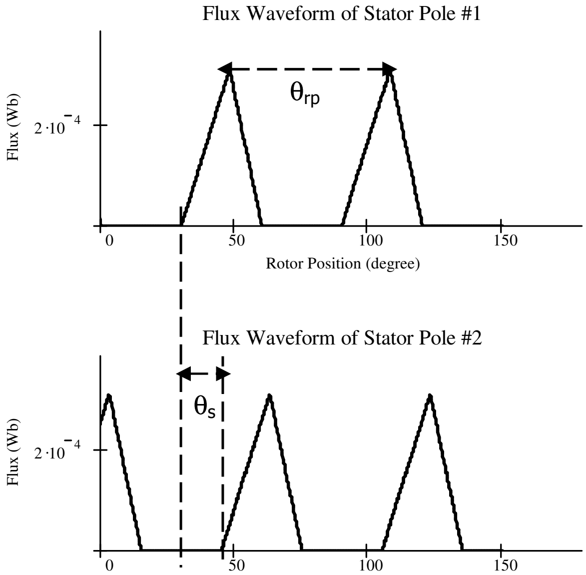

Figure 2–13: Periodic stator pole flux waveforms for a 4 phase SRM

For an 8-6 SRM:

Number of rotor teeth, $N_r = 6$,

Number of phases, $q = 4$,

Rotor tooth pitch, $\theta_{rp} = \dfrac{2\pi}{N_r}$,

Phase current displacement angle, $\theta_s = \dfrac{\theta_{rp}}{q}$,

$$\phi_{sp2}(\theta) = \phi_{sp1}(\theta - \theta_S) \quad \textbf{(2.16)}$$

$$\phi_{sp3}(\theta) = \phi_{sp2}(\theta - \theta_S) \quad \textbf{(2.17)}$$

$$\phi_{sp4}(\theta) = \phi_{sp4}(\theta - \theta_S) \quad \textbf{(2.18)}$$

Starting with the stator pole flux waveform in Figure 2.13, for the sample 8-6 motor, the back core flux waveform in section BC1 of an SRM can be found to be as shown in Figure 2.14.

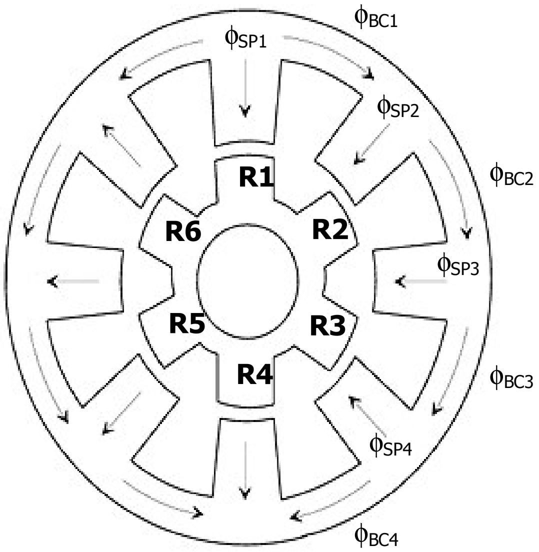

Figure 2–14: Core regions and related flux components for stator

$$\phi_{bc1}(\theta) = \frac{-1 \cdot \phi_{sp1}(\theta) + 1 \cdot \phi_{sp2}(\theta) + 1 \cdot \phi_{sp3}(\theta) + 1 \cdot \phi_{sp4}(\theta)}{2} \tag{2.19}$$

$$\phi_{bc2}(\theta) = \frac{-1 \cdot \phi_{sp1}(\theta) - 1 \cdot \phi_{sp2}(\theta) + 1 \cdot \phi_{sp3}(\theta) + 1 \cdot \phi_{sp4}(\theta)}{2} \tag{2.20}$$

$$\phi_{bc3}(\theta) = \frac{-1 \cdot \phi_{sp1}(\theta) - 1 \cdot \phi_{sp2}(\theta) - 1 \cdot \phi_{sp3}(\theta) + 1 \cdot \phi_{sp4}(\theta)}{2} \tag{2.21}$$

$$\phi_{bc4}(\theta) = \frac{-1 \cdot \phi_{sp1}(\theta) - 1 \cdot \phi_{sp2}(\theta) - 1 \cdot \phi_{sp3}(\theta) - 1 \cdot \phi_{sp4}(\theta)}{2} \tag{2.22}$$

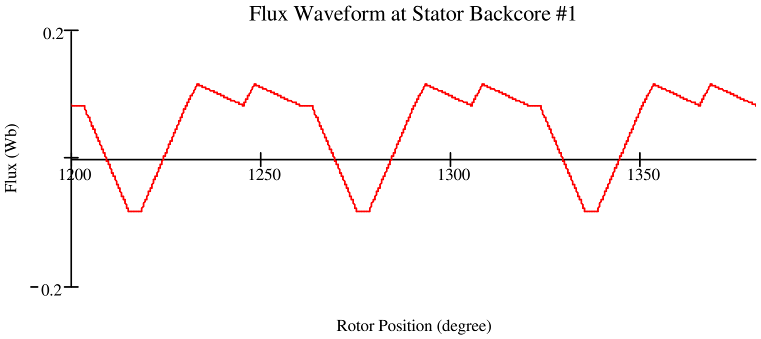

Figure 2–15: Sample flux waveform at stator back core #1

For an SRM, a pair of radially symmetric rotor teeth is at the same position under the corresponding stator poles. For example, in Figure 2.14, rotor teeth R1 and R4 are similarly aligned. Rotor tooth R1 experiences a similar flux waveform with a phase shift of θ_s due to successive stator poles, and the rotor pole flux reverses at every half revolution of the rotor as shown in Figure 2.16.

Similiar to stator back core, the flux waveforms at rotor back core segments can be obtained using rotor pole waveforms as shown in Figure 2.18.

$$\phi_{rc1}(\theta) = \frac{\phi_{rp1}(\theta) - \phi_{rp2}(\theta) - \phi_{rp3}(\theta)}{2} \tag{2.23}$$

$$\phi_{rc2}(\theta) = \frac{\phi_{rp1}(\theta) - \phi_{rp2}(\theta) + \phi_{rp3}(\theta)}{2} \tag{2.24}$$

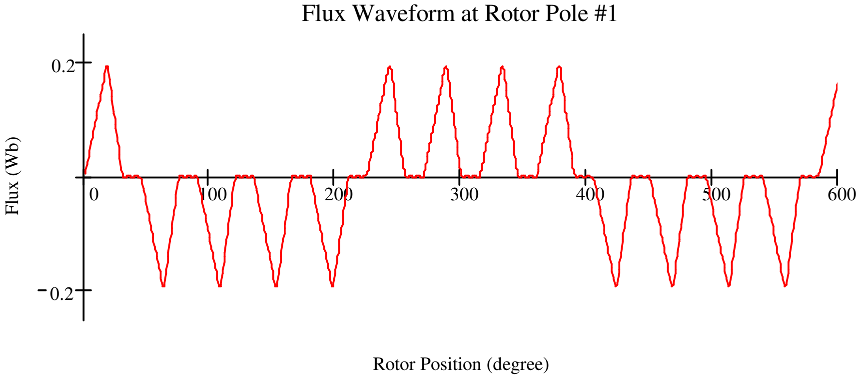

Figure 2–16: Sample flux waveform at Rotor pole #1

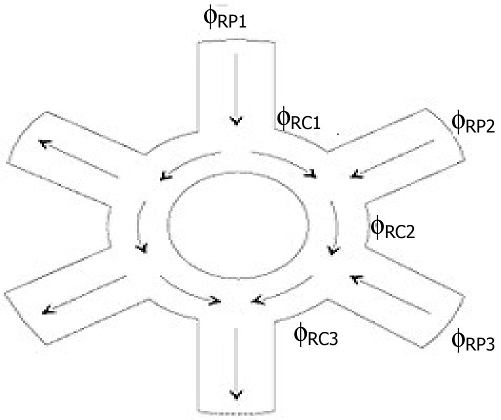

Fgure 2–17: Rotor core regions and related flux components for rotor

$$\phi_{rc3}(\theta)=\frac{\phi_{rp1}(\theta)+\phi_{rp2}(\theta)+\phi_{rp3}(\theta)}{2} \qquad \textbf{(2.25)}$$

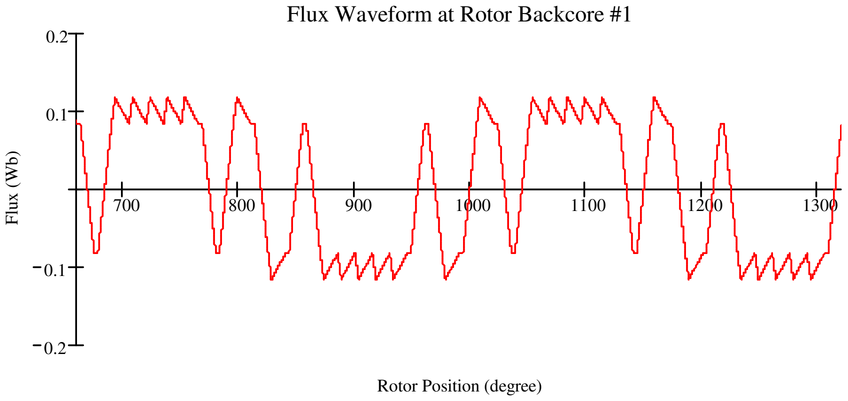

Figure 2–18: Sample flux waveform for rotor back core #1

2.3.2.2 Prediction of Core Losses from Obtained Flux Waveforms

In section 2.3.2.1, the flux waveforms at each core section are predicted starting from the stator pole flux waveform which is to be obtained after the process explained in section 2.2. Using the areas, where flux passes through, flux density waveforms for each core section can be obtained, later these flux density waveforms are expanded into Fourier series giving the magnitude and frequency for each harmonic. This is necessary to calculate core losses in order to use the "Watts per kilogram – Flux Density – Frequency" curves obtained from the lamination manufacturer. Typical loss curves are shown in Figure 2.19.

For the frequencies above or below supplied data range are found using extrapolation. As seen from the Figure 2-20, cubic spline interpolation method is suitable to extrapolate these values.

Note that, for example at 10000 rpm, each phase experiences a 1000 pulse per second waveform. In the core loss calculation, the harmonics of this waveform is considered. Obviously, higher frequencies shall occur, and for accurate calculations the loss curve should be available at those frequencies. Since the curves given are limited in frequency range, the accuracy of core loss prediction shall be low.

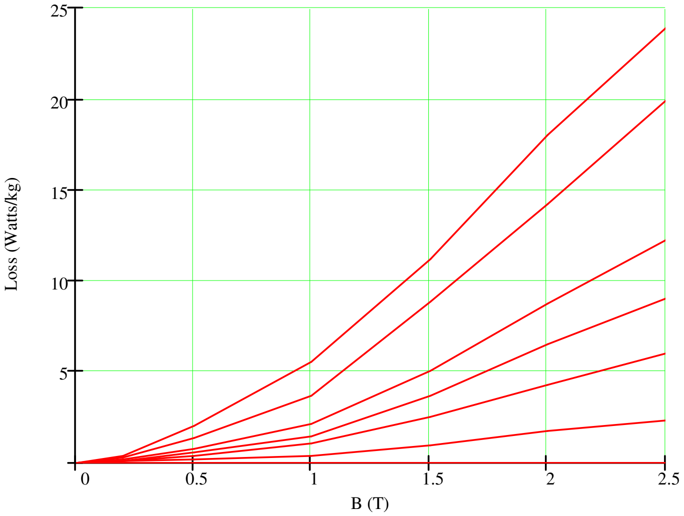

Figure 2–19: Loss curves used in software for RM23 Lamination

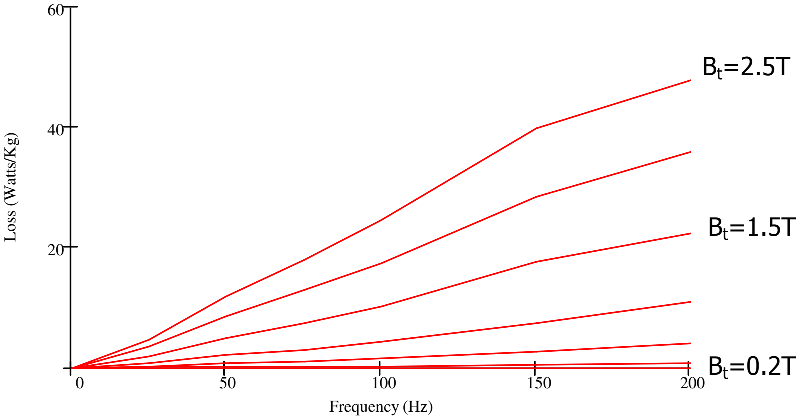

Figure 2–20: Loss curves, plotted against frequency

2.4 Prediction of Flux Linkage Characteristics of an SRM

2.4.1 Introduction

SRM performance can be predicted once the flux linkage characteristics, as a function of rotor position and excitation level are known. These charactersitics can be obtained from measurements or using field solution techniques, or using approximated analytical methods. Measured values are always preferable, but especially for an optimization process, it not possible. Field solutions give good results if the SRM structure is finely modeled, however two dimensional field solutions can not be accurate enough especially for the rotor positions close to the OUT position. Three dimensional field solutions may give as good results as measurements, but they require a large amount of time. So field solution technique, even 2 or 3 dimensional, is not suitable for design optimization, as the calculation of performance is required to be done many times during this process. Analytical methods for prediction of flux linkage characteristics are fast methods. However, their prediction and accuracy are often limited. In the literature; Corda and Stephenson [17], Krishnan [5] , Mukherji and Neville [13], Jones [27], Chai [28], and Ertan [2], [3], [4] have proposed valuable methods. In this study, the method of Ertan, which predict flux linkage curves from "Normalized Permeance Data" is used. These data are obtained from 2D field solutions and therefore are inherently more accurate, especially if corrected for the 3rd dimensional effects. These data are presented in normalized form and cover a wide range of variables. The properties and advantages of these methods and the data are:

- Characteristics of intermediate rotor positions can be predicted as well as IN and OUT positions.
- Intermediate value predictions are based on interpolation, hence, it is a very fast method
- Since the Permeance Data are obtained with normalized parameters, it is a universal method for various geometries of SR motors.

The data are obtained for normalized parameters of motor geometry. These are:

- λ/g = Rotor tooth pitch / air gap, (values 40, 70, 100, 150, 200, 250),
- t/λ = tooth width / tooth pitch, (values 0.3, 0.4, 0.5)

- X_n = Normalized positions of rotor, where X = 0 is IN position, and X_n = 1 is OUT position. (Values 0, 0.2, 0.4, 0.6, 0.8, 1)
- Data computed for λ = 0.0172 m, and core length L = 1m, and slot depth = 40.airgap.

So, for a given motor geometry, choosing the related tooth region permeance is a simple interpolation (or extrapolation) operation. For a given average tooth flux density, B_t and normalized position, X_n, the normalized permeance P_n, of the tooth region is a function of t/λ, and λ/g. So the actual permeance value can be deduced from normalized permeance using the formula:

$$P = \mu_0 \left(\frac{\lambda}{g} \right) L_C P_n \tag{2.26}$$

and corresponding tooth pitch flux, ϕ and MMF drops for this region, *F* are:

$$\phi = B_t t \tag{2.27}$$

$$F = \phi / P \tag{2.28}$$

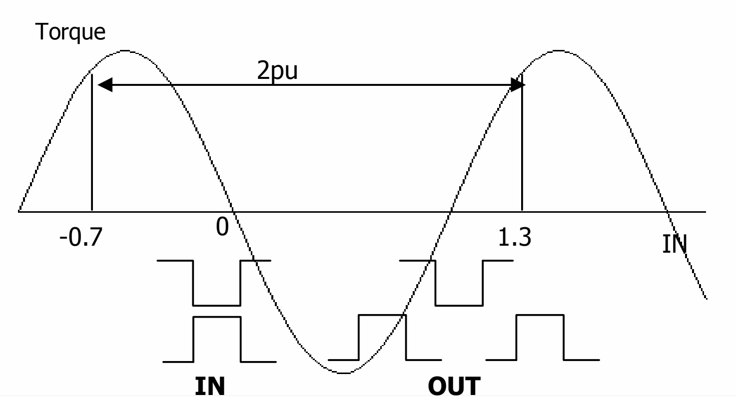

Figure 2–21: Graphical view of normalization on static torque waveform

Repeating this process for various values of B_t, at a given position, flux linkage vs. i (MMF) curve can be obtained. Repeating the procedure for other positions, a set of curves similar to Figure 2.1 can be obtained.

Normalization is a general definition which shows the relative position of rotor teeth with respect to the pitch of the stator poles. The rotor position is divided by the half of the Rotor Tooth Pitch, λ_r, to normalize this variable, since the behavior of the motor is symmetrical about the IN position.
For an SRM, e.g. with 6 rotor teeth:

$$\lambda_r = \frac{2\pi}{6} = 60^0,$$

IN Position: $\frac{0^0}{\lambda_r / 2} = 0$ p.u. and OUT Position: $\frac{30^0}{\lambda_r / 2} = 1$ p.u.

Intermediate positions between IN and OUT positions change from 0 to 1 p.u.

2.4.2 Asymmetrical Tooth Pairs Case

The permeance data are calculated for symmetrical tooth pairs, however, this is not the case in general, and that is, they have asymmetrical tooth pairs. In this situation, the method developed by Ertan [3] still may be is used. In this method, the normalized data for asymmetrical tooth pairs can be computed using the data of symmetrical tooth pairs, as shown in Figure 2.21. Two symmetrically slotted geometries, A and B, are obtained from the asymmetrically toothed geometry, one with tooth width = t_s and other with tooth width t_r. The tooth pitch of geometries A and B are:

$$\lambda_A = \max(\lambda_r, t_r + X_2 + 25g)$$
$$\lambda_B = \max(\lambda_r, t_s + X_1 + 25g) \quad \textbf{(2.29)}$$

The permeance of both geometries can be found from existing permeance data, and the permeance of the asymmetrically toothed geometry is:

$$Pn = \frac{2PnaPnb}{Pna + Pnb} \tag{2.30}$$

where, P_{na} and P_{nb} are the normalized permeance values of obtained symmetrical geometries A and B respectively. Once the normalized permeance of the asymmetrically slotted geometry is obtained, rest of the calculation of tooth region Flux – MMF calculations is same as given in previous section.

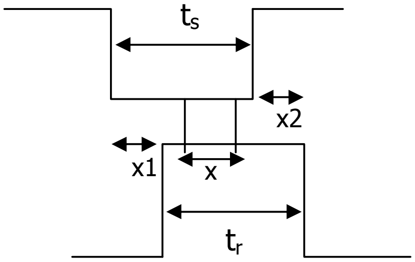

a) Asymmetrical geometry

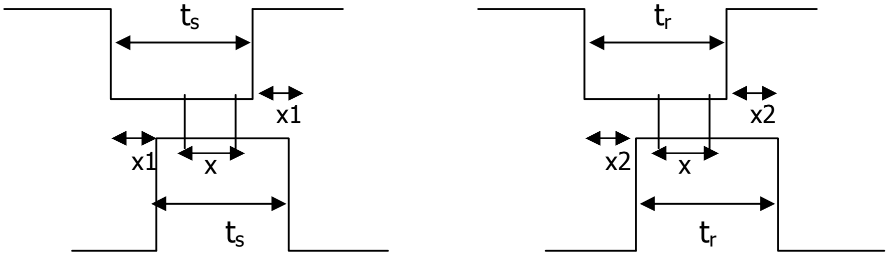

b) Geometry A **c)** Geometry B

Figure 2–22: Asymmetrical structure and related symmetrical structures

2.4.3 Back Iron Flux vs. MMF Drop Calculations

Back iron region is defined as the parts of the core other than the tooth region [2]. In the magnetic circuit of an SR motor, the MMF drop in the parts other than tooth region plays an important role. For a set of stator pole flux values, the MMF drops in the back iron region may be calculated, constructing a Flux – MMF curve (Figure 2.26). Obtained Flux – MMF curve is assumed to be independent of the rotor position. This obtained curve will be used in an operating point calculation

(See Section 2.4.4.), with the tooth region Flux – MMF curves for each rotor position respectively. This process is given in the following section.

In order to find Back iron MMF drop, we divide the core into several regions, as shown in Figure 2.23. These are:

- Stator back tooth(sbt): Remaining part of the stator poles from the tooth region,
- Rotor back tooth (rbt): Remaining part of the rotor tooth from the tooth region,
- Stator back core (sbc),
- Rotor back core (rbc).

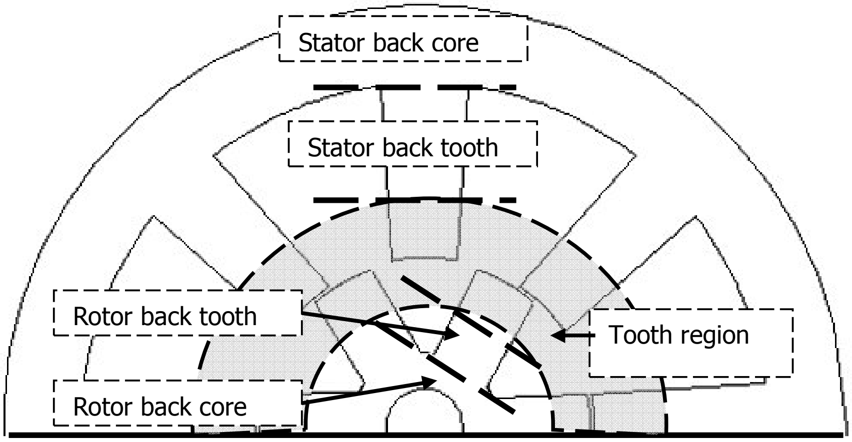

Figure 2–23: Back iron regions of an SRM

A "B" value is assumed for stator pole region. Total flux, ϕ_p, in this area is $B \cdot A_{SBT}$. The corresponding magnetic field intensity can be found by reading the "H" value for the chosen "B" value. The MMF drop in the particular region is $H_{SBT} \cdot l_{SBT}$, where l_{SBT} is the length of the flux path in the particular region.

The total MMF drop for the back iron is found by summing up the MMF drops of different regions in the back iron.

For each of the "B" points taken from the BH characteristic, by repeating this process for different values of "B", a Flux – MMF drop curve can be obtained:

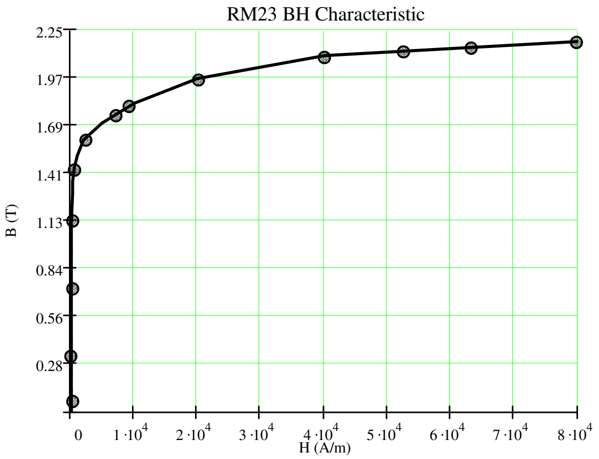

Figure 2–24: BH Characteristic of RM23 lamination

$$\phi_i = \frac{B_i}{t_s \cdot L_C}, \quad i = 1..N \tag{2.31}$$

where, $t_s \cdot L_C$ is the area for stator pole tip. Determination of back iron MMF drop for a given value of stator pole flux is given below.

2.4.3.1 Obtaining Flux – MMF Characteristics of Stator and Rotor Back Tooth Regions

Some SRMs are manufactured with a stator pole with tapering, so for an accurate approximation of the MMF drop in this region, this tapering should be taken into account. Figure 2.24 shows an approximated method, which uses the sum of small MMF drops of thickness Δh, which should be taken sufficiently small.

Assuming that the stator back tooth is divided into *n* pieces, then:

$$\Delta h = \frac{h_s - 40g}{n} \tag{2.32}$$

and the width of the m^{th} piece is:

$$t_i = t_s + 2m\Delta h \tan(a) \tag{2.33}$$

where "*a" is* the tapering angle as shown in Figure 2.25. So the total MMF drop across the tapered back tooth region is:

$$F_{sbt} = \sum_{i=1}^{n} H_i \Delta h \tag{2.34}$$

where, H_i can be found using the B-H curve.

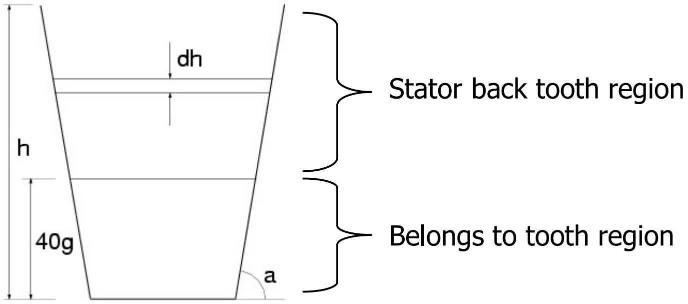

Figure 2–25: Tapering on stator pole

Assuming that the stator back tooth is divided into *n* pieces, then:

$$\Delta h = \frac{h_s - 40g}{n} \tag{2.35}$$

and the width of the m^{th} piece is:

$$t_i = t_s + 2m\Delta h \tan(a) \tag{2.36}$$

where "*a" is* the tapering angle as shown in Figure 2.25. So the total MMF drop across the tapered back tooth region is:

$$F_{sbt} = \sum_{i=1}^{n} H_i \Delta h \tag{2.37}$$

where, H_i can be found using the B-H curve.

If there is no tapering, the software simply takes the tapering angle as 0^0 and the number of pieces as 1.

$$B_{sbt} = \frac{\phi}{t_s L_c} \qquad \textbf{(2.38)}$$

Then find H_{sbt} from the B-H curve.

$$F_{sbt} = \int H_{sbt} dl = H_{sbt} \cdot (h_s - 40g) \qquad \textbf{(2.39)}$$

Likewise, the MMF drop in rotor back tooth region is found by:

$$B_{rbt} = \frac{\phi}{t_r L_c} \qquad \textbf{(2.40)}$$

then find H_{rbt} from the B-H curve.

$$F_{rbt} = \int H_{rbt} dl = H_{rbt} \cdot (h_r - 40g) \qquad \textbf{(2.41)}$$

where, h_s is the stator pole depth, and h_r is the rotor tooth depth.

2.4.3.2 Stator and Rotor Back Core Regions

Similar procedures are used in calculating the MMF drops of these regions.

$$B_{sbc} = \frac{\phi/2}{y_b L_c} \qquad \textbf{2.42}$$

then find H_{sbc} from the B-H curve.

$$F_{sbc} = \int H_{sbc} dl = H_{sbc} \cdot (\pi(Do - y_b)/2) \qquad \textbf{2.43}$$

where D_o is stator outer diameter, y_b is the stator back core width, and $(\pi(Do - y_b)/2)$ is the length of the flux path in the stator back core region.

$$B_{rbc} = \frac{\phi/2}{((d_o - d_a)/2) * Lc}$$ **2.44**

then find H_{rbc} from the B-H curve.

$$F_{rbc} = \int H_{rbc} dl = H_{rbc} \cdot (\pi((d_a + (d_o - d_a)/2)/2)$$ **2.45**

where d_o is rotor outer diameter, d_a is the shaft diameter, and $(\pi((d_a + (d_o - d_a)/2)/2)$ is the length of the flux path in the rotor back core region.

For a given point from the flux set extracted from the B-H curve, Total Back iron MMF drop is:

$$F_{Bi} = 2(F_{rbt} + F_{sbt}) + F_{rbc} + F_{sbc}$$ 2.46

MMF drops for the other points from the flux set are similarly calculated, forming the Flux – MMF curve.

2.4.4 Determination of Operating Point

For a given total MMF value, a simple operating point calculation between the tooth region and back iron characteristics is needed to find the flux passing through the poles. The operating point calculation is shown in Figure 2.26 graphically. In the software bisection method is used to approach required tooth region and back iron MMF drops to reach a total MMF excitation.

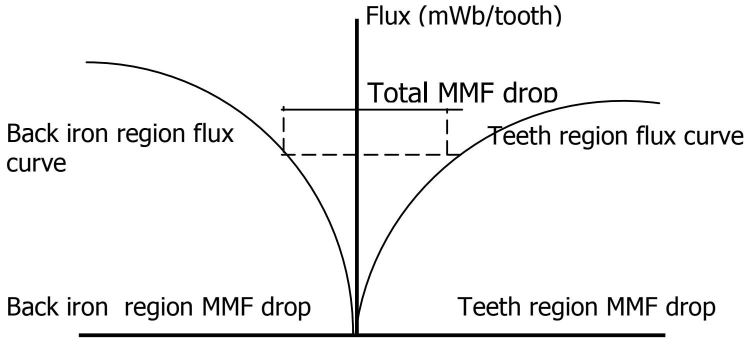

Figure 2–26: Graphical view of operating point calculation

2.4.5 Correction for End Leakage Flux

In the prediction of magnetizing curves, which are obtained using the Permeance Data, only a two dimensional field solution is taken into account. However, at the two ends of the core, flux leakage occurs, which are at significant amounts especially in small overlap positions. If this is not accounted for in predicting the flux linkage curves, significant erors occur in predicting the motor torque (see sections 4.3.3.1 and 4.3.3.2). To include this effect into flux linkage curves prediction method, some analytical methods are developed. These fast analytical methods are required since the approach of using three dimensional field solution requires a significant amount of computation time, and are not suitable for a quick design scheme, especially for an optimization algorithm.

The analytical method used in this study is based on the approach of Corda and Stephenson [19]. This approach is based on using Carter's coefficient [29], σ in order to obtain an effective core length, L_{cf}.

In this approach, side view of the magnetic circuit is considered. To account for the end leakage field, a series of infinitely permeable magnetic bodies of core length Lc are placed with a gap of *2n*. In this approach, *2n* must be chosen long enough in order not to cause a modification of individual leakage field of cores (Figure 2.27a). Figure 2.27b shows the equivalent magnetic circuit with core length L_{CF}, which accounts for the end leakage.

$$L_{cf} = L_c + 2n(1-\sigma) \quad \textbf{(2.47)}$$

$$\sigma = \frac{2}{\pi}\left\{\arctan\left(\frac{2n}{g_F}\right) - \frac{g_F}{4n} L_c n\left[1+\left(\frac{2n}{g_F}\right)^2\right]\right\} \quad \textbf{(2.48)}$$

where, σ is the Carter's coefficient, g_F is the effective air gap length, and *n* is the length where the magnitude of the end leakage fluxes in both sides drop to say 1% of its peak value. In this approach, the flux linkage is asumed to be proportional to the core length. So, the corrected flux linkage is:

$$\lambda_{3D} = \frac{L_{CF}}{L_C} \cdot \lambda_{2D} \quad \textbf{(2.49)}$$

where, λ_{3D} is the flux linkage taking into account the 3rd dimension.

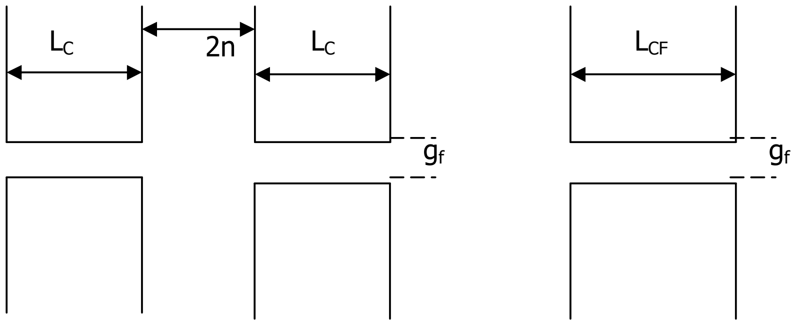

a) **b)**

Figure 2–27: a) Corda and Stephensons Model with mirror image to obtain an imaginary slotted geometry **b)** Equivalent unslotted geometry

This model requires a pair of rotor teeth to be in aligned position under the poles of excited phase. For the positions other than the IN position, this requirement is satisfied by representing the non-aligned rotor position by an IN position which has the same permeability at the t/λ, B_t and λ of the original structure. In this process, "g" is replaced by a virtual air gap g_f as shown in Figure 2.28. In the following section, the method of finding g_f is explained.

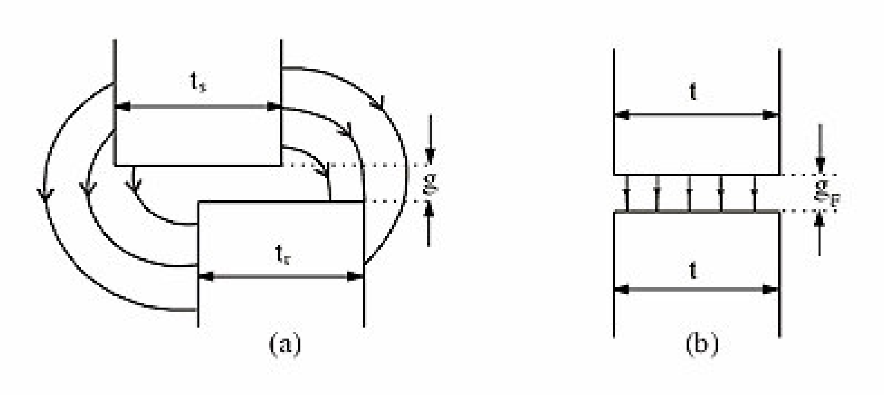

Figure 2–28: Actual model and equivalent model with fictitious airgap

2.4.5.1 Finding Equivalent Aligned Geometry for an Unaligned Position

For the positions other than IN position, an equivalent air gap length should be found, which represents the magnetic circuit of SRM in equivalent IN position. Considering the symmetrically toothed structures:

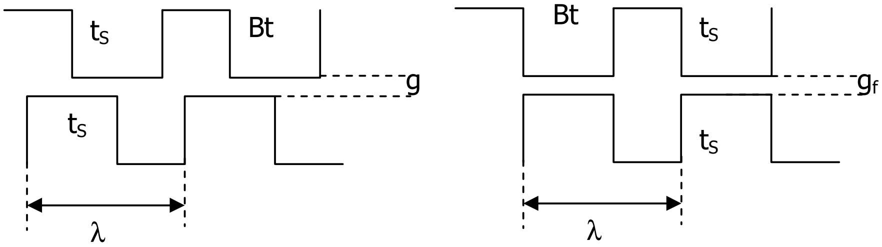

Figure 2–29: a) Rotor position 1, Xp1, **b)** Equivalent IN position representation

In this equivalent IN position representation, the physical parameters, "Tooth Pitch", λ, "Tooth Width", t, "Average Tooth Flux Density", Bt, and t/λ remain same. Only airgap length changes virtually. Hence there is a virtual change in λ/g value.

To determine g_f, the change in λ/g can be used. Since λ is constant during the process, after obtaining new λ/g value $(\lambda/g)_{NEW}$, g_f can be found using:

$$g_f = \frac{\lambda}{\left(\lambda/g\right)_{NEW}} \qquad \textbf{(2.50)}$$

At rotor position, Xp1, the tooth region has a permeance value. Since there is no physical change in equivalent IN position representation, this permeance should remain the same. So what needs to be done is to find an IN position equivalent, such that its permeance is the same as the permeance of the considered position, Xp1. If the variance of Permeance with respect to (λ/g) is known for the B_t value of Xp1, the $(\lambda/g)_{NEW}$ value can be interpolated for the permeance of Xp1. Since, in this study, the permeance data of Ertan [2], [42] are used, and these data are obtained for a range of λ/g, t/λ and B_t values, we have this Permeance – (λ/g) curves. A "Permeance – (λ/g) – B_t" matrix for the t/λ value of tooth structure, can be constructed from the permeance data easily, as shown in Figure 2.30.

For each of the t/λ values of normalized permeance data (t/λ=0.3, 0.4, 0.5), the "Permeance – (λ/g) – B_t" matrices are obtained by the software. After obtaining this three dimensional matrix (t/λ, λ/g, B_t), the steps in obtaining the required $(\lambda/g)_{NEW}$ value are given below:

- Interpolate "Permeance – (λ/g) – B_t" matrix to determine permeances at t/λ of the input motor geometry, as shown in Figure 2.30.
- For the B_t value of particular rotor position, interpolate "Permeance – (λ/g)" array from the obtained "Permeance – (λ/g) – B_t" matrix,
- Since permeance of original geometry and rotor position is assumed to remain same, $(\lambda/g)_{NEW}$ can be found by interpolating (λ/g) from the "Permeance – (λ/g)" array using the particular permeance value.
- After obtaining $(\lambda/g)_{NEW}$, equivalent air gap length is found by the software using the equation 2.47.

Equations 2.44~2.46 show that, determination of the effective end leakage distance "n" is also required. A method which uses the results of field solutions is developed for this study to determine "n". In the following section, this method is explained.

t/λ = 0.4	**λ/g=0**	**λ/g=40**	**λ/g=70**	**λ/g=100**	**λ/g=150**	**λ/g=200**	**λ/g=250**
Bt1	0	Permeance for λ/g=40 Bt=Bt1 Xn=0.0	Permeance for λ/g=70 Bt=Bt1 Xn=0.0	Permeance for λ/g=40 Bt=Bt1 Xn=0.0	Permeance for λ/g=150 Bt=Bt1 Xn=0.0	Permeance for λ/g=200 Bt=Bt1 Xn=0.0	Permeance for λ/g=250 Bt=Bt1 Xn=0.0
Bt2	0	Permeance for λ/g=40 Bt=Bt1 Xn=0.0	Permeance for λ/g=70 Bt=Bt1 Xn=0.0	Permeance for λ/g=40 Bt=Bt1 Xn=0.0	Permeance for λ/g=150 Bt=Bt1 Xn=0.0	Permeance for λ/g=200 Bt=Bt1 Xn=0.0	Permeance for λ/g=250 Bt=Bt1 Xn=0.0
Bt3	0	Permeance for λ/g=40 Bt=Bt1 Xn=0.0	Permeance for λ/g=70 Bt=Bt1 Xn=0.0	Permeance for λ/g=40 Bt=Bt1 Xn=0.0	Permeance for λ/g=150 Bt=Bt1 Xn=0.0	Permeance for λ/g=200 Bt=Bt1 Xn=0.0	Permeance for λ/g=250 Bt=Bt1 Xn=0.0
Bt4	0	Permeance for λ/g=40 Bt=Bt1 Xn=0.0	Permeance for λ/g=70 Bt=Bt1 Xn=0.0	Permeance for λ/g=40 Bt=Bt1 Xn=0.0	Permeance for λ/g=150 Bt=Bt1 Xn=0.0	Permeance for λ/g=200 Bt=Bt1 Xn=0.0	Permeance for λ/g=250 Bt=Bt4 Xn=0.0

Figure 2–30: Permeance – (λ/g) – Bt matrix constructed for the t/λ value of tooth structure

2.4.5.2 Determination of "*n*"

There are no known analytical methods to determine "*n*". 3D field solutions give accurate results, but they require a large amount of computation time. As an alternative, a normalized database for "*n*" may be constructed for the normalized parameters of Permeance Data. For this study, this database is constructed, using the professional field solution software ANSYS[39][40][41], for the normalized parameters:

- $\frac{\lambda}{g}$=40, 100 and 250,
- $\frac{t}{\lambda}$=0.3 and 0.5,
- X_n = 0.4, 0.8 and 1.0 p.u.

For each normalized parameter configuration, 2D and 3D models are constructed and solved at saturation level of stator pole. The magnitude of “*n*” values are calculated using the results of field solutions and the method described below. Steps of the method of determining “n” are given below:

I. 2D and 3D models are constructed for the same dimensional and magnetic properties. While determining the physical dimensions of constructed models, the air gap length is set as 0.25 mm, and kept constant. Field solution software considers a 1m of depth in the 3rd dimension by default. Hence, 2D field solutions are done considering a 1m of depth in Z-axis (core length). Because of this fact, 3D models are constructed with 1m of core length. 2D field solutions are required to determine the excitation level which achieves saturation level of tooth flux density(1.95 Tesla), and to record λ_{2D} values which will be used in the calculation procedure of “n”. Using the obtained excitation levels, 3D models are solved, and λ_{3D} values are recorded, which will be used in the calculation procedure of “n”.

II. For each geometry and rotor position, equivalent air gap lengths are computed using the methods given in section 2.4.5.1.,

III. The calculation method of “n” from field solutions is done using the equations 2.44~2.46. By substituting equations 2.44 and 2.45 into equation 2.46, an equation with only one unknown, which is “n”, is obtained:

$$\lambda_{3D} = \frac{\lambda_{2D}}{L_C} \cdot (L_c + 2n(1 - \frac{2}{\pi}\left\{ \arctan\left(\frac{2n}{g_F}\right) - \frac{g_F}{4n} L_c n\left[1 + \left(\frac{2n}{g_F}\right)^2\right]\right\})) \qquad \textbf{(2.51)}$$

Equation 2.48 is solved to find related “n” value and for all motor geometries and rotor positions specified, “*n*” data are obtained, which are presented in Table 2.1.

Table 2–1: Obtained data for “*n*”, g=0.25 mm, B_t = 1.95 T:

	λ/g=40		**λ/g=100**		**λ/g=250**	
Rotor position (p.u)	**t/λ=0.3 (p.u)**	**t/λ=0.5 (p.u)**	**t/λ=0.3 (p.u)**	**t/λ=0.5 (p.u)**	**t/λ=0.3 (p.u)**	**t/λ=0.5 (p.u)**
0.4	0.152 mm	0.223 mm	0.380 mm	0.452 mm	0.657 mm	0.925 mm
0.8	1.234 mm	1.345 mm	1.825 mm	2.123 mm	3.671 mm	4.986 mm
1.0	1.898 mm	2.876 mm	4.134 mm	5.135 mm	7.112 mm	9.321 mm

IV. Obtained “*n*” values are normalized with respect to g_F values found. Since the 3D field solutions are done at a relatively high saturation level, for the other excitation levels there are no data for “*n*”. This is the reason of selecting g_F as the normalization parameter, instead of actual air gap length, since calculation of g_F includes excitation level knowledge. Normalized “n” data are presented in Table 2.2.

Table 2–2: Obtained normalized data for “*n*”, normalization is done wrt g_f:

	λ/g=40		**λ/g=100**		**λ/g=250**	
Rotor position (p.u)	**t/λ=0.3 (p.u)**	**t/λ=0.5 (p.u)**	**t/λ=0.3 (p.u)**	**t/λ=0.5 (p.u)**	**t/λ=0.3 (p.u)**	**t/λ=0.5 (p.u)**
0.4	0.84978 p.u.	0.84952 p.u.	1.19290 p.u.	1.42632 p.u.	1.87878 p.u.	2.56731 p.u.
0.8	3.48717 p.u.	4.35698 p.u.	2.35486 p.u.	3.91481 p.u.	3.16505 p.u.	6.59960 p.u.
1.0	7.04557 p.u.	9.23274 p.u.	5.33014 p.u.	8.34417 p.u.	5.67437 p.u.	8.14986 p.u.

V. For the motor to be analyzed, the value of "*n*" can be found from the normalized data for "*n*".

VI. For asymetrically slotted structures, first the two symmetrical geometries are constructed as in section 2.4.2. then "n" values for each of these symmetrical geometries are determned from the normalized "n" data. Hence new L_{CF} value is found. The permeance i then determined for this core length.

VII. Although the "n" data are normalized with g_F, a detailed study which also considers the excitation level is needed for more accurate results.

2.4.5.3 Validity of "n" Data

In the previous section, a normalized "n" data are obtained. The field solution models are constructed for a core length of 1m. However, for most of the motors, core lengths are smaller. In order to investigate the validity of "n" data, for the test motor, SR2, which has a core length of 40 mm, 3D models are constructed and solved at a saturation level of 1.95 T, for normalized rotor positions X_n = 0.0, 0.2, 0.4, 0.6, 0.8 and 1.0. "n" values for SR2 are obtained from these 3D field solutions and compared with the "n" values found from the "n" database. By this way, the effect of core length on "n" is investigated. Results are given below in Table 2.3.

Table 2–3: The effect of core length on "n", MMF=966 A.t.

	λ_{2D_FEM} (Wb) For SR2	**λ_{3D_FEM} (Wb) for SR2**	**n_{40mm} (mm) from FEM for SR2**	**n_{1m} (mm) from data**	**%err**
X_n = 0.0	0.46314	0.4633	0.00348	0.001 arbitrary	-
X_n = 0.2	0.45196	0.45672	0.11	0.139	20.86
X_n = 0.4	0.40863	0.41626	0.2	0.278	28
X_n = 0.6	0.32976	0.3524	0.87	0.917	5.12
X_n = 0.8	0.24459	0.27232	1.54	1.557	1.09
X_n = 1.0	0.20218	0.2435	3.26	3.295	1.06

$$\%err = \frac{n_{1m} - n_{40mm}}{n_{1m}} 100 \qquad \textbf{(2.52)}$$

The percentage errors between n$_{40mm}$ and n$_{1m}$ are seemed to be quite small except for the normalized rotor positions 0.2 and 0.4 p.u. A more detailed comparison is needed, which compares the predicted flux linkage curves with end leakage correction done both by using n$_{40mm}$ and n$_{1m}$. Table 2.4 presents such a comparison with percentage errors based on measured values.

Table 2–4: The effect of core length on "n"

Xn (p.u)	**Predicted λ no correction (Wb)**	**λ$_{meas}$ (Wb)**	**Predicted λ corrected with n$_{1m}$ (Wb)**	**%err1 wrt λ$_{meas}$**	**Predicted λ corrected with n$_{40mm}$ (Wb)**	**%err2 wrt λ$_{meas}$**
0.0	0.46	0.468	0.46005	1.69812	0.46016	1.67521
0.2	0.443	0.446	0.44883	-0.63453	0.44767	-0.37444
0.4	0.41	0.417	0.42035	-0.80336	0.41765	-0.15588
0.6	0.34	0.353	0.36429	-3.1983	0.36334	-2.92918
0.8	0.264	0.28	0.29416	-5.05714	0.29393	-4.975
1.0	0.206	0.251	0.24837	1.04781	0.2481	1.15538

$$\%err1 = \frac{\lambda_{Meas} - \lambda_{n1m}}{\lambda_{Meas}} 100 \qquad \textbf{(2.53)}$$

$$\%err1 = \frac{\lambda_{Meas} - \lambda_{n40mm}}{\lambda_{Meas}} 100 \qquad \textbf{(2.54)}$$

In view of the results shown in Tables 2.3 and 2.4, it can be concluded that, the normalized "n" data obtained for a 1m core length can be used for including the end leakage effect, irrespective of the actual core length of the motor for which permeance predictions are made.

2.5 Conclusion

In this chapter, the mathematical background of analyzing an SRM considering the non-linear nature and saturation of the motor is given. As stated in section 2.2, the analysis method which predicts the average torque at given rotor speed requires the flux linkage characteristics as a function of excitation level and rotor position should be known. Section 2.4 explains the methods used here for predicting these data if not already available. The prediction methods are based on the usage of a normalized data of permeance. These data are obtained by 2D field solutions for the tooth region of SRM and cover a wide range of motor geometry. However, the effect of the leakage flux at the two ends of the core should be taken into account. Section 2.4.5 explains a method developed for correcting the 2D data for end leakage flux. In section 2.3, calculation methods of losses, including copper and core losses are given. Calculation of losses is required to determine the efficiency.

The methods developed in this chapter however, need to be tested to determine whether they are acceptably accurate. Both the approach used for prediction of the flux linkage – current – position curves and the performance prediction methods are compared with measurement results in Chapter 4.

CHAPTER 3

OPTIMIZATION

3.1 Introduction

As stated before, one of the aims of this study, is to develop a software which can achieve design optimization. In Chapter 2, calculation methods of performance functions are given in detail, and the optimization module will use the same procedures. However, it is found to be advantageous to make some modifications on calculation of steady – state torque in order to speed up process, and to guarantee the required conduction period (See section 3.8.1). These modifications will be described in following sections.

The function to be minimized is chosen as the weight (or the cost) of SRM. Constraints are often placed on physical dimensions, and the performance of the motor; such as, steady – state average torque, efficiency, minimum possible air gap length, during the optimization process. These criteria make the problem a constrained optimization problem. Throughout this chapter, the formulation of the constraint optimization problem will be given.

The constrained optimization problem is first converted to an unconstrained problem using the Augmented Lagrangian method. This process is also described in this chapter. The solution of the unconstrained problem and the search algorithm are also discussed in the following sections.

Optimization process is applied at two speeds, for a washing machine application. One at low speed, 520 rpm (SRM named as SRWash), other at high speed, 12000 rpm (SRM named as SRSpin), with their average torque and efficiency requirements. The results of these optimization processes will be given in Chapter 4.

3.2 Constrained Optimization Problem

A typical constrained optimization problem has a general form which can be formulated as [20]:

Minimize

$$
\begin{aligned}
& f(\bar{x}) \\
& \text{Subject to} \quad p_i(\bar{x}) = a_i \ \text{ for } i = 1,....,m_1 \\
& \qquad\qquad\quad\ q_i(\bar{x}) \le b_i \ \text{ for } i = 1,....,m_2 \\
& \qquad\qquad\quad\ \bar{x} \in X \subset R \\
& \qquad\qquad\quad\ c_k \le x_k \le d_k \ \text{ for } k = 1,....,n
\end{aligned}
\qquad \textbf{(3–1)}
$$

where:

- $f(\bar{x})$ is the function to be minimized, the objective function,
- $p_i(\bar{x})$ are the equality constraint functions,
- $q_i(\bar{x})$ are the inequality constraint functions,
- $\bar{x}$ is the search vector, vector of independent optimization parameters in terms of the cost function and constraints can be computed.

The constraints determine a feasible region and forces the optimum search vector to be in this region. One of the most common method for constrained optimization problem is the Augmented Lagrangian Method, which is the combination of Lagrangian and Penalty methods. In this study, this Augmented Lagrangian Method is chosen for the reasons:

- This method has been used in the Electrical Machines group of METU several times in the past for machine design optimization problems [21], [43],
- The algorithm is easy to implement [20].

3.3 Augmented Lagrangian Method

Constrained optimization algorithms convert the problem into an unconstrained form which the constraints are imposed into this form. The

Lagrangian method adds the equality and inequality constraints to the objective function, by multiplying with Lagrangian Multipliers, and forms the Lagrangian Function, then minimizes this unconstrained function:

$$L(\overline{x},\overline{\alpha},\overline{\beta}) = f(\overline{x}) + \sum_{i=1}^{m1} \alpha_i \cdot (a_i - p_i) + \sum_{i=1}^{m2} \beta_i \cdot (b_i - q_i) \quad \textbf{(3–2)}$$

where α and β are equality and inequality constraint Lagrange multiplies respectively.

The penalty methods eliminate some or all of the constraints. They add a penalty term to the objective function, this penalty term satisfies a high cost to infeasable points. As the penalty term increases, the unconstrained problem approximates to the original constrained problem[22].

The Augmented Lagrangian form [20], which is the combination of lagrangian and Penalty methods may be defined in the form:

$$L_a(\overline{x},\overline{\alpha},\overline{\beta}) = f(\overline{x}) + \overline{\alpha}^T \cdot (\overline{a} - \overline{p}) + \overline{\beta}^T \cdot (\overline{b} - \overline{q}) - w_1 p_1 - w_2 p_2 - w_3 p_3 \quad \textbf{(3–3)}$$

where:

- $w_i > 0$ are penalty weights,
- α^T and β^T are Lagrangian multiplier vectors for equality and inequality constraints respectively,

$$p_1 = \sum_{i=1}^{m1} (a_i - p_i)^2 \quad \textbf{(3–4)}$$

$$p_2 = \sum_{j \in C_a} (b_j - q_j)^2, \; C_a = \{j : \beta_j > 0\} \quad \textbf{(3–5)}$$

$$p_3 = \sum_{j \in C_b} (b_j - q_j)^2, \; C_b = \{j : \beta_j = 0, and, q_j \geq b_j\} \quad \textbf{(3–6)}$$

where $p_i = p_i(x)(i = 1,2,.....,m_1)$ and $q_j = q_j(x)(j = 1,2,.....,m_2)$.

The gradient of the augmented Lagrangian function is:

$$\nabla L_a = \nabla f(x) + \sum_{i=1}^{m1} \alpha_i^+ \nabla p_i + \sum_{i=C_a} \beta_j^+ \nabla q_j + \sum_{j=C_b} 2w_3 (b_j - q_j) \nabla q_j \tag{3–7}$$

where ∇p_i and ∇q_j are equality and inequality constraints gradient terms.

After the end of mth minimization phase, the multipliers are updated to satisfy $\nabla L = 0$. So that:

$$\nabla L(x^m)_{New} = \nabla L_a(x^m)_{Old} \approx 0 \tag{3–8}$$

To satisfy equation 3.8, equality and inequality multipliers are updated as the optimization progresses. For equality constraints:

$$\alpha_i^+ = \alpha_i - 2w_1 [a_i - p_i(x^m)], \; i = 1,2,...m_1 \tag{3–9}$$

For inequality constraints:

If $j \in C_a$, then;

$$\beta_j^+ = \begin{Bmatrix} 0, if \quad \beta_j - 2w_2 \lfloor b_j - q_j \rfloor \leq 0 \\ \beta_j - 2w_2 [b_j - q_j], \quad otherwise \end{Bmatrix} \tag{3–10}$$

If $j \in C_b$, then;

$$\beta_j^+ = \begin{Bmatrix} 0, if \quad \lfloor b_j - q_j \rfloor \leq 0 \\ 2w_3 [b_j - q_j], \quad otherwise \end{Bmatrix} \tag{3–11}$$

During this update process, the "w" values are the values used in the previous step, and after the update of β values, the sets C_a and C_b are also updated. Penalty weights are updated according to the rule

$$w_i^+ = \begin{cases} w_{i\_\max}, & if \quad \gamma \cdot w_i \geq w_{i\_\max} \\ \gamma \cdot w_i, & otherwise \end{cases}, \; i = 1,2,3 \tag{3–12}$$

where, γ is the penalty weight increment factor.

Selection of initial penalty weights is an important subject. They should be large enough to avoid constraint breakthroughs, but not too large in order not to confine solution path. In this study, after several tries, initial penalty weights are chosen as:

$w_1 = 1$, $w_2 = 2$, $w_3 = 2$, and $\gamma=4$ with $w_{i\_max} = 32$.

3.4 Search Method to Minimize Augmented Lagrangian Function

In this study, the Davidson – Fletcher – Powell (DFP) method [20] is used to search for the minimum because of the following reasons:

- Search directions are always guaranteed to be in the direction of descent,
- It requires only the first order partial derivatives, the gradient, of the function to be minimized
- Starting from any positive definite matrix, the generated positive definite matrices converge to the actual inverse Hessian at the solution point.

Flowcharts of the DFP method and the general optimization algorithm are given in Figure 3.1 and Figure 3.2. The complete flowchart of the Augmented .Lagrangian method can be found in [20].

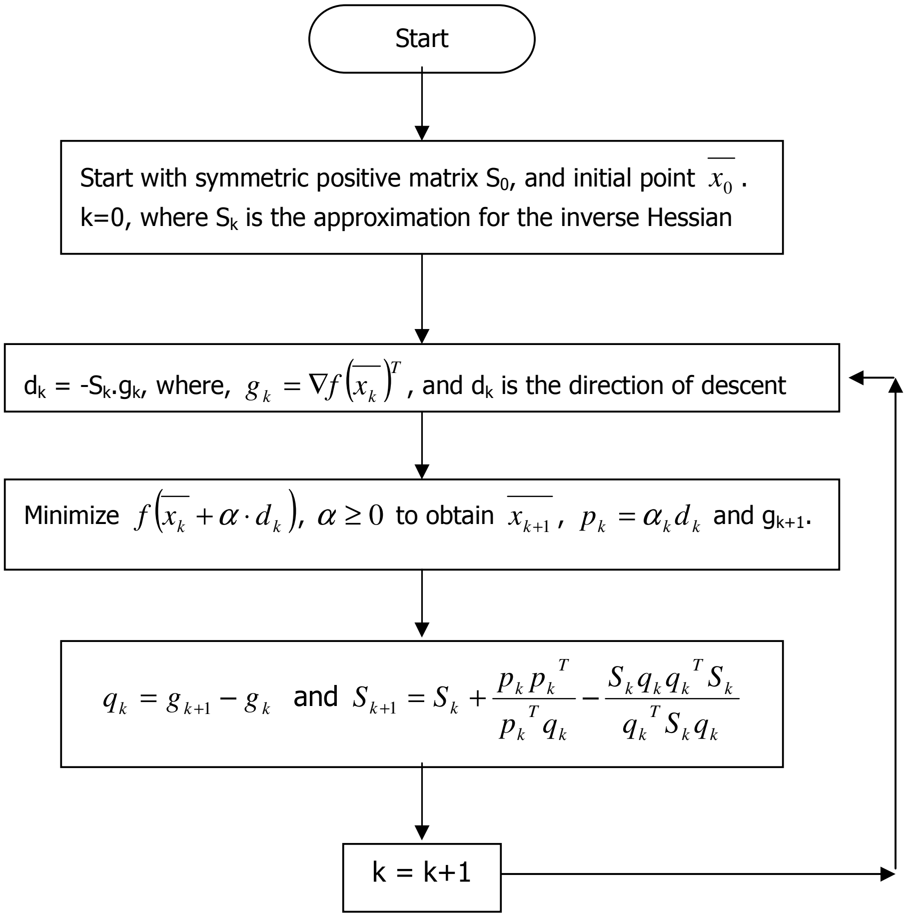

Figure 3–1: Flowchart of the DFP method

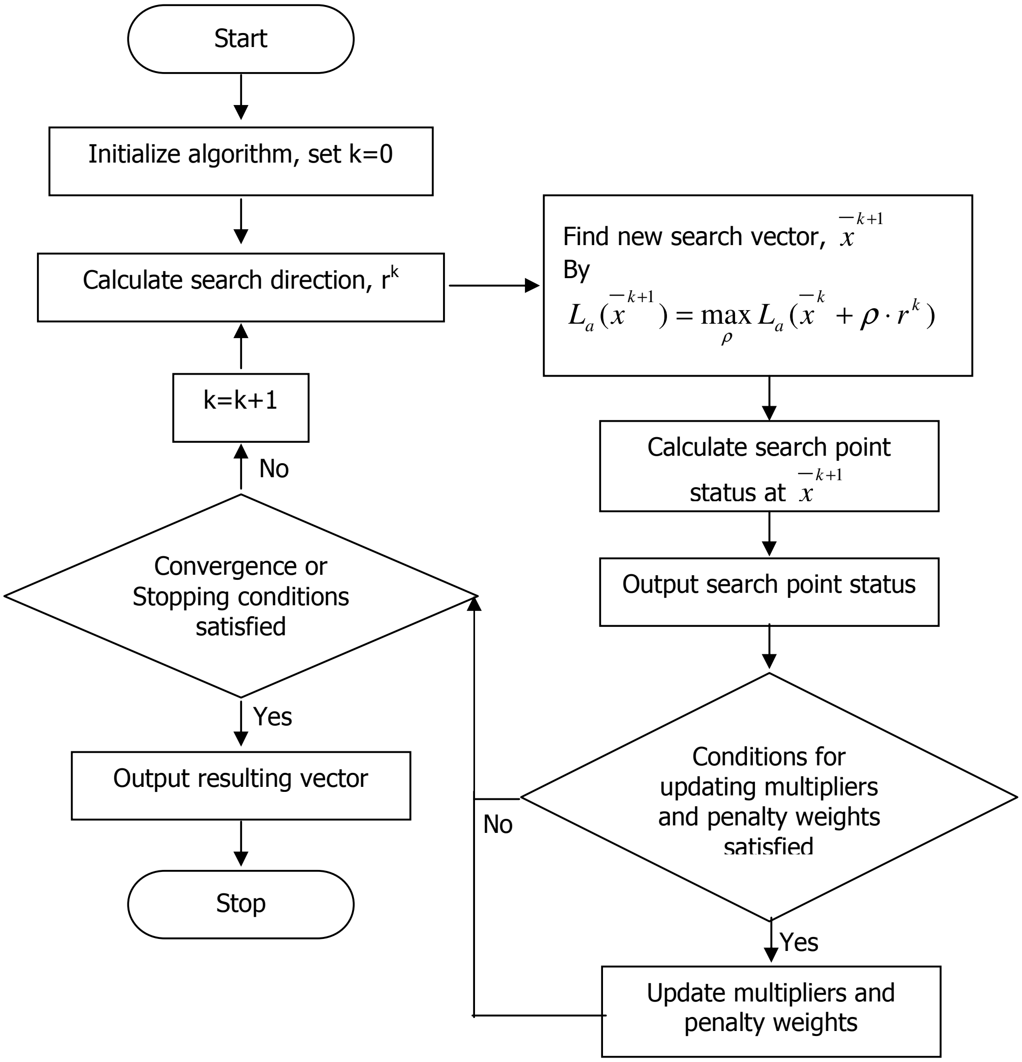

Figure 3–2: General optimization sequence using a multiplier algorithm

3.5 Some Constants Used in the Augmented Lagrangian Algorithm

The values of some of parameters are taken constant during the optimization process. These are listed below with brief explanations [20].

- ε1: Required to test for final convergence, used in conjunction with $\left\|\nabla L_a^k\right\|$. The algorithm stops when: $\left\|\nabla L_a^k\right\| < \varepsilon 1$, where $\left\|\nabla L_a^k\right\|$ is the magnitude of the gradient of augmented function at k^{th} step.
- ε2: Required to determine if a multiplier update is required,
- ε3: Used together with $\Delta x = \left\|x^{k+1} - x^k\right\|$ both in a test to determine if a multiplier update is required and in a test for final convergence, algorithm stops when $\left\|x^{k+1} - x^k\right\| < \varepsilon 3$,
- IBSD: Bad search direction counter,
- IMAX: Number of unidirectional searches allowed,
- NSRCH: A multiplier update is forced when number of searchs in a step reaches NSRCH,
- w1,w2,w3: Initial values of penalty weights,
- γ: Penalty increment factor,
- wf: Maximum allowable value for penalty weighs.
- Integration step size, *h*: Set as 1/2000th of conduction period (See section 3.9.1).
- ε_{TH}: Tolerance for the solution process given in section 3.9.1 to end the process of determining the turn off point, set as equal to the integration step size by default.
- h_{dif}: Numerical differentiation interval, not a constant value, but the 1/100th of each independent optimization parameter (see Appendix B.3).
- B_{t_peak}, The SRM operates at this value of peak flux density.
- NH: Harmonic level used for Fourier series expansions.
- k_w: Coil fill factor, default value is set as 0.7 in the software,the user can change it from the interface. For the test motor, this value is found to be 0.827.

3.6 Independent Optimization parameters

These are the minimum number of independent parameters via which the objective function and performance functions can be computed. In this study, 9 independent parameters are selected. These are dimensional parameters of SRM:

X1:d_u: inner diameter of rotor

X2:d_i: outer diameter of rotor

X3:D_o: outer diameter of stator

X4:L_c:core length

X5:y_b:back core width

X6:t_s: stator pole width

X7:t_r: rotor tooth width

X8:g: airgap length

X9:Advance Angle

$$\bar{x} = \begin{bmatrix} X1 \\ X2 \\ X3 \\ X4 \\ X5 \\ X6 \\ X7 \\ X8 \\ X9 \end{bmatrix}$$

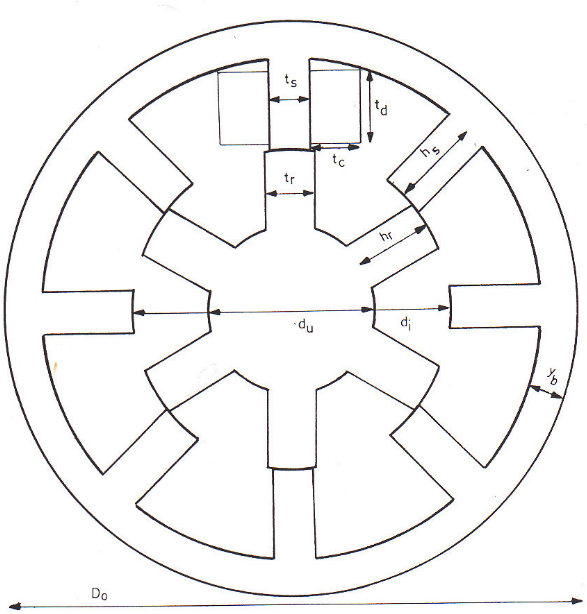

Figure 3–3: Independent physical parameters

3.7 The Object Function: Weight of SRM

In this study, the object function to be minimized is chosen as the total weight of SRM including iron and copper weight. The formulation of the object function is used as given in [21].

3.7.1 Calculation of Iron Weight

In terms of the motor dimensions, total iron weight of a given SR motor can be calculated as follows:

$$W_{fe} = \sigma_{fe}(\pi(D_o - y_b)y_b L_c + N_s t_s h_s L_c + \frac{\pi}{4} d_u{}^2 L_c + N_r t_r h_r L_c) \tag{3–13}$$

where σ_{fe} is density of iron, 7.55 gm/cm^3.

3.7.2 Calculation of Copper Weight

Total copper weight may be expressed in terms of the motor dimensions as given in equation 3.14:

$$W_{cu} = \sigma_{cu} N_s k_w t_c t_d l_{av} \tag{3–14}$$

σ_{cu} is density of copper, 8.88 gm/cm^3.

k_w is winding factor, t_c coil width, t_d coil depth.

l_{av} is the average coil length and

$$l_{av} = 2(t_s + t_c) + 2(L_c + t_c) \tag{3–15}$$

The values, t_c and t_d which are width and height of coil are can be calculated from independent parameters [21], using equations 3.16 ~ 3.18 and Figure 3.4.

From Figure 3.4;

$$c1 = \frac{d_i}{2} + g + a$$

$$c2 = c1 \cdot \tan\left(\frac{\pi}{N_s}\right)$$

$$c3 = \frac{D_o}{2} - y_b$$

$$c4 = c3 \cdot \cos\left(\sin^{-1}\frac{c2}{c3}\right) \tag{3–16}$$

$$t_c = c2 - \frac{t_s}{2} \qquad \textbf{(3–17)}$$

$$t_d = c4 - c1 \qquad \textbf{(3–18)}$$

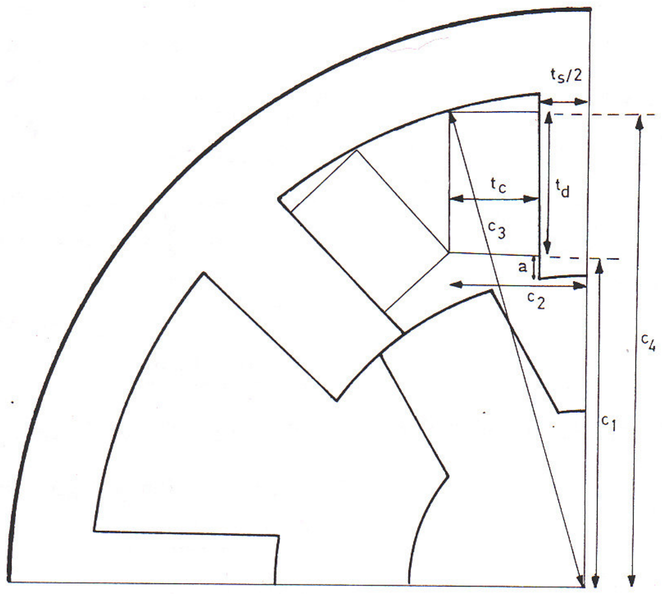

Figure 3–4: Winding arrangement [21]

Using the initial conditions, predetemined parameters, and coil area dimensions, the number of turns, N_t can easily be calculated [21]. With given unity conduction period, the flux density is desired to reach its maximum value. So, N_t can be extracted from the terminal equation of excited coil taking θ_c = 1 p.u., B_t = B_{tpeak}:

$$N_t = \frac{V}{W_r}\frac{\pi}{N_r}\frac{1}{B_{tpeak}t_s L_c} \qquad \textbf{(3–19)}$$

where; V is source voltage, W_r is rotor speed, N_r is number of rotor teeth, B_{tpeak} is the maximum allowable flux density, t_s is stator pole width and L_c is the core length. During the optimization process, at each step, only the t_s and L_c are changed by the algorithm. A "round" function, which rounds the floating point number to nearest integer value, is used for equation 3.19 in the software to avoid non-integer values of N_t. This operation introduces a little error which is negligible, but simplifies the solution process. At low speeds, e.g. 520 rpm, the equation 3.19 gives as large values as 4200 turns. These large values are not logical, so a maximum value of 450 turns is set for N_t for the optimized SRM required for washing machine application This value is determined after several optimization processes.

3.8 Constraints

The result of the optimization process should satisfy some performance criteria. As well as these performance functions, manufacturing difficulties also add some constraints to final design.

3.8.1 Equality Constraint

The average torque produced by SRM at given speed is set as the only equality constraint.

- For SRWash [25]:
    - At 520 rpm: T_{av} = 1.7 N.m.
- For SRSpin [25]:
    - At 12000 rpm: T_{av} = 0.35 N.m.

The average torque is required to specify the output power rating of the motor

3.8.2 Inequality Constraints

3.8.2.1 Air Gap Length

Due to manufacturing difficulties, a lower limit for air gap is set as 0.25 mm, and in order not to reduce performance of the SRM, an upper limit for air gap is set as 0.5 mm.

$$0.25mm \le g \le 0.5mm \tag{3–20}$$

$$0.25 \le X[8] \le 0.5 \tag{3–21}$$

Actually, Equation 3.21 does not define a constraint function, but a bounded variable which is both bounded from above and below.

It is important to note that, maximum performance occurs at the minimum value of air gap length, and due to the nature of performance calculation methods, the optimization process forces air gap length to reach its minimum. Because of this, value of 0.25 mm is used for the initial designs in order to reduce the number of iterations.

3.8.2.2 Inner Diameter of the Rotor

A lower limit for inner diameter of rotor is set in order to avoid very small values which can not support loads.

$$d_i \ge 20mm \tag{3–22}$$

This constraint is applied as follows:

$$\frac{X[1]}{20} - 1 \ge 0 \tag{3–23}$$

3.8.2.3 Rotor Tooth Depth

Referring to section 2.4, the permeance data used in the prediction of flux linkage characteristics of the SRM is obtained for tooth depth equal to 40 times air gap length. However, the results for the test motor (See section 4.3) show that, predictions are accurate enough for rotor tooth depth of approximately 22 times air gap length.

$$h_r = \frac{d_i - d_u}{2} \tag{3–24}$$

$$h_r \ge 22 \cdot g \tag{3–25}$$

This constraint is applied as follows:

$$\frac{X[2]-X[1]}{44\cdot X[8]}-1\geq 0 \qquad \textbf{(3–26)}$$

3.8.2.4 Stator pole Depth

The reason given in section 2.4 is also valid for determining the stator pole depth. However, h_s should be larger in order to permit a larger coil area. Otherwise, the current density value goes higher values. So, for low speed optimization process, in which, greater number of turns is required, 80 times airgap length is set as constraint for h_s, for high speed optimization process, number of turns requirement halves, so 40 times airgap length is set as constraint for h_s at high speed.

$$h_s=\frac{D_O-2y_b-2g-d_i}{2} \qquad \textbf{(3–27)}$$

For SRWash (520 rpm):

$$h_s\geq 80g \qquad \textbf{(3–28)}$$

This constraint is applied as follows:

$$\frac{X[3]-2X[5]-2X[8]-X[2]}{160X[8]}-1\geq 0 \qquad \textbf{(3–29)}$$

For SRSpin (12000 rpm):

$$h_s\geq 40g \qquad \textbf{(3–30)}$$

This constraint is applied as follows:

$$\frac{X[3]-2X[5]-2X[8]-X[2]}{80X[8]}-1\geq 0 \qquad \textbf{(3–31)}$$

3.8.2.5 Efficiency

As well as the torque constraint, the resultant SRM should satisfy an efficiency requirement. Especially for the washing machine application, the SRM is compared with similar rating induction motor. So, an efficiency of 80% is set for low speed application, and 35% is set for high speed application [25].
For SRWash (520 rpm):

$$eff \geq 80\% \qquad \textbf{(3–32)}$$

This constraint is applied as follows:

$$\frac{eff}{80} - 1 \geq 0 \qquad \textbf{(3–33)}$$

For SRSpin (12000 rpm):

$$eff \geq 35\% \qquad \textbf{(3–34)}$$

This constraint is applied as follows:

$$\frac{eff}{35} - 1 \geq 0 \qquad \textbf{(3–35)}$$

3.8.2.6 Advance Angle

Advance Angle is set as an independent optimization parameter in this study, since it has significant effect on produced average torque, as described in Chapter 2. A lower limit is set as the point where positive torque region of static torque curves of an SRM starts. An upper limit is set as the point where the positive torque region of prior phase begins. For an 8-6 SRM, referring to Figure 2.5:

$$7.5^0 \leq AA \leq 22.5^0 \qquad \textbf{(3–36)}$$

$$7.5 \leq X[9] \leq 22.5 \qquad \textbf{(3–37)}$$

This configuration of upper and lower bounds of advance angle permits two phase on excitation with unity conduction period. This operating scheme enhances the efficiency of the motor and permits reaching larger torque values.

3.8.2.7 Current Density

An upper limit for rms value of current density, J_c is set in order to compare the resultant motor with similar rating induction motors.

$$J_C = \frac{I_{RMS}}{t_C \cdot t_d \cdot k_w} \qquad \textbf{(3–38)}$$

$$J_c \leq 6.5 \text{ A/mm}^2 \qquad \textbf{(3–39)}$$

This constraint is applied as follows:

$$1 - \frac{J_c}{6.5} \geq 0 \qquad \textbf{(3–40)}$$

Where, t_C and t_d are coil area dimensions as shown in section 3.6.2, and k_w is winding factor which is chosen as 0.7 depending on experimental experience.

3.8.2.8 Stator and Rotor Tooth Width

Referring to section 2.5and the normalized permeance data available, in normalized form, initially the following constraints may be set:

$$0.3 \leq t_{sn} \leq 0.5 \qquad \textbf{(3–41)}$$

And

$$0.3 \leq t_{rn} \leq 0.5 \qquad \textbf{(3–42)}$$

In [22], an SRM optimization study is done which aims to reach a motor geometry with minimum torque ripple. Table 3.1 summarized the results of [22].

Table 3-1 Optimum variables for different MMF levels for UDSS

MMF (kA)	λ/g	ts/λ	tr/λ
30	165	0.49	0.5
40	202	0.49	0.5
50	227	0.41	0.5
60	226	0.4	0.5
70	225	0.43	0.5

It can be observed from the Table 3.1 that the ripple is smaller for λ/g >165, ts/λ > 0.43, and tr/λ= 0.5. Torque ripple is not a constraint for this study; however, it is desired to obtain an optimum SRM geometry, which also satisfies lower ripple requirement on produced torque. In view of the results of [22], these lower limits are changed to 0.4. These constraints are applied as follows:

$$0.4 \le t_{sn} \le 0.5 \tag{3–43}$$

$$\frac{t_{sn}}{0.4} - 1 \ge 0 \tag{3–44}$$

$$1 - \frac{t_{sn}}{0.5} \ge 0 \tag{3–45}$$

And

$$0.4 \le t_{rn} \le 0.5 \tag{3–46}$$

$$\frac{t_{rn}}{0.4} - 1 \ge 0 \tag{3–47}$$

$$1 - \frac{t_{rn}}{0.5} \ge 0 \tag{3–48}$$

3.8.2.9 Constraints on Normalized parameter λ/g

Referring to section 2.5, in normalized form, the following constraints may be set:

$$40 \le \frac{\lambda}{g} \le 250 \tag{3–49}$$

To obtain lower torque ripple, Şahin [22] suggests a λ/g value greater than 165 as shown in Table 3.1. However, this large value of λ/g magnifies the weight of the motor. Since the primary aim of optimization part this study is to reach minimum weight, the lower limit of λ/g is set as 70.

$$70 \le \frac{\lambda}{g} \le 250 \tag{3–50}$$

$$\lambda = \frac{\pi \cdot X[2]}{NRT} \tag{3–51}$$

Where *NRT* is the number of rotor teeth. These constraint is applied as follows:

$$\frac{\lambda / X[8]}{70} - 1 \ge 0 \tag{3–52}$$

$$1 - \frac{\lambda / X[8]}{250} \ge 0 \tag{3–53}$$

3.9 Calculation of Performance Functions within Optimization Algorithm

During each optimization step, the performance functions "Average Torque", "Efficiency", and "RMS value of current density" are needed to be calculated. The performance calculation methods used in optimization process are same as the methods given in Chapter 2. There are only some modifications which speed up the process, and satisfy 1 p.u. conduction period. Also, differentiation operation is needed frequently in the algorithm. Analytical differentiation is not applicable to this study, since the performance calculations are not parametrical functions of optimization parameters. So a numerical differentiation method is needed. The formulation and the application of numerical differentiation are given in Appendix B.

3.9.1 Obtaining Required Conduction Period

In Chapter 2, it is stated that, the "switch on" and "switch off" positions for the phase under excitation are required for performance calculations. After the switch off, the input voltage reverses its polarity, and the current decreases to zero in a time which is not known until it drops to zero. The total period in which the phase carries currents is the conduction period.

This conduction period as set as 1 p.u. in the study, as an alternative, this option is arranged as user selectable from the interface of the software. To guarantee 1 p.u. conduction period, a simple technique is used. Two solutions are started at the same time, one is from "Switch On" position, and the other is from "Switch On + 1 p.u." position. The two solutions meet at one point and the solution algorithm stop calculation after joining two solutions into one. Figure 3.5 describes this process graphically.

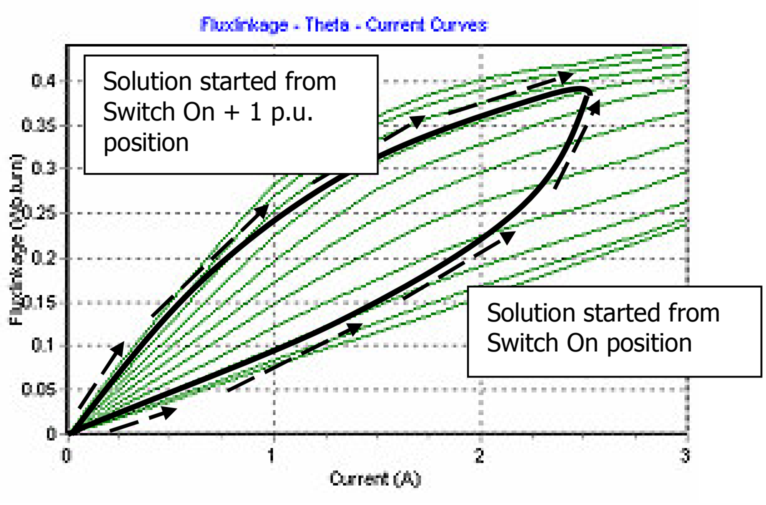

Figure 3–5: Graphical view of solution process with forced $\theta_c = 1$ p.u.

Starting the solution from "X_{ON} (Switch_{ON})"; initial position $X = X_{ON}$, $I_i = 0$, $\lambda_i = 0$, $V = V_{in}$, at each solution step: $X = X+h$

Starting the solution from "$X_{ON} + \theta_c$"; initial position $X = X_{ON} + \theta_c$, $I_i = 0$, $\lambda_i = 0$, $V = -V_{in}$, at each solution step: $X = X-h$, this solution stops when it reaches I_{max} (if chopping occurs) or when it meets other solution. The position it stops is recorded as the X_{off} position.

"*h*" is the integration step size. This step size is set as:

$$h = \Delta\theta = {}^{\theta_C}\!/_{2000} \tag{3–54}$$

The value of *h* set for the optimization process is approximately two times grater than the one set for analysis part of the software. This relatively larger value of integration step size decreases the accuracy in a negligible amount, however, speeds up the performance calculations twice. The two solutions meet at one point with an error of ε_{TH}, which can be set by the user and needs to be smaller of equal to integration step size. The process stops when:

$$\left|\theta_{ON} - \theta_{OFF}\right| \le \varepsilon_{TH} \tag{3–55}$$

After the process, the Flux linkage – Current locus is constructed, as given in Figure 3.5. The occurrence of chopping action is naturally included in the solution process.

3.9.2 Determination of the Current Limit

The solution process given in section 2.2 requires a current limit value. Especially at lower speeds, chopping action occurs at this current limit. During the optimization process, for each generated search point, and hence the motor geometry, a current limit should be determined. In this study, the approach similar to the one proposed in [21] is used. In this approach, the current value, which satisfies the maximum possible peak flux density value in the IN position of a given structure, is set as current limit. This procedure is done after predicting the flux linkage curves of current search vector as shown in Figure 2.6. This method guarantees the SRM to operate at its maximum possible flux density value, if the current reaches its maximum value.

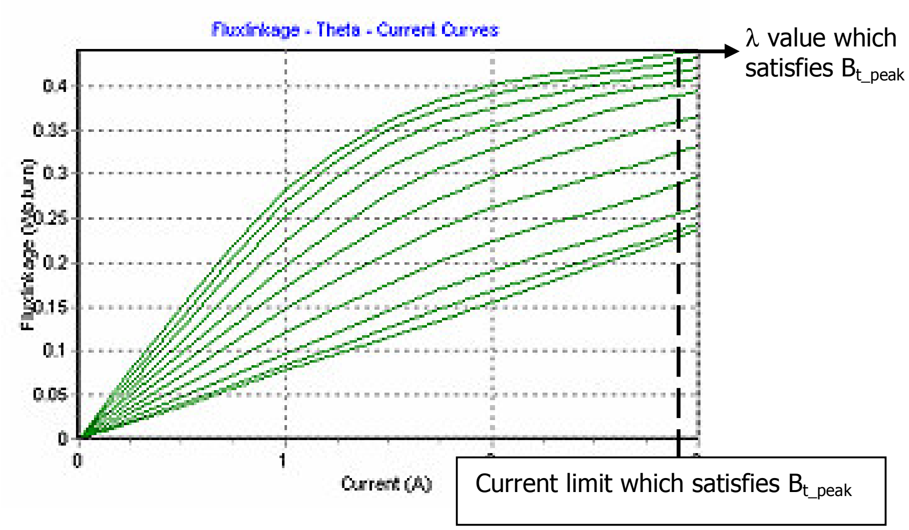

λ value which satisfies B_{t_peak}

Current limit which satisfies B_{t_peak}

Figure 3–6: Determination of current limit

3.9.3 Calculation of Current Density

After the solution process, as described in section 2.3.1, rms value of phase current is calculated. Also, as described in section 3.6.2, effective coil area is calculated as:

$$A_C = t_c \cdot t_d \cdot k_w \qquad \textbf{(3–56)}$$

So the rms value of current density is:

$$J_c = \frac{I_{RMS}}{A_C} \qquad \textbf{(3–57)}$$

The value of k_w can be set by the user using the interface of the software. In this study, SR2, the value 0.7 is used.

3.9.4 Calculation of Efficiency

By definition, efficiency is the ratio of output power to input power.

$$\eta = \frac{P_{OUT}}{P_{IN}} \% \qquad \textbf{(3–58)}$$

The output power at a given speed is calculated as:

$$P_{OUT} = T_{AV} \cdot W_r \qquad \textbf{(3–59)}$$

Input power can be calculated as the sum of output power with total losses:

$$P_{IN} = P_{OUT} + P_{Core} + P_{Cu} \qquad \textbf{(3–60)}$$

Losses are calculated as described in section 2.3.

3.10 Conclusion

In this chapter, the mathematical background of the Augmented Lagrangian method, which is the selected optimization algorithm for this study, is explained briefly. After giving the general form of constraint optimization scheme, the definition of Augmented Lagrangian function is given with the describtions of multipliers and penalty weights. After explaining the multiplier and weight update rules, the search method, DFP is given. This search method is known to be one of the best of Quasi-Newton methods, which requires only the first derivatives. The independent optimization parameters are determined and objective function is formed using these parameters. The constraint functions are determined from the performance requirements of the motor, and physical constraints. The methods for performance calculations are given briefly.

The application details of the optimization method to the design optimization of an SRM is given in Chapter 4.

CHAPTER 4

RESULTS

4.1 Introduction

In Chapter 2, the performance analysis methods are stated using the non-linear flux linkage characteristics of SRM. Prediction of these characteristics is also given in Chapter 2. In the first part of this chapter, the verification of the methods given in Chapter 2 will be investigated.

In Chapter 3, the mathematical background of optimization problem and its adaptation to SRM weight optimization are given. In the second part of this chapter, the results of optimizations carried on SRMs will be given

4.2 Verification of Performance Calculation Methods

The performance calculation methods given in Chapter 2 are programmed using Borland Delphi compiler which is an advanced version of Object Pascal programming language[46]. The analysis part of the software takes flux linkage data as input. Other inputs are operating conditions, such as the rotor speed, advance angle, excitation period, current limit, and loss curves. This part of the software is used to verify proposed calculation method by comparing results with measurements, which are taken from [26].

4.2.1 The Test Motor

The SRM which belongs to METU EE Electrical Machinery Department is chosen as the test motor. The name of the motor is SR2.

Specifications of SR2:

Rated power : 750Watt
Rated speed : 10.000 rpm
Operating Voltage : 300Volt DC
Rated Current : 3Ampere/pole
Number of phases : 4 (8 Stator poles)
Number of rotor teeth : 6

Table 4-1: Measured Physical dimensions of SR2

Rotor outer diameter	38.6 mm
Stator outer length (thicker part)	120.4 mm
Stator outer length (thinner part)	111.4 mm
Stator core inner diameter	99.99 mm
Stator pole tip width	8.35 mm
Tapering angle	2.2 degree
Rotor tooth width	8.4 mm
Airgap length	0.325 mm
Rotor tooth depth	7.2 mm
Stator pole depth	34.37 mm
Shaft diameter	16.5 mm
Core length	41 mm

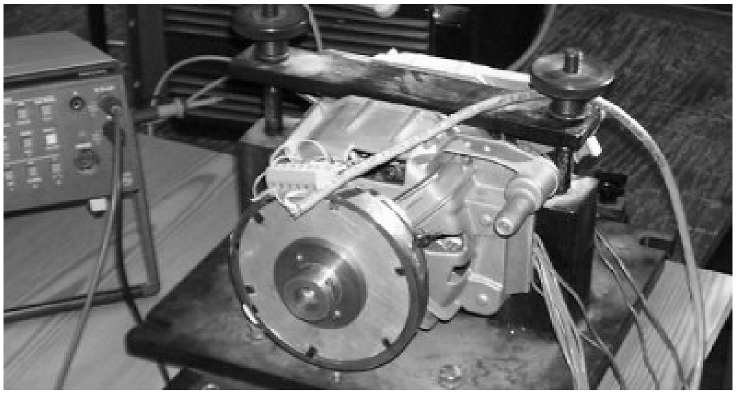

Figure 4-1: The photograph of SR2

4.2.2 Measured Flux Linkage Data

The "Flux linkage – Position – Current", and "Torque – Position – Current" data are obtained by M.Özgür KIZILKAYA and E.Bizkevelci [26]. Graphical and tabular representations of the data are given below.

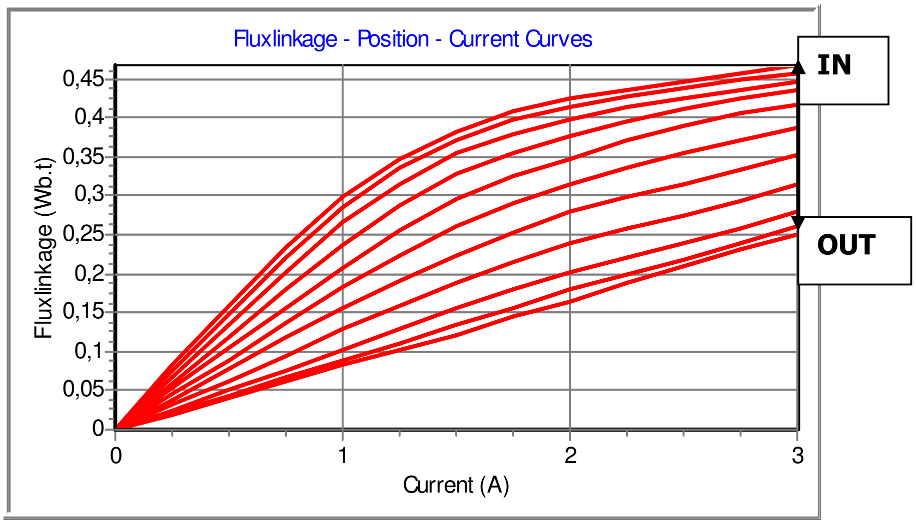

Figure 4-2: Graphical represantation of measured flux linkage data

Table 4-2: Tabular view of measured flux linkage data

CURRENT	FLUX LINKAGE (Wb)										
	0°	**3°**	**6°**	**9°**	**12°**	**15°**	**18°**	**21°**	**24°**	**27°**	**30°**
0 A	0.000	0.000	0.000	0.000	0.000	0.000	0.000	0.000	0.000	0.000	0.000
0.25 A	0.083	0.075	0.067	0.060	0.053	0.045	0.038	0.031	0.025	0.022	0.020
0.50 A	0.160	0.148	0.134	0.119	0.105	0.090	0.077	0.063	0.051	0.043	0.040
0.75 A	0.234	0.221	0.203	0.181	0.157	0.137	0.118	0.095	0.076	0.066	0.061
1 A	0.299	0.286	0.267	0.238	0.208	0.182	0.157	0.128	0.102	0.088	0.083
1.25 A	0.347	0.335	0.316	0.287	0.255	0.223	0.192	0.158	0.129	0.111	0.103
1.50 A	0.383	0.372	0.354	0.327	0.296	0.260	0.224	0.187	0.155	0.134	0.122
1.75 A	0.408	0.397	0.380	0.355	0.325	0.290	0.253	0.214	0.180	0.157	0.144
2 A	0.425	0.414	0.398	0.376	0.348	0.315	0.279	0.239	0.202	0.179	0.165
2.25 A	0.437	0.427	0.413	0.395	0.371	0.337	0.298	0.257	0.221	0.199	0.187
2.50 A	0.446	0.438	0.425	0.411	0.390	0.355	0.315	0.274	0.239	0.218	0.209
2.75 A	0.457	0.448	0.437	0.424	0.406	0.372	0.334	0.294	0.259	0.239	0.230
3 A	0.468	0.458	0.446	0.435	0.417	0.388	0.353	0.314	0.280	0.260	0.251

4.2.3 Performance Calculations and Comparisons with Measured Performance

Using the method described in Section 2.2, the performance of the motor is predicted first using the measured flux linkage curves. The calculations include; Current – Time waveforms for various rotor speeds, Torque – Speed curves for four distinct Advance Angles (AA = 0^0 – 4^0 – 7.5^0 – 11^0), and Loss – Speed curve for 0^0 advance angle.

Measurement conditions:

DC link voltage : 300 Volt
Chopper settings : 2.85 – 3.15 Ampere
Switching mode : One phase on
Excitation period : $\Delta\theta = 15^0$ (0.5 p.u.)

Initial Conditions:

$V = V_{in} = 300$ V
$i = 0$ A

θ_{ON} = Switch on position of SRM phase (Depends on Advance Angle) as shown in Figure 2.5.

$\theta_{OFF} = \theta_{ON} + \Delta\theta$, switch off position of SRM phase.

4.2.3.1 Comparison of Phase current waveforms

The predicted performance is compared with measurements. The comparison of "Rise Times", "Fall Times", "Peak Values" and "Number of Chops" of predicted and measured current waveforms for different Advance Angles and speeds are given in Table 4.3 and in graphical form below.

Table 4-3: The comparison of Rise Times and Fall Times of predicted and measured current waveforms

Speed (rpm)	**Advance Angle**	**Rise Time (Measured – Predicted)**	**Fall Time (Measured – Predicted)**	**Peak Values**	**Number of Chops**
1000	**0**	1.36 ms – 1.345 ms	1.36 ms – 1.355 ms	3.15 – 3.15	5 – 5
1600	**0**	1.47 ms – 1.48 ms	1.44 ms – 1.40 ms	3.15 – 3.15	1 – 1
1000	**11**	0.9 ms – 0.85 ms	1.1 ms – 1.0 ms	3.15 – 3.15	5 – 5
2000	**4**	1.16 ms – 1.16 ms	1.09 ms – 1.13 ms	1.85 – 1.84	0 – 0

Comparison of current waveforms at 1000 rpm, Advance Angle = 0°:

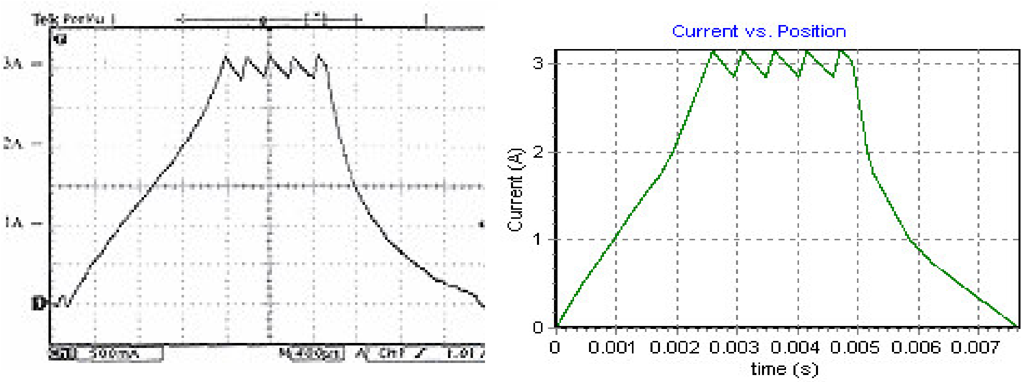

Figure 4-3: a) Measured current waveform at 1000 rpm, AA=0 degree **b)P**redicted current waveform at 1000 rpm, AA=0 degree

Comparison of current waveforms at 1600 rpm, Advance Angle = 0°:

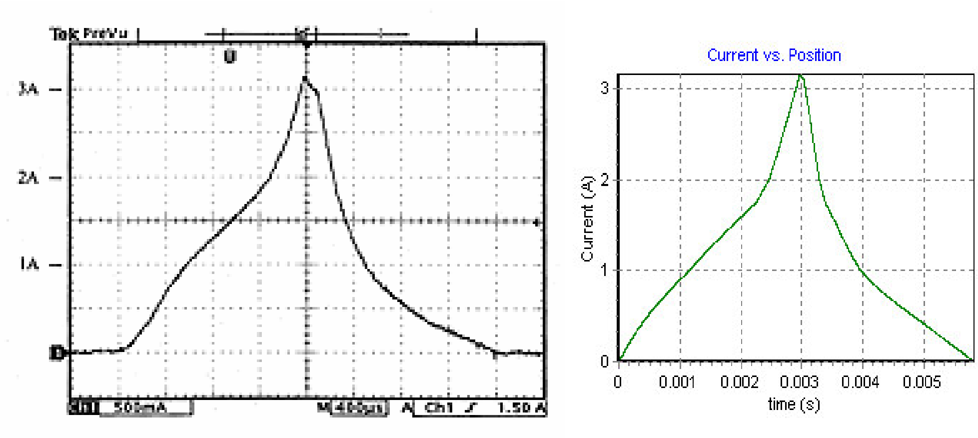

Figure 4-4: a) Measured current waveform at 1600 rpm, AA=0 degree **b)**Predicted current waveform at 1600 rpm, AA=0 degree

Comparison of current waveforms at 2000 rpm, Advance Angle = 4°:

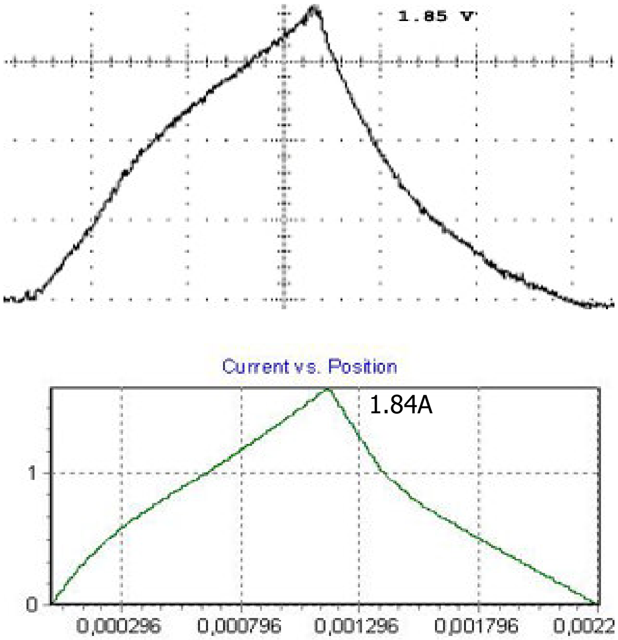

Figure 4-5: a) Measured current waveform at 2000 rpm, AA=4 degree **b)**Predicted current waveform at 2000 rpm, AA=4, degree

Comparison of current waveforms at 1000 rpm, Advance Angle = 11°:

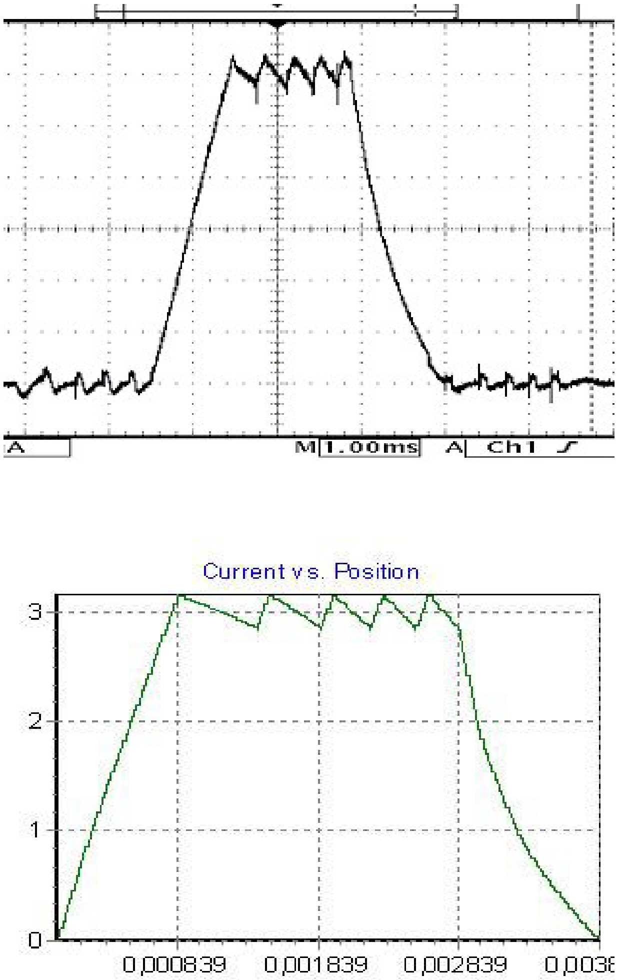

Figure 4-6: a) Measured current waveform at 1000 rpm, AA=11 degree
b)Predicted current waveform at 1000 rpm, AA=11, degree

After examining Table 4.3, and Figures 4.3. to 4.6, it can be conluded that, the solution method given in section 2.2 satisfies good results. The shape of predicted and measred current waveforms are very similiar. The characteristic properties of current waveforms are very close to each other. In the next section, the Torque – Speed curves obtained using the solution method will be compared with measured curves.

4.2.3.2 Comparison of Torque – Speed Characteristics

The comparison of predicted and measured Torque – Speed curves are given below graphically and numerical values including the percentage errors are given in Table 4.4.

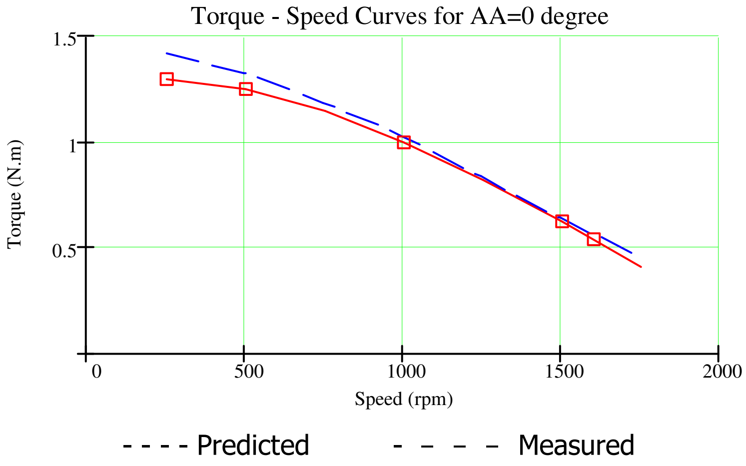

Figure 4-7: Torque – Speed curves, AA = 0^0

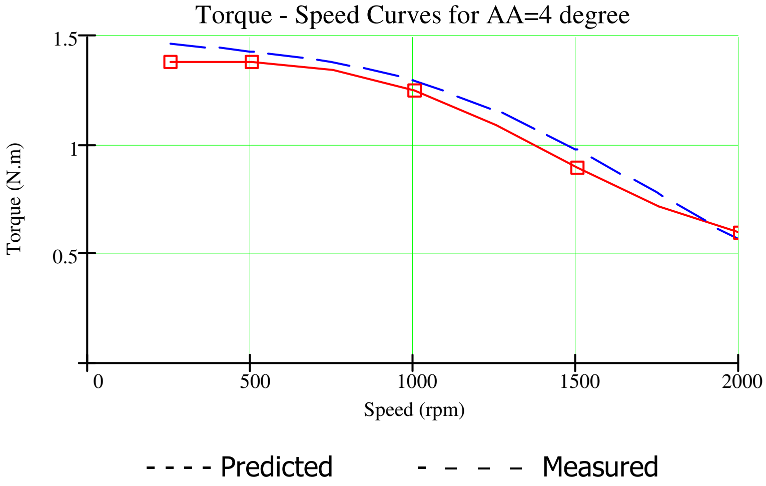

Figure 4-8: Torque – Speed curves, AA = 4^0

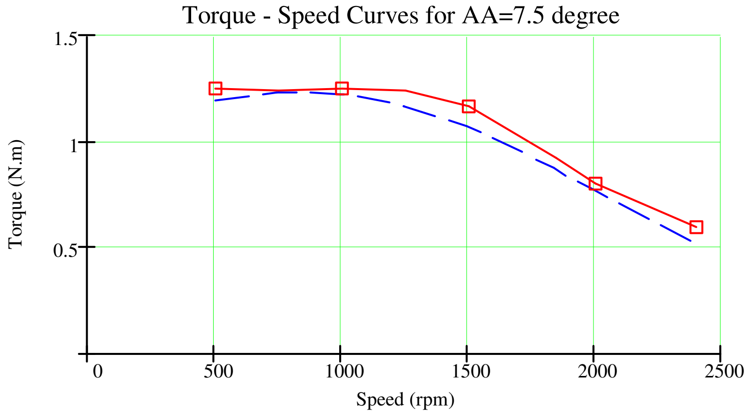

- - - - Predicted   - – – – Measured

Figure 4-9: Torque – Speed curves, AA = 7.5^0

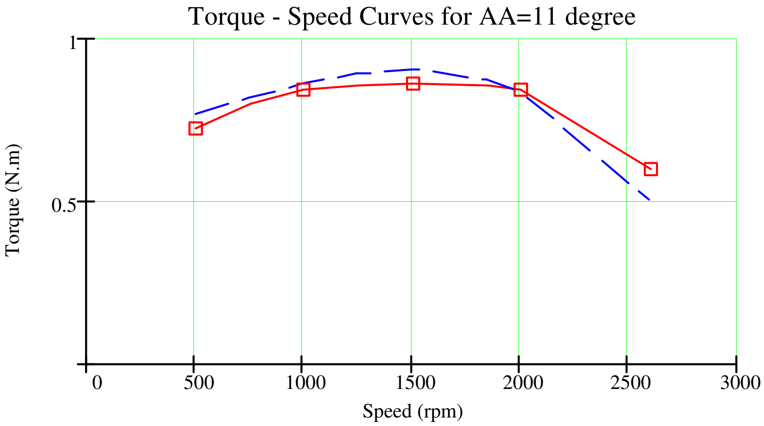

- - - - Predicted   - – – – Measured

Figure 4-10: Torque – Speed curves, AA = 11^0

Table 4-4: The percentage errors between predicted and measured torques

AA = 0^0				AA = 4^0			
rpm	**Measured**	**Predicted**	**%err**	**rpm**	**Measured**	**Predicted**	**%err**
250	1.300	1.423	-9.46%	**250**	1.380	1.465	-6.16%
500	1.250	1.323	-5.84%	**500**	1.380	1.430	-3.62%
1000	1.000	1.025	-2.50%	**1000**	1.250	1.300	-4.00%
1500	0.625	0.632	-1.12%	**1500**	0.900	0.980	-8.89%
1600	0.540	0.558	-3.33%	**2000**	0.600	0.561	6.50%
AA = 7.5^0				AA = 11^0			
rpm	**Measured**	**Predicted**	**%err**	**rpm**	**Measured**	**Predicted**	**%err**
500	1.250	1.200	4.00%	**500**	0.720	0.764	-6.11%
1000	1.255	1.220	2.79%	**1000**	0.840	0.858	-2.14%
1500	1.170	1.070	8.55%	**1500**	0.860	0.901	-4.77%
2000	0.800	0.762	4.75%	**2000**	0.840	0.836	0.48%
2400	0.600	0.514	14.33%	**2600**	0.600	0.498	17.00%

4.2.3.3 Comparison of SRM Core Losses for SR2

Predicted and measured losses for SR2 are given in Table 4.5 with the percentage error between them. Measured values are taken from [45], which are obtained for advance angle of 0 degree, excitation period of 0.5 p.u., and current limit of 3A.

Table 4-5: Comparison of losses for SR2

AA = 0^0			
rpm	**Measured**	**Predicted**	**%err**
500	51	37	27.45%
1250	60	67	-11.67%
1500	60	70	-16.00%

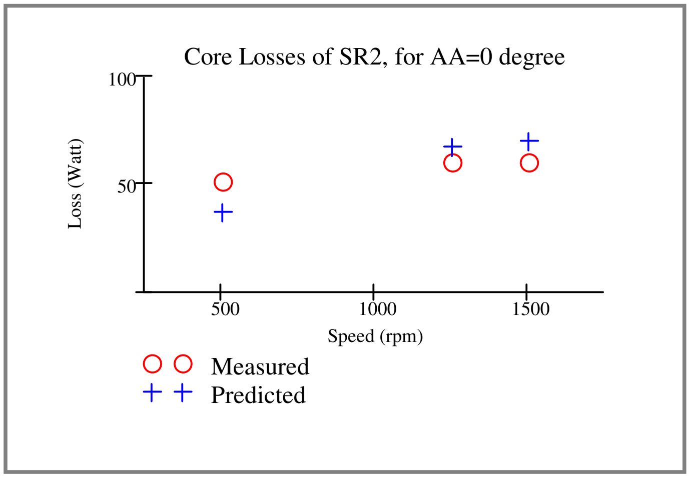

Figure 4-11: Measured and Predicted Core losses for SR2

From Table 4.5 and Figure 4.11, maximum error occurs at 500 rpm, with an percentage error of 27.45%. However, the shape of the predicted loss curve is similar to the measured loss curve. Loss predictions include very complex calculation methods (See section 2.3). Furthermore, the available W/kg vs frequency curve is available for a very limited range and is not the curve of the material used for producing SR2.

Table 4.6 shows the fundamental and harmonic frequencies used to calculate core losses at the 3 speed values considered here. It can be noticed that the harmonics considered in core loss calculation reach up to 3000 H, whereas the available data are only up to 200 Hz. Figure 4.12 presents the general shape of the extrapolated loss curves used for the core loss calculations here. It must be also remembered that the Bt values at high frequencies are very very small, while the data are available only down to 0.2 Tesla. To determine the loss at a given B value from the available data, cubic spline interpolation is used.

Table 4-6: Fundamental and 20th harmonic frequencies at given speeds

rpm	**Fund. Frequency**	**20th Harmonic frequency**
500	50	1000
1250	125	2500
1500	150	3000

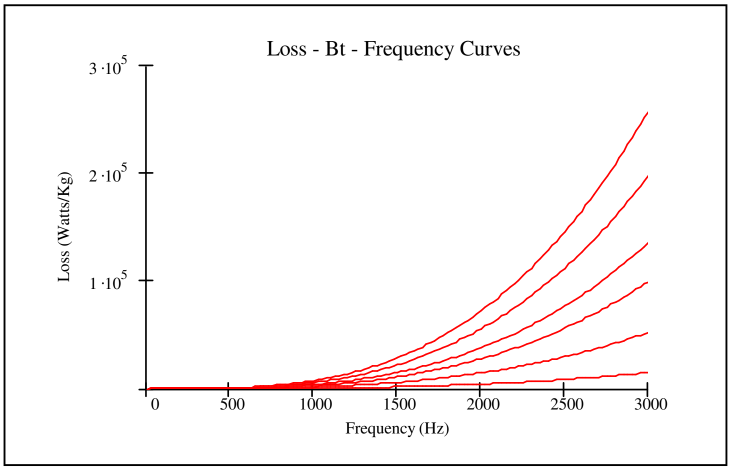

Figure 4-12: Extrapolated loss curves up to 3000 Hz

Due to the nature of cubic spline interpolation, extrapolated curves are in exponential form. However, extrapolation introduces a large amount of error.

4.3 Verification of Prediction of Flux Linkage Characteristics of an SRM

The Flux linkage – Position – Current ($\Psi - \theta - I$)characteristiscs of SR2 are predicted with and without End – Leakage Flux correction. The results are given below both in graphical and tabular form. The percentage errors between the measured and predicted curves are also given in tabular form. Lastly, the Torque – Speed curves obtained using the predicted $\Psi - \theta - I$ curves are compared with the measured Torque – Speed curves.

4.3.1 Predicted Flux Linkage Curves Without End Leakage Correction

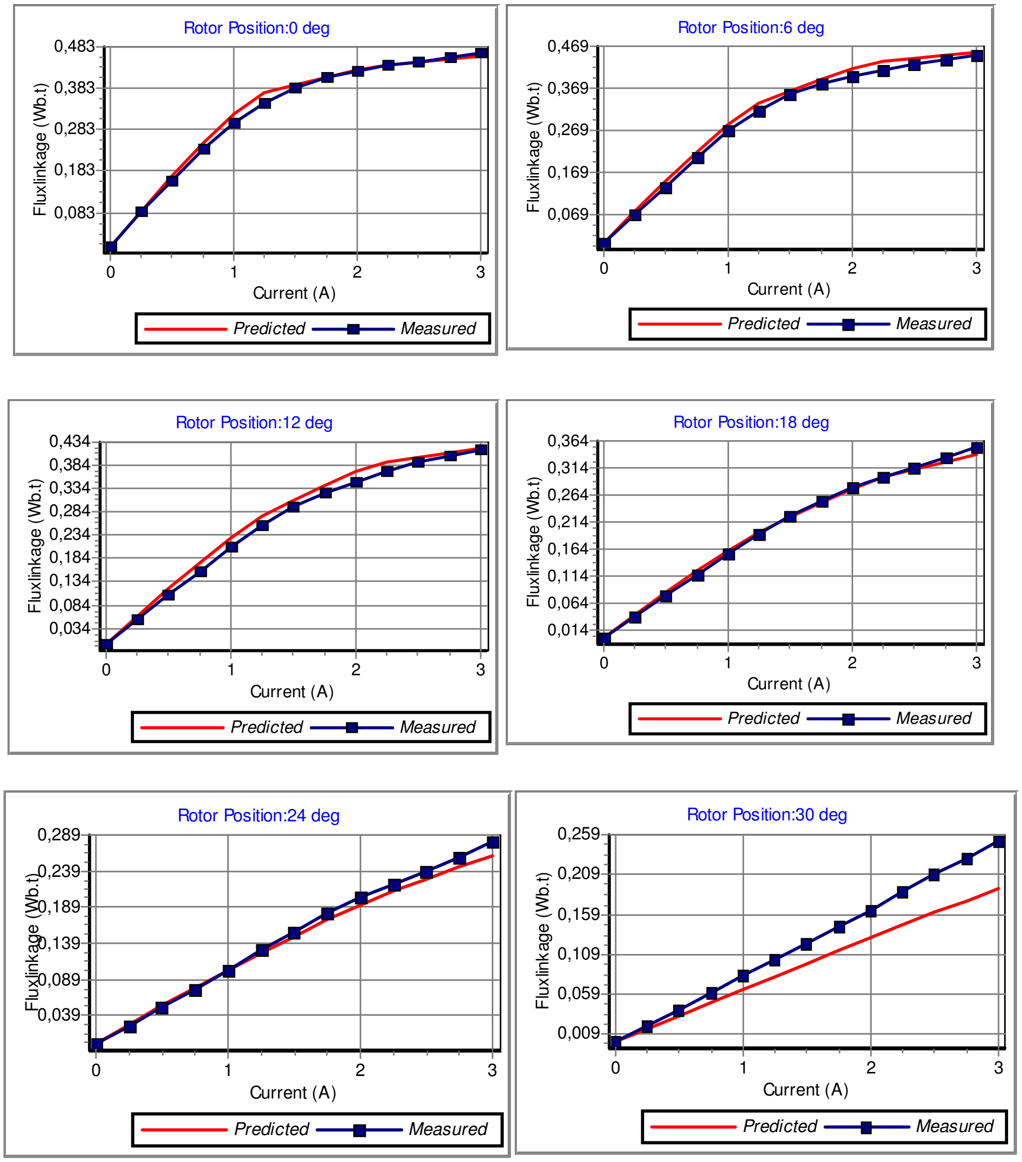

Figure 4-13: Comparison of Measures curves and Predicted curves <u>without end leakage correction</u>

Figure 4.12 shows that, prediction of flux linkage curves are close to measured curves near IN position of the rotor; however, examining the curves near

OUT position, a need for correction apparently arises. In the next section, predicted curves with the end leakage correction are given

4.3.2 Predicted Flux Linkage Curves With End leakage Correction

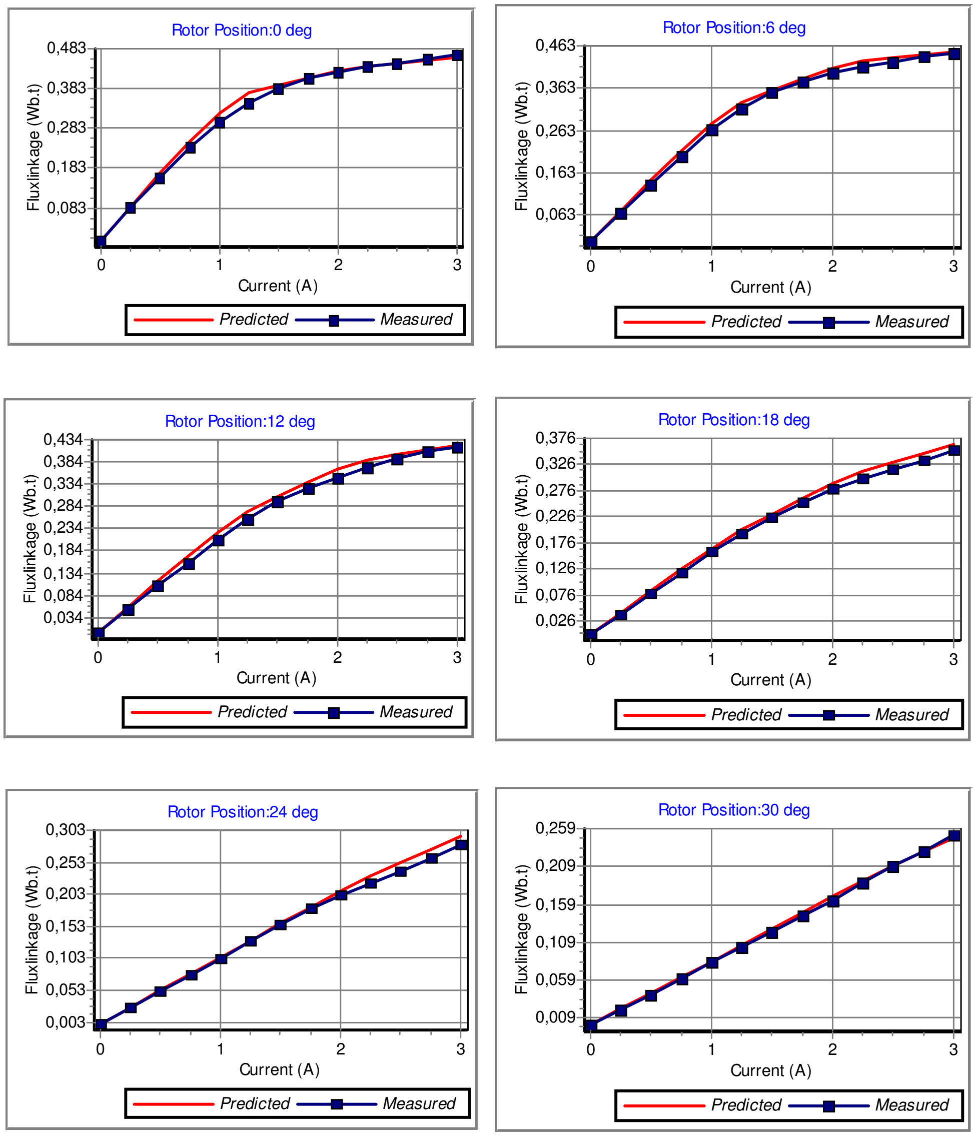

Figure 4-14: Comparison of Measures curves and Predicted curves <u>with end leakage correction</u>

Table 4-7: Numerical values and %errors between measured curves and predicted curves with end leakage correction

Flux linkage (Wb.t)									
	0 degree			***6 degree***			***12 degree***		
I	***Meas.***	***Pred.***	***% err***	***Meas.***	***Pred.***	***% err***	***Meas.***	***Pred.***	***% err***
0	0	0	**0**	0	0	**0**	0	0	**0**
0,25	0.083	0.0840	**1.202**	0.067	0.0723	**7.845**	0.053	0.0579	**9.166**
0,5	0.160	0.1680	**5.001**	0.134	0.1446	**7.912**	0.105	0.1159	**10.387**
0,75	0.234	0.2501	**6.893**	0.203	0.2152	**6.002**	0.157	0.1730	**10.216**
1	0.299	0.3224	**7.816**	0.267	0.2787	**4.368**	0.208	0.2262	**8.748**
1,25	0.347	0.3724	**7.331**	0.316	0.3274	**3.592**	0.255	0.2710	**6.275**
1,5	0.383	0.3912	**2.146**	0.354	0.3562	**0.617**	0.296	0.3046	**2.910**
1,75	0.408	0.4100	**0.490**	0.380	0.3851	**1.330**	0.325	0.3383	**4.103**
2	0.425	0.4266	**0.366**	0.398	0.4099	**2.989**	0.348	0.3678	**5.681**
2,25	0.437	0.4388	**0.422**	0.413	0.4270	**3.381**	0.371	0.3888	**4.810**
2,5	0.446	0.4458	**0.040**	0.425	0.4343	**2.199**	0.390	0.3995	**2.427**
2,75	0.457	0.4528	**0.920**	0.437	0.4417	**1.084**	0.406	0.4101	**1.015**
3	0.468	0.4598	**1.758**	0.446	0.4491	**0.703**	0.417	0.4208	**0.912**
	18 degree			***24 degree***			***30 degree***		
I	***Meas.***	***Pred.***	***% err***	***Meas.***	***Pred.***	***% err***	***Meas.***	***Pred.***	***% err***
0	0	0	**0**	0	0	**0**	0	0	**0**
0,25	0.038	0.0414	**8.912**	0.025	0.0258	**3.194**	0.020	0.0211	**5.739**
0,5	0.077	0.0835	**8.377**	0.051	0.0522	**2.440**	0.040	0.0423	**5.739**
0,75	0.118	0.1250	**5.969**	0.076	0.0788	**3.662**	0.061	0.0632	**3.603**
1	0.157	0.1644	**4.736**	0.102	0.1050	**2.960**	0.083	0.0839	**1.123**
1,25	0.192	0.1996	**3.950**	0.129	0.1308	**1.358**	0.103	0.1048	**1.790**
1,5	0.224	0.2297	**2.566**	0.155	0.1564	**0.872**	0.122	0.1265	**3.671**
1,75	0.253	0.2604	**2.910**	0.180	0.1825	**1.400**	0.144	0.1481	**2.857**
2	0.279	0.2887	**3.476**	0.202	0.2079	**2.926**	0.165	0.1693	**2.622**
2,25	0.298	0.3122	**4.754**	0.221	0.2312	**4.626**	0.187	0.1897	**1.456**
2,5	0.315	0.3294	**4.558**	0.239	0.2517	**5.325**	0.209	0.2091	**0.051**
2,75	0.33357	0.33419	**3.824**	0.25897	0.25854	**5.264**	0.23001	0.22766	**0.656**
3	0.3532	0.34873	**3.232**	0.28018	0.2758	**4.979**	0.25118	0.24704	**1.244**

It can be noticed from Table 4.6 and graphical views of the curves that, the end leakage correction method given in section 2.4.5 considerably improves the prediction accuracy of the flux linkage predictions, especially for the rotor positions near OUT position.

4.3.3 Comparison of Torque – Speed Characteristics

Torque – Speed characteristics for different advance angles are calculated by the software using the predicted curves either with and without end leakage correction.

4.3.3.1 Predicted Torque – Speed Curves Without End Leakage Correction

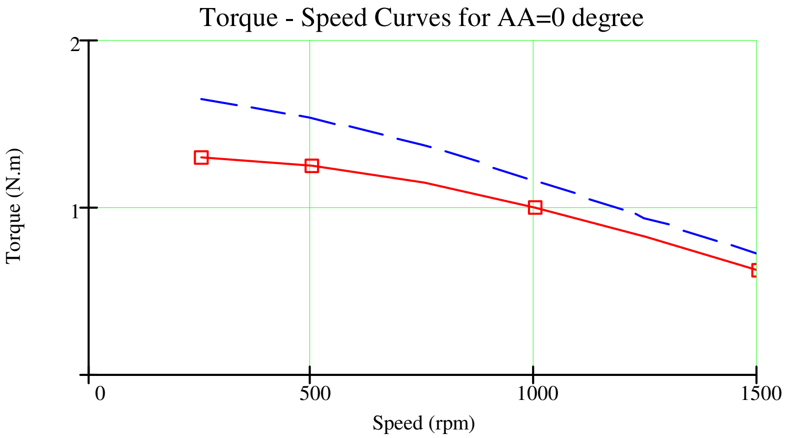

- - - - Predicted - - - - Measured

Figure 4-15: Torque – Speed curves, AA = 0^0

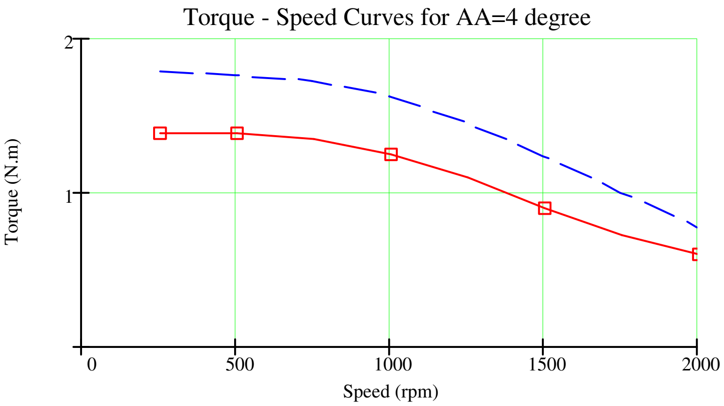

- - - - Predicted - - - - Measured

Figure 4-16: Torque – Speed curves, AA = 4^0

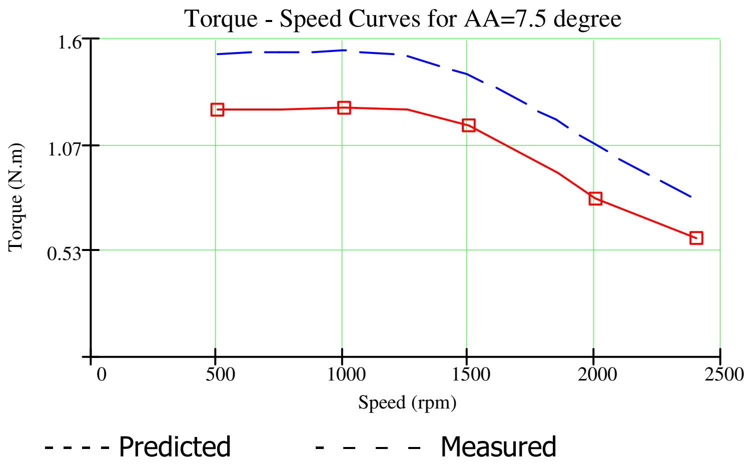

Figure 4-17: Torque – Speed curves, AA = 7.5^0

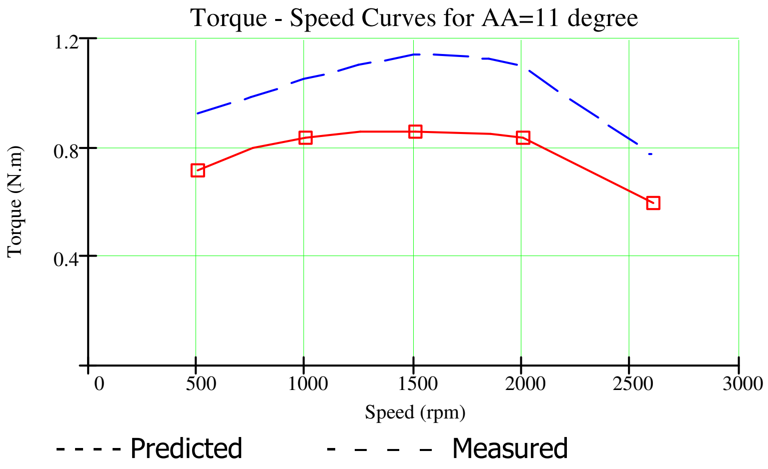

Figure 4-18: Torque – Speed curves, AA = 11^0

Table 4-8: The percentage errors between predicted and measured torques

AA = 0^0				AA = 4^0			
rpm	**Measured**	**Predicted**	**%err**	**rpm**	**Measured**	**Predicted**	**%err**
250	1.300	1.646	-26.62%	**250**	1.380	1.786	-29.42%
500	1.250	1.527	-22.16%	**500**	1.380	1.760	-27.54%
1000	1.000	1.160	-16.00%	**1000**	1.250	1.622	-29.76%
1500	0.625	0.713	-14.08%	**1500**	0.900	1.226	-36.22%
1600	0.540	0.648	-20.00%	**2000**	0.600	0.772	-28.67%
AA = 7.5^0				AA = 11^0			
rpm	**Measured**	**Predicted**	**%err**	**rpm**	**Measured**	**Predicted**	**%err**
500	1.250	1.522	-21.76%	**500**	0.720	0.930	-29.17%
1000	1.255	1.543	-22.95%	**1000**	0.840	1.050	-25.00%
1500	1.170	1.424	-21.71%	**1500**	0.860	1.143	-32.91%
2000	0.800	1.070	-33.75%	**2000**	0.840	1.097	-30.60%
2400	0.600	0.785	-30.83%	**2600**	0.600	0.770	-28,33%

From Table 4.7 and Figures 4.14 to 4.17, it is observed that, without the end leakage correction, significant errors as much as 36% occur between predicted and measured torque – speeds curves. In the next section, same curves will be obtained using predicted flux linkage curves including the end leakage correction.

4.3.3.2 Predicted Torque – Speed Curves With End Leakage Correction

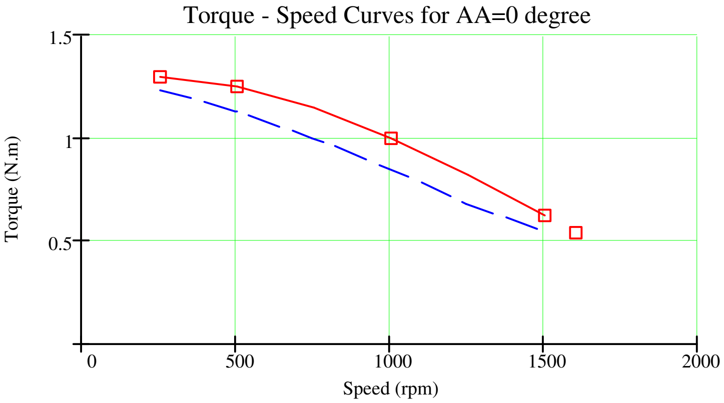

- - - - Predicted – – – – Measured

Figure 4-19: Torque – Speed curves, AA = 0^0

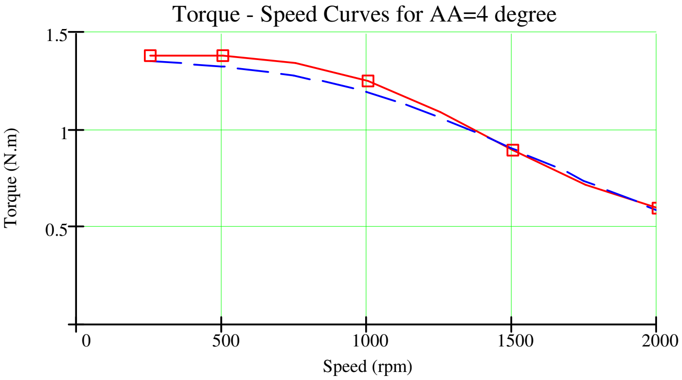

- - - - Predicted – – – – Measured

Figure 4-20: Torque – Speed curves, AA = 4^0

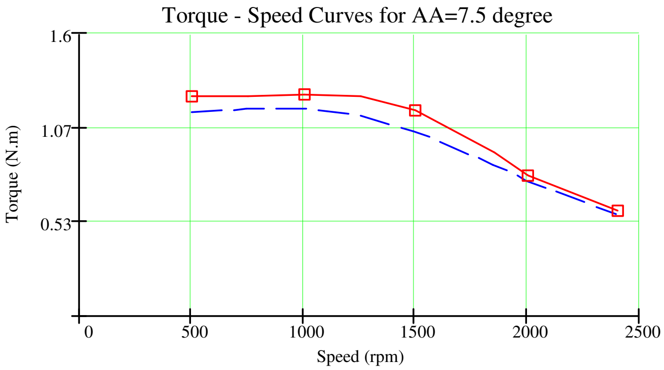

- - - - Predicted - – – – Measured

Figure 4-21: Torque – Speed curves, AA = 7.5^0

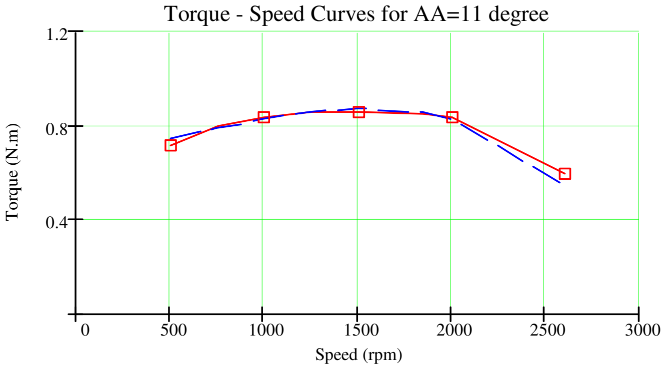

- - - - Predicted - – – – Measured

Figure 4-22: Torque – Speed curves, AA = 11^0

Table 4-9: The percentage errors between predicted and measured torques

AA = 0^0				AA = 4^0			
rpm	**Measured**	**Predicted**	**%err**	**rpm**	**Measured**	**Predicted**	**%err**
250	1.300	1.230	5.38%	**250**	1.380	1.358	1.59%
500	1.250	1.132	9.44%	**500**	1.380	1.324	4.06%
1000	1.000	0.846	15.40%	**1000**	1.250	1.197	4.24%
1500	0.625	0.537	14.08%	**1500**	0.900	0.905	-0.56%
1600	0.540	0.491	9.07%	**2000**	0.600	0.583	2.83%
AA = 7.5^0				AA = 11^0			
rpm	**Measured**	**Predicted**	**%err**	**rpm**	**Measured**	**Predicted**	**%err**
500	1.250	1.157	7.44%	**500**	0.720	0.745	-3.47%
1000	1.255	1.171	6.69%	**1000**	0.840	0.832	0.95%
1500	1.170	1.050	10.26%	**1500**	0.860	0.876	-1.86%
2000	0.800	0.766	4.25%	**2000**	0.840	0.828	1.43%
2400	0.600	0.576	4.00%	**2600**	0.600	0.546	9.00%

The torque – Speed curves obtained using the predicted flux linkage curves with end leakage correction are similar to measured curves in shape and close in torque values with a maximum error of 15%. The curves are above measured curves for uncorrected flux linkage curves. After the correction, torque – speed curves shift down below the measured curves. From this point of view, correction algorithm reduces the amount of average torque, and causes the predicted and measured curves to be closer. However, from Figure 4.18, it is observed that, there seems to be an over correction, but since the errors are in tolerable limits, this prediction method can be used in the optimization part of the software. Until here, the verifications of the methods given in Chapter 2 are investigated. Next section covers the results of optimizations stated in Chapter 3.

4.4 Optimization Results

The mathematical background and formulation of optimization algorithm are given in Chapter 3. Also, the constraints and adaptation of SRM weight minimization problem into the optimization scheme are given in Chapter 3. In this section, the results for weight minimization problems for wash speed (SRWash) and spin speed

(SRSpin) will be given. Both designs will be investigated if they could satisfy the performance needs of other design. Both minimization problems are started from two initial conditions for each. Results are given in following sections.

4.4.1 Optimization results for SRWash

520 rpm with 1.7 N.m torque requirement, Efficiency $\geq$80%, and $J_C \leq 6.5$ A/mm^2
$\varepsilon 1=0.0001$, $\varepsilon 2=0.1$, $\varepsilon 3=0.1$, $k_w=0.7$

Table 4-10: Optimization results for SRWash

	Initial D. #1	**Final D. #1**	**Initial D. #2**	**Final D. #2**
Rotor inner diameter (du,X1)	20	20	18	20
Rotor outer diameter (di,X2)	36	34.075	20	36.51
Stator outer diameter (Do,X3)	110.4	118.43	90	123
Core length (Lc,X4)	30	24.26	15	20.08
Back core width (yb,X5)	8	6	4	5.16
Stator pole width (ts,X6)	8.4	7.4	5	7.966
Rotor tooth width (tr,X7)	8.4	7.41	5	7.97
Airgap length (g,X8)	0.25	0.25	0.25	0.25
Advance Angle	10^0	7.62^0	10	10.434
Motor Weight (gr)	**2088**	**2024**	**712**	**1942**
Torque (N.m)	**2.298**	**1.7**	**0.166**	**1.7**
Efficiency (%)	**74.79**	**80.304**	**44**	**82.104**
J_{RMS} (A/mm^2)	**8.96**	**6.4**	**8.783**	**6.406**
Stator pole average flux density (Bt_{AV})	1.033	1.131	1.247	1.04
Number of Iterations taken for convergence		270		252

The final designs show a difference of 4% in weight. This result shows that, similar to all electrical machine minimization problems [21], local minima present. To reach the minimum of local minima, the convergence rates might be reduced. However, due to the non-linear nature of SRM, and complexity of the calculation methods, smaller convergence rates cause the process to fail with lack of accuracy error.

After examining the final results, it is observed that they satisfy the constraints which are stated in Chapter 3 in detail.

<u>For initial design #1</u>, briefly:

- T_{AV} = 1.7 N.m, satisfied,
- Efficiency = 80.3, satisfied,
- Air gap length = 0.25 mm satisfied,
- Inner diameter of the rotor = 20 mm, satisfied
- Rotor tooth depth = 7.037 mm, which is approximately 28 times air gap length, satisfied,
- Stator pole depth = 35.9275, which is approximately 143 times air gap length, satisfied,
- Current density = 6.4 A/mm^2, satisfied,
- Stator and rotor tooth width, in normalized form (t/λ):
  - t_{sn} = 0.414, satisfied,
  - t_{rn} = 0.414, satisfied,
- $\frac{\lambda_r}{g}$ = 71.366, satisfied.

<u>For initial design #2</u>, briefly:

- T_{AV} = 1.7 N.m, satisfied,
- Efficiency = 82.104, satisfied,
- Air gap length = 0.25 mm satisfied,
- Inner diameter of the rotor = 20 mm, satisfied
- Rotor tooth depth = 8.255 mm, which is approximately 33 times air gap length, satisfied,
- Stator pole depth = 37.82, which is approximately 148 times air gap length, satisfied,
- Current density = 6.406 A/mm^2, satisfied,

- Stator and rotor tooth width, in normalized form (t/λ):
  - $t_{sn} = 0.416$, satisfied,
  - $t_{rn} = 0.416$, satisfied,
- $\frac{\lambda_r}{g} = 76.466$, satisfied.

4.4.2 Performance of SRWash at 12000 rpm

The aim of this section is to investigate the performance of SRWash at high speed operation.

Final Design #1: $T_{AV} = 0$,

Final Design #2:

$T_{AV} = 0.002192$ N.m for AA = 7.5^0,

$T_{AV} = 0.00578$ N.m for AA = 13.51^0,

$T_{AV} = 0.0045$ N.m for AA = 15^0,

$T_{AV} \approx 0$ N.m for AA > 15^0,

These results show that, final designs obtained for SRWash can not produce necessary torque of 0.35 N.m.

4.4.3 Optimization results for SRSpin

12000 rpm with 0.35 N.m torque requirement, Efficiency $\geq$35%, and $J_C \leq 6.5$ A/mm^2
$\varepsilon1=0.0001$, $\varepsilon2=0.1$, $\varepsilon3=0.1$, $k_w=0.7$

Table 4-11: Optimization results for SRSpin

	Initial D. #1	**Final D. #1**	**Initial D. #2**	**Final D. #2**
Rotor inner diameter (du,X1)	20	20.122	18	20
Rotor outer diameter (di,X2)	46	45.09	30	44.52
Stator outer diameter (Do,X3)	120	101.359	90	100
Core length (Lc,X4)	40	29.354	20	27.63
Back core width (yb,X5)	8	7.88	4	7.86
Stator pole width (ts,X6)	7.8	9.449	6.3	9.311
Rotor tooth width (tr,X7)	7.85	9.451	6.32	9.322
Airgap length (g,X8)	0.25	0.25	0.25	0.25
Advance Angle	18	19.163	18	17.77
Motor Weight (gr)	**3286**	**1754**	**979**	**1620**
Torque (N.m)	**0.3**	**0.35**	**0.239**	**0.35**
Efficiency (%)	**25.71**	**39.09**	**74.33**	**40.7**
J_{RMS} (A/mm^2)	**1.769**	**4.72**	**6.42**	**4.69**
Stator pole average flux density (Bt_{AV})	0.2	0.212	0.51	0.225
Number of Iterations taken for convergence		231		224

The final designs of SRSpin also show a difference of 7.63% in weight. The presence of local optima is observed. After examining the final results, it is observed that they satisfy the constraints which are stated in Chapter 3 in detail.

For initial design #1, briefly:

- T_{AV} = 0.35 N.m, satisfied,
- Efficiency = 39.09, satisfied,
- Air gap length = 0.25 mm satisfied,
- Inner diameter of the rotor = 20 mm, satisfied
- Rotor tooth depth = 12.48 mm, which is approximately 50 times air gap length, satisfied,
- Stator pole depth = 20, which is 80 times air gap length, satisfied,
- Current density = 4.72 A/mm^2, satisfied,
- Stator and rotor tooth width, in normalized form (t/λ):
  - t_{sn} = 0.4, satisfied,
  - t_{rn} = 0.4, satisfied,
- $\frac{\lambda_r}{g}$ = 94.439, satisfied.

For initial design #2, briefly:

- T_{AV} = 0.35 N.m, satisfied,
- Efficiency = 40.7, satisfied,
- Air gap length = 0.25 mm satisfied,
- Inner diameter of the rotor = 20 mm, satisfied
- Rotor tooth depth = 12.25 mm, which is approximately 50 times air gap length, satisfied,
- Stator pole depth = 19.64, which is approximately 78 times air gap length, satisfied,
- Current density = 4.69 A/mm^2, satisfied,
- Stator and rotor tooth width, in normalized form (t/λ):
  - t_{sn} = 0.4, satisfied,
  - t_{rn} = 0.4, satisfied,
- $\frac{\lambda_r}{g}$ = 93.242, satisfied.

4.4.4 Performance of SRSpin at 520 rpm

The aim of this section is to investigate the performance of SRWash at high speed operation.

Final Design #1:

T_{AV} = 1.724 N.m, for AA = 7.5^0, and current limit of 4.6A,

Efficiency = 69.4%

Current density = 6.97 A/mm^2,

The coil fill factor is set as 0.7 in this study, however, for the test motor SR2, k_w=0.827. Considering this difference, we can calculate current densities for k_w of SR2.

Current density = $6.97 \cdot \frac{0.7}{0.827}$ =5.89 A/mm^2,

Final Design #2:

T_{AV} = 1.72 N.m, for AA = 7.5^0, and current limit of 5A,

Efficiency = 68.4%

Current density = 7.72 A/mm^2, which exceeds the limit of 6.5 A/mm^2, using the k_w of SR2:

Current density = $7.72 \cdot \frac{0.7}{0.827}$ =6.534 A/mm^2, which is very close to the constraint of 6.5 A/mm^2.

These results show that, the final design #1 is suitable for use in 520 rpm. However, the final designs of SRWash could not produce required torque. It can be said that, for a washing machine application, the design of the motor should be made for high speed operation considering the low speed requirements.

4.5 Conclusion

In this chapter, the verifications of the performance calculation methods stated in Chapter 2 are given. Comparisons are made with measurements. It is seen that, once the flux linkage characteristics as a function of excitation level and rotor position are known, the performance of the motor can be predicted in an accurate way. For a motor at design stage, those characteristics can not be measured. This is valid also for each step of optimization process given in Chapter 3. With the given motor geometry and magnetic properties, those characteristics can be predicted as explained in section 2.4. Using the related methods, flux linkage characteristics of a real motor are predicted, and compared with measurements. It is seen that, with the end leakage correction operation, predicted curves are very close to measured curves.

Since, flux linkage prediction and analysis methods given in Chapter 2 are accurate enough, they can be used in the optimization process. In this chapter, the results optimization schemes carried on for the SRMs given in Chapter 3 are given. Final designs show that, there exist local minima. To reach the minimum of local minima, the convergence criteria should be decreased, but this operation causes the process finish before satisfying the constraints, because of the complexity of the problem.

In the last part of the chapter, the final designs of SRWash are analyzed for the speed requirement of SRSpin, and likewise, final designs of SRSpin are analyzed for the speed requirement of SRWash. It is seen that, a motor optimally designed for low speed can not satisfy high speed requirements. On the other hand, it is found that, the designs for high speed also satisfy the low speed operation requirements.

If a motor is desired to operate both at low and high speed, a double speed optimization process would be useful, which primarily optimizes the motor for high speed, considering the requirements of low speed operation.

CHAPTER 5

CONCLUSION

5.1 General

For industrial applications, the Switched Reluctance Motor and drives are serious contenders of induction and DC motors, because of the simple motor structure, having no rotor windings, and concentrated coils in stator poles. Simple and reliable drive circuitry is also an advantage for SRM. However, need for position sensing, extremely high ripple on torque especially at low speeds decreases the populary of SRM. Considerable number of researchs are directed on development of drive circuitry and control algorithms which interests in reduction of torque ripple and acoustic noise.

This study contains a brief introduction to SRM. Its structure and principle of operation are given in a short view. In this study, SRM performance analysis and design optimization procedures have been developed, considering that the motor is driven by a asymmetric bridge converter.

For the performance analysis of SRM, methods are investigated and implemented in a user friendly software. Once the flux linkage characteristics as a function of rotor position and excitation level of an SRM are known, the performance calculations can be achieved at a given speed or speed range. Performance calculations include, calculation of steady – state average torque, torque ripple, copper and core losses and efficiency. Implementation of performance calculation methods are tested for a 750 Watt, 4 phase SRM. Comparisons between measurements and predicted results, given in Chapter 4, show that the implementation of proposed analysis methods is accurate.

An important subject in using the performance calculation methods is the requirement of flux linkage characteristics. The user can enter pre-obtained characteristics or can select the flux linkage prediction option of the software. The prediction method is based on a set of numerically obtained data. This method requires the motor geometry and B-H characteristics of lamination to be entered. Once these data are known, prediction of flux linkage characteristics is an easy and fast operation as described in section 2.4. The results of predictions show that, due to the leakage flux of end windings, a correction is needed. As stated in section 2.4.5, a correction method is developed and implemented. The accuracy of flux linkage prediction method is also tested with measurements and results are given in Chapter 4. It is observed that, the prediction method with end leakage flux correction is accurate enough to be used, especially in an optimization process.

The construction of optimum motor geometry, which satisfies required performance specifications is a very important subject. In this study, the optimization of SRM is formulated as a weight minimization problem. The performance requirements, geometrical aspects, and manufacturing difficulties impose some constraints to the problem. In this study, performance constraints are imposed on steady – state average torque, efficiency and rms value of current density.

Since the problem is a constrained optimization problem, Augmented Lagrangian method is preferred, which converts the constrained optimization problem into unconstrained form. The minima are searched using the DFP (Davidson, Fletcher, Powell) method, which requires only the gradient of the function. Chapter 3 covers the theoretical background of optimization scheme is given.

Weight minimization process is carried on considering the needs of a washing machine application. This application requires the SRM to operate at two speeds, one for washing operation, and the other is for spinning operation. At each speed requirement, starting from two initial designs, optimizations are carried on. For low speed optimization, the SRM is named as SRWash, and for high speed optimization, the SRM is named as SRSpin. Final designs of SRWash and SRSpin are investigated if they could satisfy the requirements of other motor. Results show that only the final designs of SRSpin can achieve low speed operation with some slight modifications. From this result, it can be concluded that, for this kind of application, the optimization algorithm should be developed for high speed operation considering the requirements of low speed operation.

5.2 Future Work

Computer technology is growing faster, enabling very complex computations, like field solution routines, to be done in a fast way. For the analysis part of the software, a field solution routine might be integrated into the software to predict flux linkage characteristics of given motor geometry. However, for an optimization process, using field solutions in every iteration is not feasible yet.

REFERENCES

[1] Stephenson, J. M., Corda, J., "Computation of Torque and Current in Doubly-Salient Reluctance Motors From Nonlinear Magnetization Data", Proc. IEE, Vol 126, No 5, May 1979, pp.393-396

[2] Ertan, H.B., "Analytical Prediction of Torque and Inductance Characteristics of Identically Slotted Doubly Salient Reluctance Motors", Proc. IEE, Vol 4, 1986, pp.230-236

[3] Ertan, H.B., "Prediction of Torque and Permeance Characteristics of Asymmetrical Tooth Pairs", Proc. Of the International Conference on Electrical Machines (ICEM), Munich, 1986, Vol 1, pp.97-100

[4] Ertan, H.B., "Prediction of Torque and Inductance Displacement Characteristics of Asymmetrically Slotted VR Motors Using a Simplified Model for Numerical Solution", IEEE Trans. On Magnetics, Vol 35, No 5, September 1999, pp.4247-4258

[5] Krishnan, R., "Switched Reluctance Motor Drives: Modeling, Simulation, Analysis, Design, and Applications", CRC Press, 2001

[6] Singh, G., "Mathematical Modelling of Step-Motor", Proceedings of the incremental motion control system and devices', University of Illinois, USA, pp.59-148

[7] Pickup, I.E.D., Tipping, D., "Method for Predicting the Dynamic Response of a Variable Reluctance Stepping Motor", Proc. IEE, 1973, Vol 120, No 7, pp.757-765

[8] Pickup, I.E.D., Tipping, D., "Prediction of Pull-in Rate and Settling-time characteristics of a Variable Reluctance Stepping Motor and Effect of Stator-Damping Coils on These Characteristics", ibid., 1976, Vol 123, No 3, pp.213-219

[9] Byrne, J.V., O'Dwyer, J.B., "Saturable Variable Reluctance Machine Simulation Using Exponential Function", Proceedings of the international conference on stepping motors and systems, University of Leeds, July 1976, pp.11-1

[10] Blenkinshop, P.T., "A Novel, Self-Commutating, Singly-Excited Motor", Ph.D Thesis, University of Leeds, Oct. 1976

[11] Lawrenson, P., "Switched- Reluctance Motor Drives", IEE Electronics and Power, February 1983, pp.144-147

[12] Lawrenson, P., Stephenson, J.M., Blenkinshop, P.T., Corda, J., "Variable – Speed Switched Reluctance Motors", proc. IEE, Electrical Power Applications, 1980, Vol 127, no 4, pp.253-265

[13] Ertan, H.B., "Prediction of Static Torque of Step Motors", Ph.D. Thesis, University of Leeds, 1977

[14] Ertan, H.B., "Asimetrik Çıkık Kutuplu Magnetik Yapılarda Kuvvetin Hesabı", Doçentlik Tezi, 1982

[15] Mukherji, K.C., Neville, S., "Magnetic Permeance of Identical Doubly Slotting: Deductions from Analysis by F.W. Carter", Proc. IEE, 1971, Vol 118, no 9, pp.1257-1268

[16] Harris, M.R., Hughes, A., Lawrenson, P.J., "Static Torque Production in Saturated Doubly – Salient Machines", Proc. IEE, 1975, Vol 122, no 10, pp.1121-1127

[17] Harris, M.R., Andjagholi, V., Lawrenson, P.J., Hughes, A., Ertan, H.B., "Unifying Approach to the Static Torque of Stepping Motor Structures", Proc. IEE, 1977, Vol 124, no 12, pp.1215-1224

[18] Ertan, H.B., Hughes, A., Lawrenson, P.J. "Efficient Numerical Method for Predicting the Torque/Displacement Curve of Saturated VR Motors", Proc. IEE, Electrical Power Applications, 1980, Vol 127, no 4, pp.246-252

[19] Corda, J., Stephenson, J.M., "Analytical Estimation of the Minimum and Maximum Inductances of a Doubly Salient Motor", Proceedings of the International Conference on Stepping Motors and Systems, 1979, pp.50-59

[20] Pierre, A.D., Lowe, M.J., "Mathematical Programming via Augmented Lagrangians", Addison-Wesley Publishing Company, 1975

[21] Tohumcu, M., "Optimum Design of Switched Reluctance Motors", Ph.D. Thesis, Middle East Technical University, 1985

[22] Şahin, F., "Optimum Geometry for Torque Ripple Minimization of Switched Reluctance Motors", M.Sc. Thesis, Middle East Technical University, 1996

[23] Materu, P.N., Krishnan, R., "Estimation of Switched Reluctance Motor Losses", IEEE Transactions on Industry Applications Vol 28, no 3 May/June 1992, pp.668-679

[24] Daşdemir, B., "Non-linear Analysis and Design Optimization of Switched Reluctance Motors", unpublished document

[25] Yılmaz, A., "Hedef Çamaşır Makinası İstenen Tork Hız Karakteristikleri", Tübitak – Bilten, May 2004

[26] Kızılkaya, M.Ö., "A Software for Dynamic Simulation of Switched Reluctance Motor",M.Sc. Thesis, Middle East Technical University, December 2001,

[27] Jones, A. L., "Permeance Model and Reluctance Force Between Toothed Structures", Proc. Of 5th symposium on incremental motion control system and devices, University of Illinois, May 1976, paper H

[28] Chai, H.D., "Permeance Model and Reluctance Force Between Toothed Structures", Proc. Of 2nd symposium on incremental motion control system and devices, University of Illinois, May 1973, paper K

[29] Carter, F.W., "The Magnetic Field of the Dynamo-Electric Machine", Jour IEE, 1926, pp.1115-1138

[30] Byrne, J.V., "Tangential Forces in Overlapped Pole Geometries Incorporating Ideally Saturable Material", IEEE Trans. Vol. MAG-8, No 1, March 1972, pp.2-9

[31] Unnewehr, L.E., Koch, W.H., "An Axial Air-Gap Reluctance Motor for Variable Speed Applications", IEEE Trans. Vol. PAS-93, 1074, pp.367-376

[32] Blenkinsop, P.T., "A Novel Self Commutating Singly Excited Motor", Ph.D. Thesis, University of Leeds, 1976

[33] Koch, W.H., "Thyristor Controlled Pulsating Field Reluctance Motor System", Electric Machines and Electromagnetics, 1977, pp.201-215

[34] Walivadekar, V.N., Athani, V.V., Acharya, G.N., "Equivalent Circuit for Switched reluctance Motor", IEEE TENCON'93, Beijing

[35] Xu, L., Ruckstadter, E., "Direct Modeling of Switched Reluctance Machine by Coupled Field – Circuit Method", IEEE Trans. On Energy Conversion, Vol. 10, No 3, September 1995,

[36] Tang, Y., Kline, J.A., "Modeling and Design Optimization of Switched Reluctance Machine by Boundary Element Analysis and Simulation", IEEE Trans. On Energy Conversion, Vol. 11, No 4, December 1996,

[37] Ohdachi, Y., "Optimum Design of Switched reluctance Motors using Dynamic Finite Element Analysis", IEEE Trans. On Magnetics, Vol. 33, No 2, March 1997,

[38] Miller, T.J.E., "Optimal Design of Switched Reluctance Motors", IEEE Trans. On Industrial Electronics, Vol. 49, No 1, February 2002

[39] ANSYS Commands Manual, Swanson analysis Systems, Revision 5.0, Houston, 1992

[40] ANSYS User Manual, Swanson analysis Systems, Revision 5.0, Houston, 1992

[41] ANSYS Theoretical Manual, Swanson analysis Systems, Revision 5.0, Houston, 1992

[42] Beşenek, N., "Numerically Calculated Force and Permeance Data for Doubly Salient Geometries", Ms. Thesis, METU, 1988

[43] Yağan, Ö., "A new Approach to the Design optimization of Switched Reluctance motor", M.S. thesis, METU, 1990

[44] Kızılkaya, M.Ö., "The Method for Calculation of the Frictional Torque of a Motor and Application of the Method to the SR Motor", January 2001

[45] Ertan, H.B., Daşdemir, B., "An Approach to Analysis and Design of Switched Reluctance Motors", ISEF 2001, Poland,

[46] Cantu, M., "Delphi 3", Sybex,1998,

[47] Mathews, J.H., "Numerical Methods", Prentice Hall International, UK, 1987

APPENDIX A

THE SOFTWARE

A.1. Introduction

A software is developed for the study, named as SRCAD. The aim of SRCAD is to carry on all the methods given in Chapter 2 and Chapter 3. It is developed in Borland Delphi environment using the object pascal language [46]. The Delphi environment helps the programmer to develop user friendly interfaces in a fast way by suplying all necessary design tools such as forms, buttons, graphic plotters, etc. Pascal programming language is one of the most powerful and easy compiler, with its modular structure, existing in the market.

The software has two main parts, and each part can be called from the main interface. First part is the analysing part, and second one is the optimization part. Although each part has their own interface, they use most of the procedures in a common way. In the following sections, these parts will be explained briefly.

A.2. Analysis Part of SRCAD

As its name implies, this part of the software is to achieve performance calculations for given SRM. User has two options in using this part. He/She can either enter already obtained flux linkage data, or can prefer to input physical and magnetic properties of an SRM,then the software can predict necessary flux linkage data. Other inputs necessary for an analysis are the operating conditions:

Operation speed, or speed range,

- Switch On, and Switch Off instants (alternatively, Advance angle, and Excitation Period),
- Loss curves as a function of flux density and frequency, user can select curves from available library or can enter already obtained data,
- Supply voltage,
- Current limit and chopper settings (Imax, Imin),
- Phase resistance.

Main flowchart of the analysis part of the SRCAD is given below in Figure A.1.

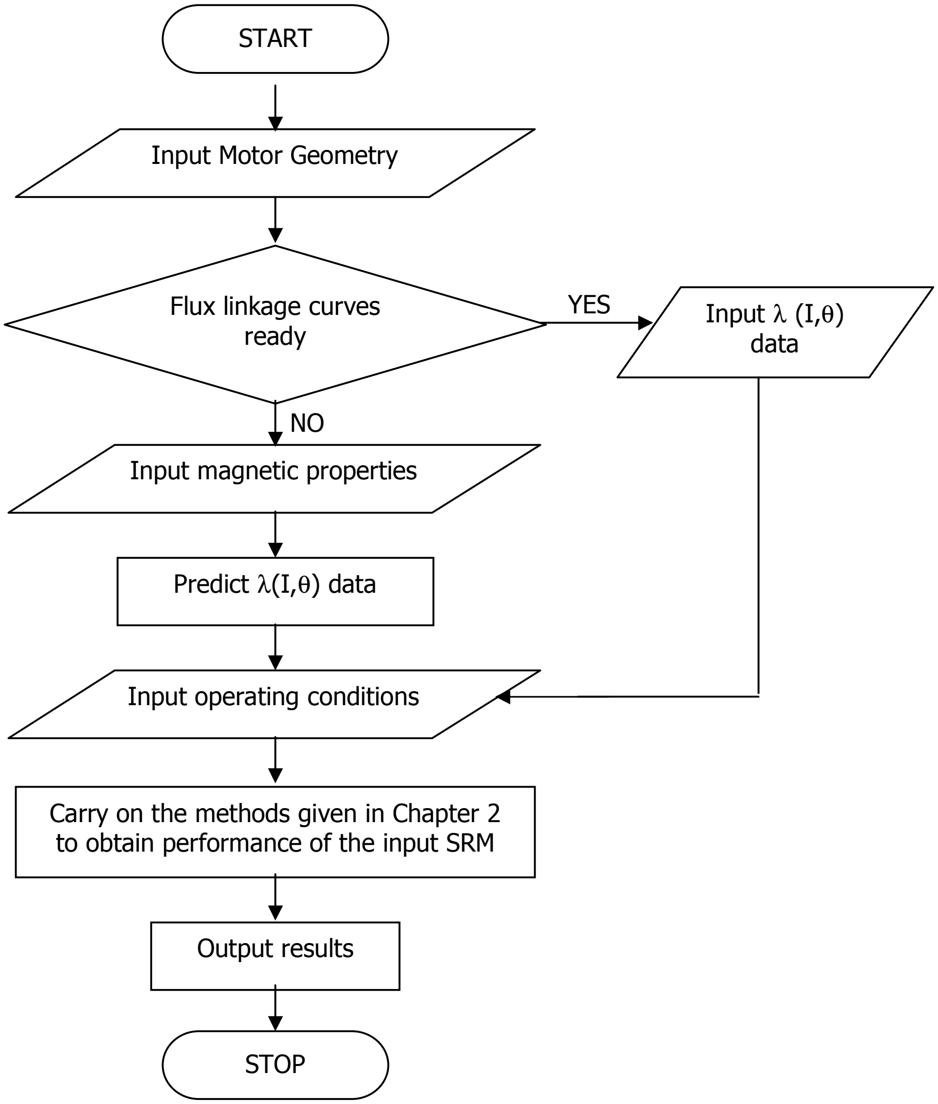

Figure A–1: Main flowchart of the analysis part of SRCAD

A.2.1. Graphical User Interface

Main interface of analysis part of SRCAD is shown in Figure A.2 below.

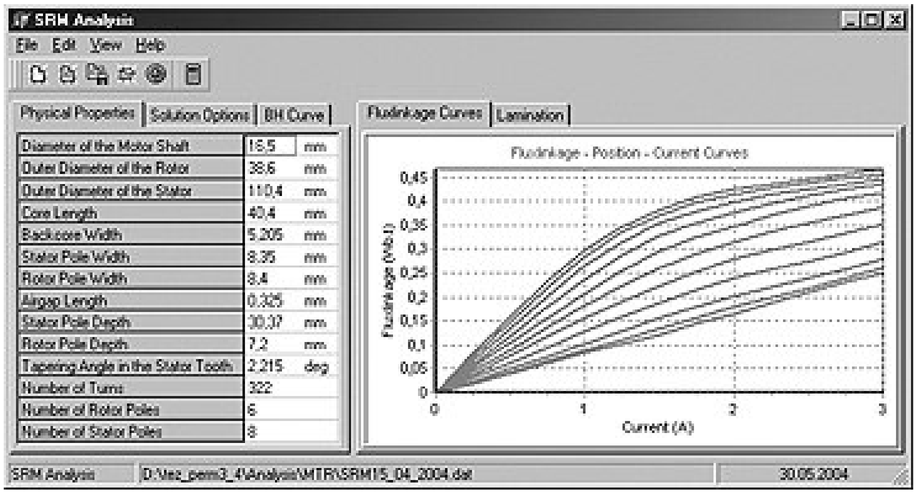

Diameter of the Motor Shaft	16,5	mm
Outer Diameter of the Rotor	38,6	mm
Outer Diameter of the Stator	110,4	mm
Core Length	40,4	mm
Backcore Width	5,205	mm
Stator Pole Width	8,35	mm
Rotor Pole Width	8,4	mm
Airgap Length	0,325	mm
Stator Pole Depth	30,37	mm
Rotor Pole Depth	7,2	mm
Tapering Angle in the Stator Tooth	2,215	deg
Number of Turns	322	
Number of Rotor Poles	6	
Number of Stator Poles	8	

Figure A–2: Main interface of analysis part of SRCAD

This interface includes;

- Physical properties of input SRM geometry,
- Solution options, which are operating conditions, shown in Figure A.3,
- BH Characteristic of selected material,
- Input or predicted flux linkage curves,
- Lamination drawing of input SRM geometry, shown in Figure A.4.
- Results on a separate window, as shown in Figure A.5, and Figure A.6.

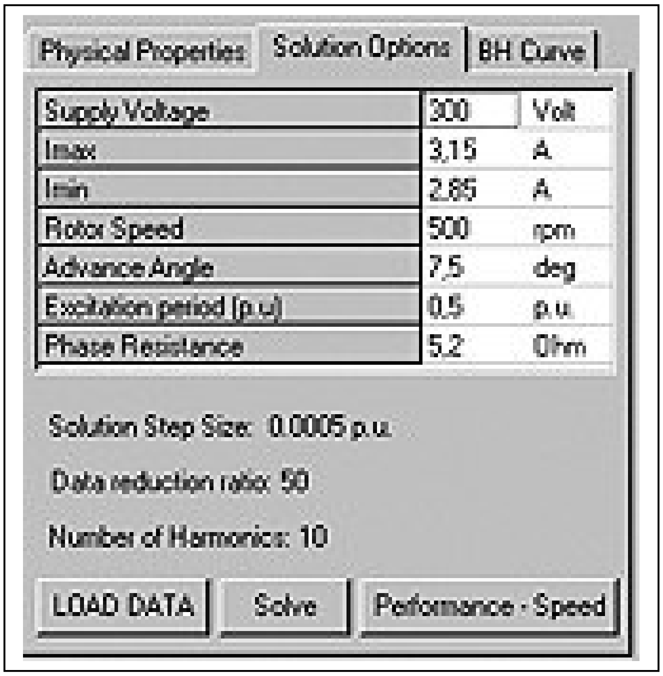

Supply Voltage	300	Volt
Imax	3,15	A
Imin	2,85	A
Rotor Speed	500	rpm
Advance Angle	7,5	deg
Excitation period (p.u)	0,5	p.u.
Phase Resistance	5,2	Ohm

Solution Step Size: 0.0005 p.u.

Data reduction ratio: 50

Number of Harmonics: 10

Figure A–3: Operation conditions

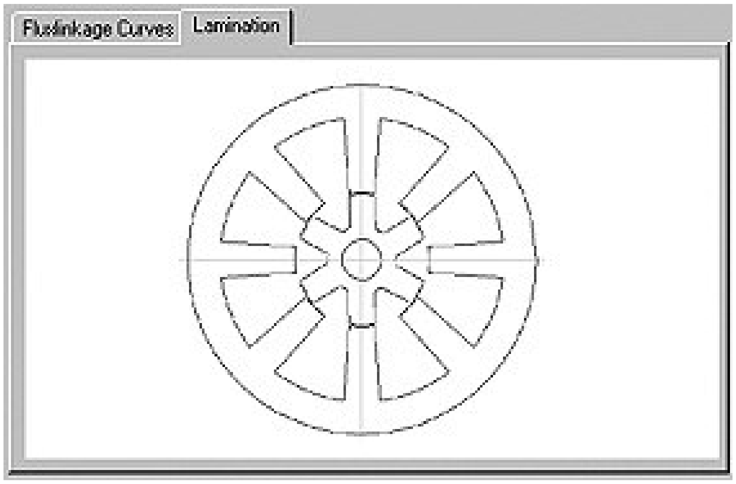

Figure A–4: Lamination drawing capability of SRCAD

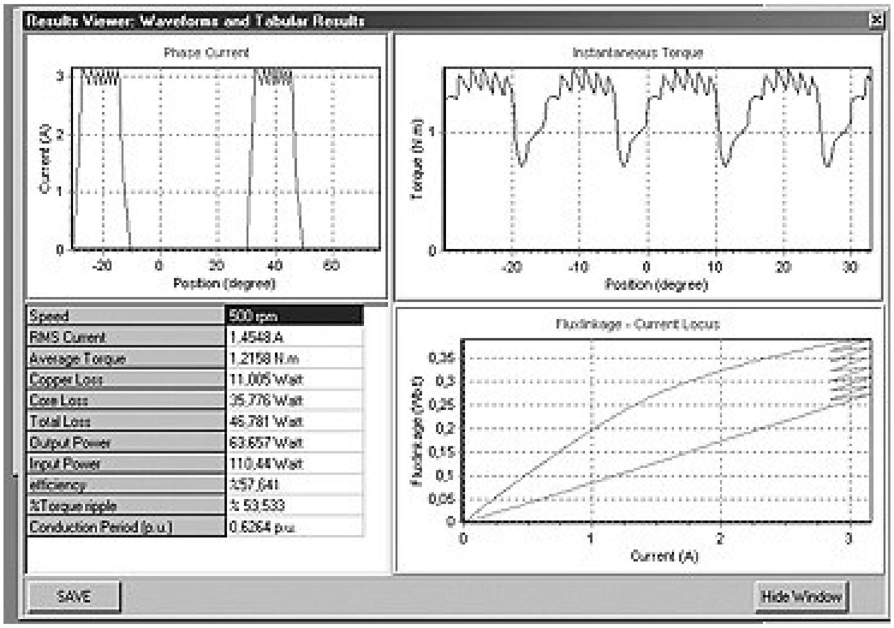

Speed	500 rpm
RMS Current	1,4548 A
Average Torque	1,2158 N.m
Copper Loss	11,005 Watt
Core Loss	35,776 Watt
Total Loss	46,781 Watt
Output Power	63,657 Watt
Input Power	110,44 Watt
efficiency	%57,641
%Torque ripple	% 53,533
Conduction Period (p.u.)	0,6264 p.u.

Figure A–5: Results window of SRCAD, for single speed option

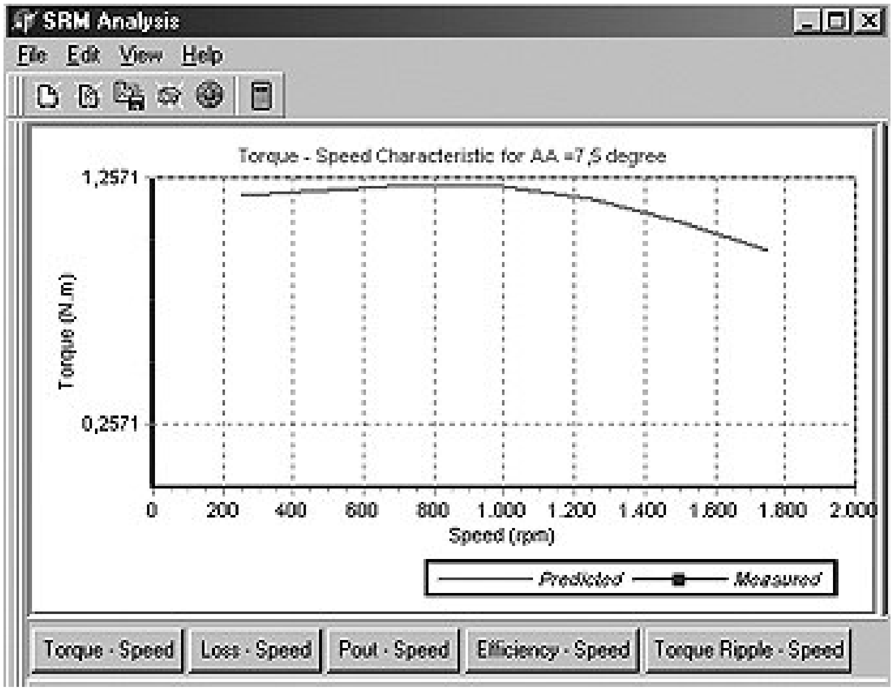

Figure A–6: Results window of SRCAD, for multi – speed option

A.2.2. Modules of Analysis Part of SRCAD

The software is developed using the advantage of modularity of Pascal programming language. Several modules are prepared to achieve necessary computations.

A.2.1.1. Main Unit

This unit includes the interface descriptions, and calls required procedures from other modules. For example, for single speed analysis, the calling procedure is given in Figure A.7.

```
procedure TForm1.Button2Click(Sender: TObject);
var
i,j,K:integer;
sum,son,fark:double;
kat1:double;
begin
clearcharts;
Xon := (-22.5 - SRM1.OpCond.AA)/(180/SRM1.dim_vector[NRT]);
.
.
.
```

Figure A–7: Calling procedure for single speed analysis

A.2.1.2. The "SRMUnit" Module

This unit includes the mathematical procedures listed below

- Integration,
- Fourier series expansion,
- Reduction of data,
- Periodic waveform constructor,

A.2.1.3. The “Fluxlinkage” Module

This unit includes the procedures necessary for flux linkage predictions. These are listed below:

- “Toothregion”, which achieves the operations stated in section 2.4,
- “Backiron”, which achieves the operations stated in section 2.4.3,
- “Endleakage”, which achieves the operations stated in section 2.4.5,

A.2.1.4. The “RK” module

This unit includes the procedures necessary for performance calculations of the SRM. These are listed below:

- “RKOnestep”, which achieves the Runge Kutta 4th order algorithm,
- “SolveSystem”, which achieves the operations stated in section 2.2.2,
- “Solvesystem2”, which achieves the modified operation of procedure “Solvesystem”, to be used in optimization algorithm, as stated in section 3.8.1.

A.2.1.5. The “OP” Module

This unit achieves operating point calculations which described in section 2.4.4. the procedures of this module are listed below:

- “operatingpoint”, which achieves the operations stated in section 2.4.4,
- “Bisection”, called from “operatingpoint” procedure to find the current operating point using the bisection method [47]

A.2.1.6. The “Interpol” Module

This module is for interpolation tasks. Procedures of this module are listed below:

- “Linear”, achieves linear interpolation [47],
- “Cubic”, achieves cubic spline interpolation [47],
- “PWL”, achieves quadratic interpolation [47].

A.2.1.7. The “Loss” Module

This module includes the procedures necessary for loss calculations. The procedures of this unit are listed below:

- “copperloss”, calculates the copper loss using the methods given in section 2.3.1,
- “ironloss”, calculates the core loss using the methods given in section 2.3.2.

A.3. Optimization Part of SRCAD

This part of the software is developed for design optimization of SR motor. User, inputs the initial design and variables needed for constraint to the software from the interface, and then software carries on the optimization process.

A.3.1. Graphical User Interface

Main interface of optimization part of SRCAD is shown in Figure 5.8 below.

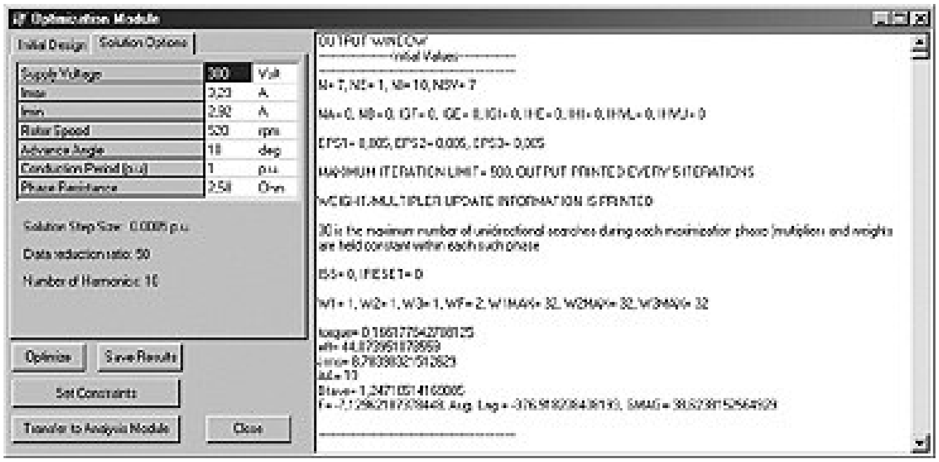

Supply Voltage	300	Volt
Imax	3.20	A
Imin	2.90	A
Rotor Speed	520	rpm
Advance Angle	18	deg
Conduction Period (p.u)	1	p.u
Phase Resistance	2.58	Ohm

Solution Step Size: 0.0005 p.u.
Data reduction ratio: 50
Number of Harmonics: 16

```
OUTPUT WINDOW
-------------Initial Values-------------
----------------------------------------
N= 7, NS= 1, NI= 10, NSV= 7

EPS1= 0,005, EPS2= 0,005, EPS3= 0,005

MAXIMUM ITERATION LIMIT = 500, OUTPUT PRINTED EVERY 5 ITERATIONS

WEIGHT-MULTIPLIER UPDATE INFORMATION IS PRINTED

30 is the maximum number of unidirectional searches during each minimization phase (multipliers and weights
are held constant within each such phase

ISS= 0, IRESET= 0

W1= 1, W2= 1, W3= 1, WF= 2, W1MAX= 32, W2MAX= 32, W3MAX= 32
```

Figure A–8: Main interface of optimization part of SRCAD

A.3.2. Modules of Optimization Part of SRCAD

The optimization part of SRCAD uses the same procedures as analysis part, for performance calculations and prediction of flux linkage curves. Two modules exist in this part.

A.3.2.1. The "MainUnitOpt" module

This unit includes the interface descriptions of optimization part of SRCAD, and calls optimization procedures from the interface.

A.3.2.2. The "Optim" Module

All the mathematical background given in chapter 3 is included in this module. The procedures of this module are listed below:

- "FXNS", calculates cost function, equality and inequality constraint functions for the current search vector, $\overline{X}$,
- "GRAD", calculates the gradients of cost function, equality and inequality constraint functions for the current search vector, $\overline{X}$,
- "INITIAL", initializes the algorithm, sets boundary values for bounded variables, flags and counters. All multipliervectors and gradients are set to zero,
- "LPNLP", runs the optimization algorithm, calls other procedures,
- "SEARCH", achieves a quadratic-convergent unidirectional search,
- "UPDATE", updates equality and inequality constraint multipliers, and penalty weights,
- "DFPRV", generates the search direction R,
- "VALUE", evaluates the problem functions, called from "SEARCH" procedure,
- "DELTA", calculates the $\left\|\overline{X}^{k+1} - \overline{X}^{k}\right\|$, $\left\|\nabla L_a^{k+1} - \nabla L_a^{k}\right\|$, and $\left\|\nabla L_a^{k}\right\|$
- "AUGLAG", formulates Augmented Lagrangian,
- "OUTPUT", outputs the results with predetermined intervals

APPENDIX B

IMPLEMENTATION OF SOME MATHEMATICAL ROUTINES

B.1. Integration of Data Arrays

The software developed for the study frequently requires the integration operation over data arrays. Since the data to be integrated are defined as point by point, the most suitable method is the Trapezoidal Rule [47]. Figure B.1 explains the rule graphically. The area under the curve obtained by the data points in each subinterval is considered as a trapezoid, and the integral of whole array is the sum of these trapezoids. This operation is achieved by the software as shown in Figure B.2.

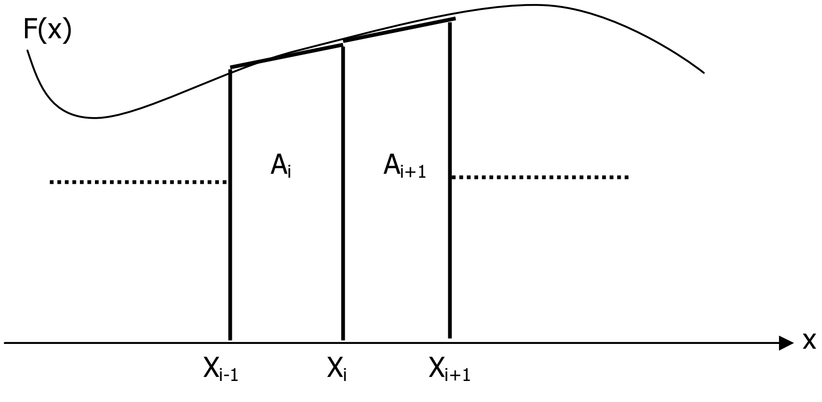

Figure B–1

$$A_i = \frac{F(X_i) + F(X_{i+1})}{2} \cdot \left(X_{i+1} - X_i\right) \qquad \textbf{(B. 1)}$$

$$\int F(X) = \sum_i A_i \qquad \textbf{(B. 2)}$$

```
sum:=0;
for i := 0 to intN-1 do
sum:=sum+ 0.5*(Yarray[i+1]+Yarray[i])*(Xarray[i+1]-Xarray[i]);
result := sum;
```

Figure B–2: Sample code from the software, which achieves integration over data arrays

B.2. Fourier Series

From the definition of Fourier series:

$$f(x) = \frac{A_0}{2} + \sum_{n=1}^{N} \left[A_n \cos(nx) + B_n \sin(nx)\right] \qquad \textbf{(B.3)}$$

Where,

$$A_0 = \frac{2}{T} \int_{-T/2}^{T/2} f(x)dx \qquad \textbf{(B.4)}$$

$$A_n = \frac{2}{T} \int_{-T/2}^{T/2} f(x)\cos\left(\frac{n\pi x}{T/2}\right)dx \qquad \textbf{(B.5)}$$

$$B_n = \frac{2}{T} \int_{-T/2}^{T/2} f(x)\sin\left(\frac{n\pi x}{T/2}\right)dx \qquad \textbf{(B.6)}$$

And T is the period of periodic function. Software achieves these formulations as shown in Figure B.3.

```
result.A0:=(2/(*T))*integrate(intN,Xarray,Yarray);
 for i := 1 to N do
 begin
  for j := 0 to intN do
  ytemp[j] := Yarray[j]*cos((i*pi*Xarray[j]*2/T));
 result.An[i]:= (2/T)*integrate(intN,Xarray,Ytemp);
 end;

 for i := 1 to N do
 begin
  for j := 0 to intN do
  ytemp[j] := Yarray[j]*sin(i*pi*Xarray[j]*2/T);
 result.Bn[i]:= (2/T)*integrate(intN,Xarray,Ytemp);
 end;
```

Figure B–3: Implementation of Fourier series by the software

B.3. Numerical Differentiation

To take numerical differentiation of function *f(x)*, it should be evaluated at values that lie to the left and right of x . Then the numerical differentiation of *f(x)* is, by definition[47]:

$$f^{'}(x) = \frac{f(x+h) - f(x-h)}{2h} \qquad \textbf{(B.7)}$$

During the optimization process, the value of h is determined as:

$h = X[i]/100$ i = 1..9

And x[i] is the ith independent optimization parameter.

APPENDIX C

ANSYS MACRO FILES

The field solution software, ANSYS, has been frequently used in the study, especially for constructing a normalized data which are used for end leakage correction on predicted flux linkage curves. 2D and 3D field solution macro files are prepared. These macro files are given below combined in one macro file.

The macro given below, first constructs the 2D model of given motor geometry. Later, the 3D model is constructed, and solved for specified excitation level and rotor position.

C.1. Ansys macro file which constructs and solves 2D and 3D models

```
/cle
pi=4*atan(1)
lg=40
tl=0.3
/prep7
K,20,0,0,0,
mur_rtr=500
rsv_rtr=1.8e-7
k_rtr=50
dens_rtr=7800
c_rtr=475
mur_str=500
rsv_str=0
```

```
k_str=50
rsv_cl=1.7e-8
lambda=lg*airgap
trns=350*lambda/70
Rrotorout=lambda*6/(2*pi)
*SET,Rrotorin,Rrotorout-Hrt_slot
*SET,Rshaft,4e-3
*SET,Rstatorin,Rrotorout+airgap+Hst_slot
*SET,Hyoke,10e-3
*SET,Rstatorout,Rstatorin+Hyoke
*SET,Wst_slot,tl*lambda
*SET,Wrt_slot,tl*lambda
et,1,53
mp,murx,1,1
R,1,1
et,2,53
mp,murx,2,mur_rtr
*if,rsv_rtr,gt,0,then
 mp,rsvx,2,rsv_rtr
*endif
R,2,1
et,3,53
mp,murx,3,mur_str
*if,rsv_str,gt,0,then
 mp,rsvx,3,rsv_str
*endif
R,3,1
et,4,53
mp,murx,4,1
mp,rsvx,4,rsv_cl
r,4,1
et,5,53
mp,murx,5,1
mp,rsvx,5,rsv_cl
```

```
r,5,1
et,6,53
mp,murx,6,1
mp,rsvx,6,rsv_cl
r,6,1
et,7,53
mp,murx,7,1
mp,rsvx,7,rsv_cl
r,7,1
K,1,-1*(Wst_slot/2),Rrotorout+airgap-0.4*Rrotorout,0,
K,2,1*(Wst_slot/2),Rrotorout+airgap-0.4*Rrotorout,0,
K,3,1*(Wst_slot/2),Rrotorout+airgap+Hst_slot+0.7*Hst_slot,0,
K,4,-1*(Wst_slot/2),Rrotorout+airgap+Hst_slot+0.7*Hst_slot,0,
L,1,2
L,2,3
L,3,4
L,4,1
local,11,0,0,0,0
circle,20,Rrotorout+airgap
lovlap,all
ldele,1
ldele,9
ldele,10
ldele,13
ldele,16
ldele,7
ldele,8
lcomb,14,15,0
KDELE,1
KDELE,2
KDELE,5
KDELE,7
KDELE,8
ldele,3
```

```
ldele,12
ldele,11

local,11,1,-1*(Wst_slot/2),Rrotorout+airgap-0.4*Rrotorout,0
wpcsys,,11
KGEN,2,4, , , ,2.2, , ,0
local,11,1,1*(Wst_slot/2),Rrotorout+airgap-0.4*Rrotorout,0
wpcsys,,11
KGEN,2,3, , , ,-2.2, , ,0
kdele,3
kdele,4

local,11,0,0,0,0
L,10,2
L,2,1
L,1,9

circle,20,Rrotorout+airgap+Hst_slot
lovlap,all

ldele,8
ldele,9
ldele,2
ldele,13
ldele,6
ldele,7
ldele,10
lcomb,11,12,0
KDELE,1
KDELE,2
KDELE,3
KDELE,5
KDELE,6
local,11,0,0,0,0,0,0,0
```

```
wpcsys,,0

al,all
aatt,3,3,3

local,11,1,0,0,0
local,11,0,0,0,0,90,0,0

local,11,1,0,0,0
local,11,0,0,0,0,90,0,0

K,1,-1*(Wrt_slot/2),Rrotorin-0.5*Rrotorin,0,
K,2,1*(Wrt_slot/2),Rrotorin-0.5*Rrotorin,0,
K,3,1*(Wrt_slot/2),Rrotorout+0.5*Rrotorout,0,
K,4,-1*(Wrt_slot/2),Rrotorout+0.5*Rrotorout,0,

LSTR,1,2
LSTR,2,3
LSTR,3,4
LSTR,4,1

circle,20,Rrotorout
lovlap,all
ldele,3
ldele,12
ldele,13
ldele,5
ldele,8
ldele,17
ldele,20

circle,20,Rrotorin
lovlap,all
ldele,1
```

```
ldele,6
ldele,7
ldele,2
ldele,5
ldele,13
ldele,21
lcomb,18,19,0
lcomb,17,20,0

local,11,0,0,0,0,90,0,0
asel,none
al,8,12,17,18
aatt,2,2,2

KDELE,6
KDELE,16
KDELE,18
KDELE,12
KDELE,15
KDELE,5
KDELE,1
KDELE,2
KDELE,3
KDELE,4

local,11,0,0,0,0,0,0,0
local,11,1,0,0,0,0,0,0
asel,none
asel,s,mat,,2
AGEN, ,all, , , ,-90, , , ,1
allsel

asel,none
asel,s,mat,,3
```

```
!Generate stator poles
AGEN,2,1, , , ,45, , ,0
AGEN,2,1, , , ,45*2, , ,0
AGEN,2,1, , , ,45*3, , ,0
AGEN,2,1, , , ,45*4, , ,0
AGEN,2,1, , , ,45*5, , ,0
AGEN,2,1, , , ,45*6, , ,0
AGEN,2,1, , , ,45*7, , ,0
allsel

asel,none
asel,s,mat,,2
!Generate rotor teeth
local,11,1,0,0,0,0,0,0
AGEN,2,2, , , ,60*1, , ,0
AGEN,2,2, , , ,60*2, , ,0
AGEN,2,2, , , ,60*3, , ,0
AGEN,2,2, , , ,60*4, , ,0
AGEN,2,2, , , ,60*5, , ,0

local,11,0,0,0,0,0,0,0
wpcsys,,0
PCIRC,Rrotorin,Rshaft,0,360
aatt,2,2,2
aadd,all
aatt,2,2,2
cm,rtr,area
!asum
!*GET,rotor_area,AREA,all,AREA

asel,none
PCIRC,Rstatorout,Rstatorin,0,360
aatt,3,3,3
asel,none
```

```
asel,s,mat,,3
aadd,all
aatt,3,3,3

cm,sttr,area
asel,none
PCIRC,Rshaft,0,0,360
aatt,1,1,1

allsel
local,11,0,0,0,0,0,0,0
wpcsys,,0
numcmp,area
numcmp,line

allsel
csys,0
numcmp,kp
K,116,-Rstatorout,-80e-3/2,0
K,117,-Rstatorout,80e-3/2,0
L,116,117

K,118,Rstatorout,-80e-3/2,0
K,119,Rstatorout,80e-3/2,0
L,118,119

K,120,-65e-3/2,Rstatorout2,0
K,121,65e-3/2,Rstatorout2,0
L,120,121

K,122,-65e-3/2,-Rstatorout2,0
K,123,65e-3/2,-Rstatorout2,0
L,122,123
L,117,120
```

```
L,119,121
L,116,122
L,118,123
lovlap,all

AL,73,75,76,80,82,17,34
AL,74,77,78,79,81,38,42
numcmp,area

AADD,2,4,5
!saved here
ang=30
/prep7
numcmp,area
numcmp,line
!Rotate the rotor
asel,s,area,,1
asel,a,area,,2
csys,1
AGEN, ,all, , , ,ang, , , ,1
allsel
csys,0

/prep7
asel,s,area,,3
cm,sttr,area

cmsel,s,sttr
allsel,below,area
PCIRC,Rstatorout,(Rrotorout+(airgap/2)),0,360
aovlap,all
aadd,5,6,8

numcmp,area
```

```
numcmp,line
cm,sttr,area

allsel
cmsel,u,sttr
PCIRC,(Rrotorout+(airgap/2)),0,0,360
aovlap,all
cm,rotor,area
allsel
numcmp,area
numcmp,line
allsel
PCIRC,(Rstatorout),0,0,360
aovlap,all

aadd,7,8,10
adele,1
numcmp,area
numcmp,line

aglue,all
ET,9,200,7

allsel
aatt,,,9
type,9

/prep7
Allsel
!Generate mesh structure
SMRT,3
MSHAPE,1,2D
MSHKEY,0
AMESH,all
```

```
AREFINE,all, , ,2,0,1,1
allsel

csys,0
ET,8,SOLID96
esize,,20
!Generate 3D model
asel,s,area,,3
!allsel,below,area
type,8
mat,2
VEXT,all, , ,0,0,0.04,,,,

asel,s,area,,1
!allsel,below,area
type,8
mat,3
VEXT,all, , ,0,0,0.04,,,,

asel,s,area,,2
asel,a,area,,4
!allsel,below,area
type,8
mat,1
VEXT,all, , ,0,0,0.04,,,,

allsel

esize,,10
asel,s,area,,2
!allsel,below,area
type,8
mat,1
VEXT,all, , ,0,0,-0.02,,,,
```

```
asel,s,area,,1
!allsel,below,area
type,8
mat,1
VEXT,all, , ,0,0,-0.02,,,,

asel,s,area,,3
asel,a,area,,4
!allsel,below,area
type,8
mat,1
VEXT,all, , ,0,0,-0.02,,,,

allsel
esize,,10
allsel
asel,s,loc,z,0.04
type,8
mat,1
VEXT,all, , ,0,0,0.02,,,,

allsel
aclear,all
nsel,all
nummrg,all
!asel,s,loc,z,0

allsel
numcmp,volu
numcmp,area
numcmp,line

allsel
```

```
!Construct current sources
local,20,0,0,Rrotorout+airgap+Hst_slot/2,20e-3,0,90,0

csys,20
wpcsys,20

race,0.7*2*8.2e-3,.028,,trns*4,10e-3,0.7*hst_slot,,,'coil1'

local,21,0,0,-1*(Rrotorout+airgap+Hst_slot/2),20e-3,0,90,0

csys,21

wpcsys,21

race,0.7*2*8.2e-3,.028,,trns*4,10e-3,0.7*hst_slot,,,'coil2'

csys,0
wpcsys,0

!csys,1
!nsel,s,loc,x,Rstatorout

Allsel
!Set actual material properties
!MAT,2,
!/INPUT,emagRM23_Lin.SI_MPL

!MAT,3,
!/INPUT,emagRM23_Lin.SI_MPL


Allsel
/SOLU
NSLE,S
```

```
*GET,NMIN,NODE,,NUM,MIN
D,NMIN,MAG,0
NSEL,ALL
EQSLV,FRONT, ,0,
NEQIT,50
Allsel
MAGSOLV,3,,,,,1
*dim,cur,array,1
cur(1)=4
!Calculate flux linkage
lmatrix,1,'coil','cur','lg_%lg%_tl_%tl%_ang_%ang%'
FINISH
```